PLASMA CHARACTERISTICS WITH RESPECT TO HIGHLY PRESSURIZED DRILLING APPLICATIONS

A Thesis

by

JACOB ROBERT MALLAMS

Submitted to the Office of Graduate and Professional Studies of
Texas A&M University
in partial fulfillment of the requirements for the degree of

MASTER OF SCIENCE

Chair of Committee,	David Staack
Committee Members,	Dion Antao
	Chad Mashuga
Head of Department,	Andreas A. Polycarpou

December 2020

Major Subject: Mechanical Engineering

ABSTRACT

Deep earth drilling is a key technique to extract oil, gas, and geothermal heat from the earth. Energy focusing methods have been explored as an alternative approach to reach these resources. Many of these techniques require incredibly high energies and complex systems. Here the fundamental elements of a hybrid drilling/energy focusing technique is discussed. By utilizing short time span plasma discharges, energy focusing can be achieved within traditional drilling systems. These discharges induce a strong cavitation and resulting shockwave. It is believed that this focused energy will lower the required cutting force to progress through the rock. Lowering the required cutting force will allow for lower drill bit wear, quicker rate of penetration, and an overall cost savings of the project. This paper will discuss the characteristics, capabilities, and requirements associated with a plasma discharge at downhole pressures.

The plasma behavior of discharges at pressures similar to downhole conditions have been explored. It has been proven that a high voltage (20+ kV) discharge is capable of discharging in pressures up to 350 atm. The consistency of this discharge is dependent on the electrode gap and supplied voltage. Higher pressures require higher voltages or smaller electrode gaps to remain consistent. Furthermore, the resulting impact of the discharge is a function of total system energy and the voltage/pressure ratio. Plasma energy has been quantified and recommendations for to maximize discharge energy is discussed. To obtain a better understanding of the discharge event, discharges have been imaged and characterized with both a high speed camera and an ICCD.

ACKNOWLEDGMENTS

I would like to thank Professor David Staack for his guidance, advice, and incredible knowledge throughout my time at Texas A&M. I have enjoyed every moment in the lab thanks to my great colleagues and their wiliness to help in every situation. Their excitement learn with me along the way has made every challenge enjoyable. Special thanks to Xin Tang and Mirza Akhter for reviewing this material and helping me at many points along the way. Thank you to the Texas A&M University Office of Graduate and Professional Studies for this very helpful LaTeX thesis template. Lastly, thank you to the rest of Texas A&M and everyone I met along the way, my time here has given me more than I had ever hoped for.

CONTRIBUTORS AND FUNDING SOURCES

Contributors

This work was supported by a thesis committee consisting of Professor David Staack and Professor Dion Antao of the Department of Mechanical Engineering and Professor Chad Mashuga of the Department of Chemical Engineering. I appreciate your time and effort in assisting me to successfully complete this program.

Several individuals were involved in creating the research within this paper. Xin Tang and Mirza Akhter's efforts have been foremost within many aspects of this process. Xin helped with many discussions, research, and project path decisions. He assisted in many of the experimental setups and experiments that led to the content within this thesis. Mirza's help was invaluable when it came to performing the long hours of experimentation needed for the results in this thesis. He has also helped to push many parallel objectives that support the tasks discussed within this thesis and the project goals as a whole. The SPARC engineering team has met weekly to discuss this work and all other aspects of the SPARC project. This team consists of Professor David Staack, Professor Dion Antao, Professor Bruce Tai, Mirza Akhter, Xin Tang, Sanat Kumar, and Aamer Kazi. I would also like to acknowledge the rest of my lab mates in the Staack Plamsa lab for their continued support and assistance. Matthew Burnette and Christopher Campbell in particular have helped with trouble shooting and safety inspections at many points. With the exception of the helping hands discussed above, all other work conducted for this thesis was completed independently.

Funding Sources

This project has been supported by a grant from The Department of Energy's Office of Energy Efficiency & Renewable Energy. The grant has been awarded for "efficient drilling for geothermal energy" and was awarded through the Geothermal Technologies Office. This grant supported my assistantship with the university as well as the capital expenses and involved research costs of the project as a whole.

NOMENCLATURE

A	Area
C	Capacitance
CAD	Computer-aided design
d	Electrode gap distance
DC	Direct current
DOE	Department of Energy
e	Electron charge
EDGE	Efficient drilling for geothermal energy
EERE	Energy Efficiency & Renewable Energy
EMI	Electromagnetic interference
FOD	Foreign object debris
GTO	Geothermal Technologies Office
I	Current
ICCD	Intensified Charged Coupled Device
j	Current density
n_e	Electron density
NPT	American National Standard Pipe Thread
p	Ambient Pressure
P	Power
PDC	Polycrystalline diamond compact
PPE	Personal protective equipment
RC	Resistor Capacitor

ROI	Region of interest
ROP	Rate of penetration
SPARC	Shockwave and Plasma Accelerated Rock Cracking
U	Energy
V	Voltage
v_d	Electron drift
V_b	Breakdown Voltage
V1	Voltage present immediately after air switch breakdown
V2	Voltage present immediately before primary fluid breakdown

TABLE OF CONTENTS

Page

LIST OF FIGURES

FIGURE Page

LIST OF TABLES

TABLE Page

1. INTRODUCTION

1.1 Introduction

Plasma is often termed the fourth state of matter beyond solids, liquids, and gasses. Simply put, plasma is described as ionized gas that is capable of conducting electricity. In nature it can be found in the form of lightning, auroras, or static electric sparks. Outside of nature, engineers utilize plasma for items such as fluorescent lighting, arc welders, semiconductor fabrication, and more. In this paper a novel use of plasma is discussed.

Plasmas offer unique opportunities for applications throughout many different industries [1]. The medical industry has found uses to improve sterilization, tissue removal and repair, in-vivo operations, dental tools, and much more. [2, 3, 4, 5]. There have been many interesting benefits offered by plasma in the agriculture and food sanitation fields [6, 7, 8]. Environmental pollution control through plasma processes has emerged as a feasible approach of managing water and air contaminants [9, 10, 11, 12, 13, 14, 15]. The oil industry has come to utilized on the impacts that plasma has to offer. Plasma techniques have been developed in both oil processing [16, 17] and oil extraction [18, 19, 20].

This paper focuses on the potential applications for plasma use within drilling and rock cracking [21]. By introducing nanosecond pulsed plasma discharges, high energy shock waves and cavitations can be created [22, 23]. This process is capable of introducing cracks upon a substrate. Preliminary experiments in this project have verified the ability to successfully produce fractures within hard rocks with this technique. It is believed that this approach could be utilized within modern oil, gas, and geothermal drilling to improve upon the rate of penetration (ROP), drill bit wear, and reliability during the drilling process. Most tradition drilling applications rely on drilling fluid for efficient operations [24]. In order to adapt the nanosecond pulse discharge technology to drilling, it will be critical for the plasma to create similar or improved effects within the drilling fluid at the high pressures and temperatures present downhole.

It isn't hard to see that plasma approaches are becoming more common, understood, and welcomed across all industries. Many of the before mentioned technologies utilize the rapid energy impulse that pulsed plasma has to offer. Downhole plasma induced rock cracking shares the same root physical approach as these technologies. These successful projects show promise that the necessary technology for a downhole plasma technology is readily available. Furthermore, the oil industry itself is no stranger to using plasma as a means of progressing through the earth.

1.2 Motivation

The oil and geothermal industry relies upon the cost effective creation of the well. If drilling expenses rise too high the entire project may suffer or fail. A primary cost of the drilling process is the rig rental and staff cost [25]. As a result, it is critical to minimize the time a drill rig is on site. Rate of penetration and down time are the basic two factors that determine the length of time the rig and crew must to utilized. When considered literally, the faster a drilling project can penetrate and the longer the bit life (to reduce down time) the cheaper the well will be. Hard rock - Granite and feldspar are known for increasing the difficulty and time of drilling. Due to the associated difficulties of these hard rocks, plasma induced cracks would be improving both the ROP and the drill bit wear, resulting in reduced downtime and more profitable drilling projects.

The motivation for this project originated within the Texas A&M Staack Plasma lab during experiments on mechanical plasma creation via snapping shrimp [26]. These shrimp use their strong claws to create a cavitation and resulting plasma. This cavitation is utilized to stun prey or crack rocks during burrowing. The latter of these strategies encouraged the idea of plasma within drilling. The Department of Energy's (DOE) Office of Energy Efficiency & Renewable Energy (EERE) contains the Geothermal Technologies Office (GTO) which funds a grant called The efficient drilling for geothermal energy (EDGE). A portion of this grant was awarded to the Shockwave and Plasma Accelerated Rock Cracking (SPARC) project within the Staack Plasma Lab. The project objective reads "We will leverage targeted microscale energy delivery at the rock surface during traditional drag bit type drilling operations to enhance rock reduction and increase the ROP to >30 ft/hr for geothermal lithology conditions of elevated temperature (200 °C),

extreme pressure (10 ksi) and rock compressive strength (200 MPa)." In order meet this objective the mechanics behind a plasma discharge at these conditions must be understood. A number of experiments to understand the plasma's behavior have been performed and are discussed at length within this thesis.

1.3 Thesis Statement

The initial step of designing a downhole plasma system will require the plasma characteristics to be well understood. Unfortunately, plasmas in liquids at these high pressures (3000+ psi) have been researched very little. Jones and Kunhardt ran a number of experiments discussing plasma breakdowns at these conditions [27], but since their investigation there have been few reports of high pressure experiments. In order to design plasmas for drilling application Jones's work needs to be expanded upon. A parametric, time resolved study of these conditions will help to offer understanding into the role that high pressures plays within the breakdown mechanics of plasma. This thesis will discuss the production, characteristics, and behavior of plasma within these drilling conditions.

There are a number of parameters that are important to understand in order to characterize and understand plasma within the drilling environment. Perhaps the most obvious characteristics to understand are the voltage and energy requirements for a downhole, pressurized plasma. Furthermore, a visual understanding of the mechanisms at play during a pressurized discharge will offer insight on how to maximize their effect within drilling. During the discharge a high pressure, high temperature cavitation bubble is formed. This bubble is expected to correlate to the energy released from the discharge [28]. In conjunction with the cavitation bubble, light emission from the plasma is capable of registering the magnitude of energy release as light emission is expected to increase with plasma density and therefore plasma intensity [29]. The plasma density light emission is considered a The latter of these two factors is utilized to gauging the relative force imposed upon the rock. In order to understand these parameters the following experiments have been performed.

Four key experiments have been conducted to evaluated the aforementioned characteristics. All experiments were conducted within a small pressure vessel capable of 400+ atm. Each experi-

ment was completed at several different pressure levels with appropriate diagnostics. The voltage requirements for breakdown has been explored at pressures up to 350 atm. Electrical data was collected in order to better understand the energy output and baseline requirements of the system at higher pressures. This experiment was then repeated with a smaller electrode gap and higher maximum voltages as this is considered to be a more efficient configuration for pressurized discharges. The third experiment conducted with the use of an Intensified Charged Coupled Device (ICCD) camera. The ICCD camera allowed for information within hundreds of nanoseconds of the event to be captured. The emitted light from the plasma discharge was measured using the ICCD in order to correlate the light emission with ambient pressures. The final experiment gathered high speed video data in order to generate a more clear picture of the events that occur during the discharge.

The hypothesis explored in this thesis is that a plasma discharge will remain feasible throughout the pressures explored indicating its potential for downhole application. This hypothesis is built on the understanding that the creation of plasma is dependent on the ambient density as opposed to the ambient pressure [30]. The density of gas will change dramatically as pressure is increased. The density of gas at 350 atm is roughly 360x more dense than at atmospheric conditions. Liquids, namely water, is incompressible and as such the density stays fairly constant through large pressure changes. The density of water will only increase approximately 1% at 350 atm. As such, it is expected that the plasma should remain feasible and generally the same within such conditions.

The conducted experiments have offered valuable information and key insights to hypothesis stated above. The remainder of this paper will discuss the supporting literature, experimental setup, experimental results, and conclusions of these tests. These findings will inform future work related to the construction and testing of more advanced plasma enhanced drilling experiments and ultimately the formulation of a commercial design.

2. LITERATURE REVIEW

2.1 Plasma Background

Plasmas are created when an electrical potential is strong enough to ionize a target gas. Upon ionization the gas becomes conductive and allows current to flow to a location of lower electrical potential. The behavior of the plasma is characterized by many aspects. Figure 2.1 describes the type of plasma you may achieve as the magnitude of the voltage and current are adjusted. At the beginning of the glow discharge there is a breakdown region where a plasma channel is formed and the gases become ionized. This region curve shows the critical behavior used for high intensity discharges. Upon reaching the breakdown voltage any stored energy will be released through the plasma channel until the energy is depleted or the plasma stabilizes through a driving current. It is this rapid discharge of energy that yields the mechanisms used to create rock cracking. The experiments studied within this paper utilize a double spark gap which consist of an air spark switch and a primary discharge. This allows the voltage to the primary discharge to be set to a value higher than the breakdown voltage of that electrode setup.

In order to maximize power output onto the substrate a capacitor is utilized to allow for increased stored energy. The equation of stored energy within a capacitor is show in equation 2.1. Where U is energy stored, C is capacitance, and V is voltage. Furthermore, the power output from a capacitor can be calculated using equation 2.2 where P is power, U is stored energy, and dt is the dissipation time. Through these equations it can be seen that a high potential(10kV+), nanosecond discharge is capable of generating a significant amount of power (during the short discharge duration). This level of power output yields a strong cavitation and shockwave in the wake of the discharge. Understanding the mechanisms driving this event will aid in optimizing the resultant effects.

$$U = \frac{1}{2}CV^2 \tag{2.1}$$

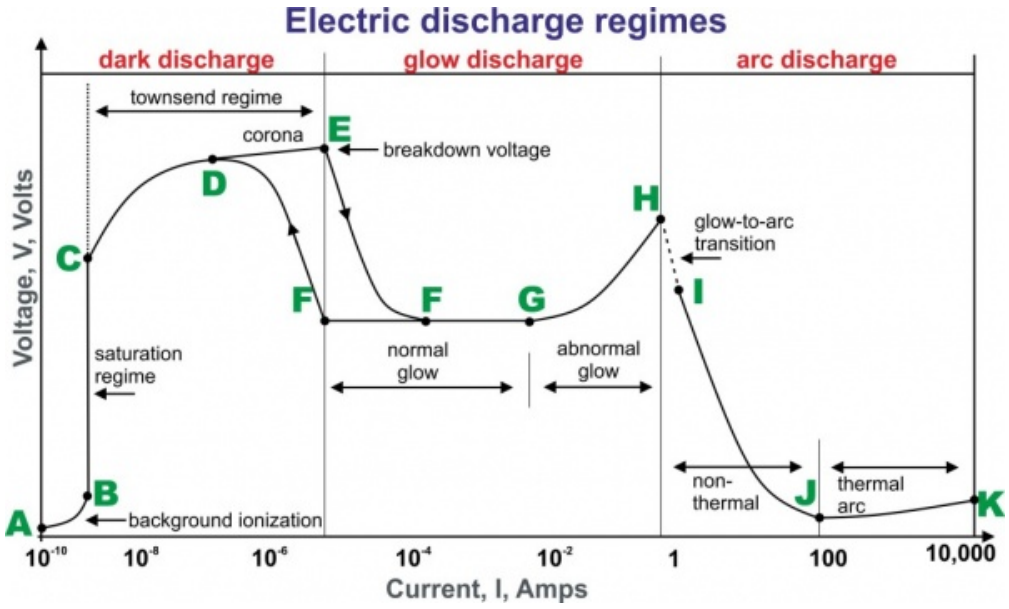

Figure 2.1: Plasma Discharge Diagram

$$P = \frac{dU}{dt} \tag{2.2}$$

2.2 Plasmas in Gases

Initial pulsed plasma research focuses primarily on gas-phase discharges. As a result the mechanisms involved in such an event are fairly well understood. A breakdown event is begun as a potential is created between the two electrodes - the cathode and anode. At some point an individual electron leaves the cathode and travels directly toward the anode. As the initial electron travels it gathers additional electrons and ions creating what is called an electron avalanche. Within the wake of this avalanche is the ionized, conductive gas column. [30]

In the event that there is stored energy within the system the newly formed column of ionized gas allows for the formation of an intense spark. The current density reaches a magnitude that creates intense joule heating, an increase in plasma temperature, and additional thermally ionized gas. Gas within the spark channel reach temperatures up to 20,000 K, and the electron concentration will near complete ionization. Conductivity is estimated to be roughly $\frac{102}{ohm*cm}$. At this point

ionization has reached a point that conductivity is determined through coulomb collisions instead of electron density. [31]

In conjunction with the temperature effects, the pressure and geometry within the column respond. The rapid temperature increase forces a significant increase in pressure. This pressure generates an intense cylindrical shock wave that emits outward from the column. The radius of the spark channel grows to approximately 1 cm allowing for an increase of current through the larger cross section. After the current peaks the effects began to diminish as energy is depleted. The current and voltage drops as driving forces diminish and the channel loses temperature while reducing in volume. The plasma will reach a point where it is no longer able to sustain ionization and the column will dissipate. [32]

2.3 Plasmas in Liquid

While the mechanisms for plasmas in gasses are generally accepted, the underlying process of liquid discharges are still argued. As technology has advanced, opportunities for more sophisticated experiments have been conducted. Despite this growth, no specific theory has become strong enough to rule out the others. Furthermore, it is possible that each contributes to the event in different capacities. The prevailing theories agree on the presence (or generation) of a localized low density region. Within this region an electron avalanche may form which evolves into a full discharge typically through the propagation of an incomplete plasma column termed a streamer [33].

A streamer is a branched structure that emits from the powered electrode once sufficient electrical potential has been met. Much like lightning within a thunderstorm, branched plasma channels will reach out until a lower potential is found or the energy needed to sustain the streamer has bled off. Within a storm the lower potential is the earth. Within lab experiments this lower potential is the complementing electrode. Significant research has been conducted on the shape, speed, and behavior of streamers. A recent study from Campbell [34] shows in great detail how these streamers will branch out from a single point on the electrode. The formation of these streamers will be affected the liquid medium, hydrostatic pressure, dissolved gasses, and electrode material [33].

Hydrostatic pressure is notable due to the relevance within the discussed experiments.

One possible source of the low density region may be the Lippmann effect. It is conceivably capable of creating a low-density cold microcavity or bubble in these conditions. [35] The Lippmann effect, simply put, is the change of surface tension as a result of electrical potential difference between two liquid conductors. Lewis explains that during a discharge event an impulse of strong potential is created. The fluid near an electrode will experience a reduction in the interfacial tension when exposed to this impulse. The magnitude of this effect argued to be sufficient enough to reduce the interfacial adhesion between the fluid and metal electrode to a point where the free surface tension becomes the presiding effect. At this point a reduction or full loss of adhesion onto the electrode occurs. This would offer a cavity for the full breakdown process to begin.

Seepersad expresses concerns upon timescales of hydrodynamic factors such as the Lippmann effect. [36] He remarks how electrostriction is capable of creating negative pressure nanoscale voids when exposed to the short nanosecond timescales at play. Electrostriction is the change in shape of an object due to applied electrical fields. Shneider supports these findings explaining that the the volumetric force acting on the dielectric fluid due to the electric field are capable of overcoming interfacial forces resulting in micro ruptures within the liquid. [23] Theses ruptures the offer negative pressures and subsequently an appropriate medium for breakdown to begin.

Some sources argue that bubble formation occurs through local heating, either through volume heating or field emission. [37] [38] This introduced heat vaporizes a small volume of liquid. Similar to other approaches, this localized heating offers a low pressure, low density vapor phase for breakdown to initiate. A key rebuttal to this theory arises in the case of submicrosecond discharges where the timescales involved for the discharge process to occur do not allow sufficient heat transfer. [39] Furthermore, work from Starikovskiy [40] claims that small enough timescales (picosecond) can create liquid plasma generation without the need bubble all together.

Several believe that preexisting nano-scale bubbles within the fluid offers a logical explanation on the presence of localized low density regions. Naidis has found that when artificially created microbubbles (40-100 μm) are introduced plasma discharges always began within the introduced

bubble. [41] Joshi addresses this idea directly and argues the above theories [39].

Joshi explains that in the case of nanosecond pulse discharges the timescale of the event is too short to allow for any temperature effects to occur. Similarly argued, hydrostatic effects will not have time to effect the state of the initiation medium. Electron-impact ionization and Zener tunneling, two ionization methods, were simulated and deemed insufficient to created low density regions. Joshi concludes that a random distribution of pre-existing nanobubbles is a sufficient explanation of the observed behaviors.

2.4 Plasmas in Pressurized Liquids

Upon the initiation of the plasma within the low density region a collection of streamers will form that branch toward the opposite electrode [42]. These streamers will continue to branch out until making contact with the other electrode. At this point the streamer offers a low resistance channel for the energy to flow through and the breakdown process occurs. This is consistent with streamer behavior within atmospheric conditions as well [43].

The understanding of the breakdown characteristics at ultra high pressures will be critical for use within downhole conditions. There have been very few studies regarding the characteristics of plasma at these conditions. However, Jones's work offers us some important knowledge regarding the situation. Jones did a number of experiments comparing electrode gap, pressure (1 atm-300 atm), and solution conductivity [44, 27]. While brief, Jones's work corresponds well with this thesis's initial tests. It will be critical to build upon his work to offer both accompanying visuals and the understanding that an immediate substrate may have on the breakdown process. Furthermore, verifying portions of Jones's work will allow us to build confidence in future downhole design requirements.

2.5 Energy Focusing Leverage

The effectiveness of the mechanisms studied in this paper rely heavily upon their ability to outperform traditional techniques. Nanosecond plasma discharges allow for a much faster energy release than any mechanical methods. Compressing a moderate amount of energy into a signifi-

cantly shorter timescale allows for a focused, powerful impulse that will have different destructive effects when compared to a slow, mechanical drill. Traditional oil rigs will have an equipped power on the order of 600 kW [45]. This power is used to operate all of the pumps, motors, and auxiliary equipment involved within the drilling process. The discharges discussed in this paper range from 40 to 160 Joules. If 1% of created rig power were dedicated to plasma processes, the discharges could be scaled up 3x and operate at 25 discharges/second.

Improving baseline power and efficiency is not the primary objective of integrating plasma. As mentioned above, the rapid energy release offers advantages inaccessible to traditional drilling. A complete plasma discharge with high enough energy will create a shock wave and cavitation bubble. Vogel [46] has explored these shock waves and cavitation bubbles from laser generated plasma. Within Vogel's paper he images the event from inception up until the event has been fully formed and the shock wave has traveled up to 300 μm. Depending on the event, this will occur anywhere between 80 ns to 140 ns. Vogel found the shock wave velocity to increase as the input energy increased; the maximum velocity to be obtained was 4450 m/s (three times the speed of sound in water) during an event caused by a 1 mJ, 6 ns laser pulse. Furthermore, Vogel calculated the velocity of the bubble wall to reach supersonic speeds as well, in some cases up to 2450 m/s. It is a reasonable assumption to consider that the destructive nature of these governed by the sharp increase in pressure associated with both the shockwave and the bubble. Several of the higher energy pulses within Vogel's experiment reach maximum shockwave pressures up to 7150 MPa or just over 1,000,000 psi. The corresponding peak bubble pressure has been calculated to be 8801 MPa, approximately 1,276,000 psi. These values would extraordinarily high for any steady state system, however the event exist for tens of nanoseconds, and the pressures reduce significantly as everything expands. Vogue measured the shock wave pressure at a radius of 10 mm to be significantly lower at 2.62 MPa, 380 psi. That is to say that 85% of the shockwave energy would have dissipated upon reaching 10 mm from the point of inception. This idea highlights the importance of minimizing the distance between electrodes and the surface being drilled. As that length increases the plasma effects will be considerably reduced.

The bubble created from the plasma discharge will initiate with not only high pressures as noted above but also and very high temperatures. One source has measured this temperature to be on the order of 8000K [47]. At this point the origin will explode into a bubble of pressurized, hot gas. The bubble may expand and contract several times before sufficient energy has been depleted to cause the event to dissipate. This event has been studied under high ambient pressure by Sukovich [48]. It was confirmed that the characteristics inside these bubbles are quite extreme, especially at singularity. Sukovich produced cavitation bubbles within a pressurized media up to 4300 psi. He recorded images of the bubble event and plotted its size over time. He discusses at length the presence of a spheroid shape that often appears within the center of the bubble and resulting jets that emit from the bubble. Sukovich explains that the calculated pressures and appearance of these spheroid shapes encourage the possibility that Ice-VII (2.1 GPa) or Ice-VI (1.1 GPa) may have formed within this area. The possibility of these species being present bolsters the idea that this event is capable of destructive power despite its short time span and limited volume.

All things considered, the bubbles discussed above are not that different than a proper explosion. Albeit, the scale may vary between plasma generated cavitation bubbles and military grade explosions, perhaps some insight into substrate effects can be learned from the latter. A typical ambient plasma event can generate bubbles that grow to 1-2 mm, however a typical torpedo containing 500 kg of TNT will generate a bubble 10,000 time the size with bubbles on the scale of 10 to 20 m [49]. Immediately after an explosion the bubble grows similar to the plasma discharge. Upon reaching a size where the hydrostatic pressure around the bubble is larger than the pressure inside the bubble the bubble will began to shrink again. As the bubble starts to shrink it will attract to an near surface due to the Bjerknes effect. Klaseboer explores the effects of these cavitation bubbles against a thin steel wall. In his experiment a steel plate (yield stress 240 MPa) with a thickness of 2 mm is subjected to a 55 g explosion (approximately 250 kJ). This creates a bubble radius of 0.54 m, but the charge is placed at a distance of 2.2 times that value (1.2 m). After the discharge event the steel wall deflects 20-30 mm away from the bubble. After 20 ms the deflection inverts and the plate is attracted 15-25 mm toward the discharge. After 90 ms a sharp inversion occurs (likely after

singularity) where the wall again deflects 30-40 mm away. A pressure sensor at the center of the plate measures a peak pressure of 30 MPa. A tenth of a millisecond later the measured pressure had dropped to 5 MPa suggesting that the peak pressure is due to the initial shock wave. These experiments are orders of magnitude more powerful than a typical spark discharge, however it aids in highlighting two key components that may aid in drilling.

The first important effect is the shock wave and resulting spike in pressure. This pressure wave is expected to be capable of introducing cracks within the granite that will promote both larger chip size and lower cutting forces, two items necessary for efficient drilling. Further, if any substantial negative pressures can be obtained then the granite is likely to dislodge with little to no needed cutting force. The compressive strength of granite is roughly 131 MPa, however its tensile strength is only 4.8 MPa. If implemented correctly plasma should be capable of introducing flaws through shock waves and high pressures as well as weakening and dislodging the rock through negative pressures.

Hartlieb [50] explores these types of structural affects by altering the integrity of granite. In Hartlieb's experiment high power microwave irradiation is used to induce a network of cracks in an attempt to reduce the required cutting power. After 24 kW of irradiation they were able to observe a 22.5% reduction in required cutting force. This finding helps to encourage the cutting force advantages offered through plasma discharges. The following section discusses several drilling applications and techniques that have been studied and attempted. Many of them strive to utilize the energy focusing leverage discussed above.

2.6 Energy Focusing Approaches

Early ideas of pulsed plasma drilling date back to the 70s [51]. Since then there have been various approaches to electrically enhanced drilling. A report from Maurer Enterprises [52] discuss the various methods that were in development around that time. A large number of approaches were mentioned and many of them are discusses below in their more modern shape. Maurer mentions percussion drills, vaporization drills, keft cutting mechanisms, nuclear drills, electric arc drills, plasma drills, electron beam drills, laser drills, jet-piercing drills, flame drilling, microwave

drills, induction drills, spark drilling, electrohydraulic drilling, explosive drilling, and more. Many of these approaches are shown as merely concepts within Maurer's report, but several of these ideas have grown into proper technologies. In 1992 Kitzinger filed a patent for a very high energy plasma blasting drill [53]. His dramatic approach aimed to deliver a continuous 3 gigawatts of energy downhole. As with Kitzinger's technology, many modern strategies struggle to compete with the established drilling industry. In order to be useful, the technology must provide a notable advantage in either speed, cost, or capability. Modern mechanical drilling has been around for much longer than any of these newer energy based methods, and as such mechanical drilling has had time to become more efficient and cheaper. The bar is set high for incoming technologies but many breakthroughs are happening.

The discussion below details approaches that can be grouped into three categories. The first is pure energy drilling, where large amounts of energy are used concentrated into a laser beam, plasma, or similar method. These methods require large energy input and often excel are small, deep holes. The second approach focuses on concentrating mechanical energy. The first method discussed is very similar to a water jet where a small highly pressured stream of water is utilized to created a hole. The second discussed mechanical method utilizes sharp percussion impacts in order to break and dislodge its way through the earth. Lastly, hybrid approaches are discussed where traditional mechanical drilling is combined with an alternate form of rock weakening. Several of the discussed technologies share elements of importance with the primary method explored in this paper. Understanding their successes and struggles may offer insight toward future pitfalls or strengths of future plasma approaches.

Pure energy drilling is a derivative of the approach that is explored in this paper. The primary difference is that the items explored later do not intended to drill solely of their own power, but rather they are designed to enhance traditional drilling. Timoshkin [54] discusses a pure plasma approach to drilling through the use of a plasma channel for the purposes of "miniature hole drilling". A drilling device was constructed that used pulsed plasma at 40 kV with a capacitance of up to 0.3 μF. Using just the pulsed plasma they were able to drill through soft-medium sandstone at a rates

between 4-16 cm/min or 7.8-31 ft/hr. The plasma discharges were conducted at rates between 5 and 20 pulses per second. The resultant hole diameter was 50 mm. Timoshkin's minimum specific energy was calculated to be 400 J/cm^3.

The strong pulsed plasma approach discussed by Timoshkin holds promise. In addition to this paper, others have discussed the capability and feasibility of such systems. Sun [55] has taken the pulsed plasma system and tested it upon sandstone samples at pressures upwards of 35 MPa. Sun developed a pressure simulator where the test samples could be subjected to the pressures at a depth of 3000 m. The samples used were 0.4 m x 0.4 m x 0.4 m with a round hole bored in the middle that was 0.05 m in diameter and 0.2 m in depth. The electrodes were placed within the hole and provided up to 40 kJ of energy at 20 kV and 70 kA. At lower pressures Sun subjected the sample to 5 pulses and was able to identify several large cracks (300+ mm) on both the interior and exterior of the sample. As the confining pressure was increased the effect of the plasma was diminished. Experiments at 15 Mpa required 32.4 kJ (50% additional) as well as 3x the number of pulses in order to generated a 47 mm interior crack. This highlights how higher confining pressures tend to more greatly limit the effect of plasma, especially as the distance from the origin increases.

In 2018 Changping Li [56] developed a model in order to better understand the interaction between plasma discharges and rock substrates. Termed electro pulse boring in his paper, Li discusses the behavior pressurized plasma has and why it is effective at cracking rock. A distinction is made between electrohydraulic rock breaking and electro pulse rock breaking. The former is defined by an electric breakdown through water with a rock in the nearby vicinity. Electro pulse rock breaking requires the electric breakdown to occur inside of the rock sample. Li illustrates this idea through two opposed electrodes that have a rock sample placed physically within the spark gap. The forces of an electrohydraulic breakdown are primarily compression forces where the power from the discharge impacts the rock. Electro pulse discharges will generate regions of interior pressure leading to tensile failure. For this reason electro pulse discharges are better suited for rock destruction. While the electro pulse is shown to be more effective, it is also much more difficult to develop a system capable of capitalizing on this technique.

Li's simulations explain a number of important parameters for electrode configuration. It is shown that as electrode spacing is reduced the maximum electric field strength increases. However, as the electrodes are brought together the average electric field strength is lowered. That is to say the closer the electrodes, the more concentrated the energy will be. The same results were found when experimenting with the sharpness of the electrodes. As the tip angle of the electrodes is reduced (the tip becomes pointier) the maximum electric field is increased while the averaged field is decreased. Li found that an increase in voltage will improve the damage inflicted upon granite. This increase in effectiveness comes at the cost of reduced efficiency. Increased capacitance will improve inflicted damage at the cost to charging time and discharge frequency. In order to optimize this system, the electrode spacing and tip angle must be balanced in order to breach the required threshold to damage the rock. If they are too far beyond the threshold then energy will be wasted and rock at a further distance will remain unaffected. The voltage and capacitance can be adjusted in order to increase effectiveness at the cost of energy efficiency and power supply demand.

Pulsed plasma approaches tend to use their focused energy to impart a sharp physical pressure gradient in order to created damage. Pulsed laser drilling looks to focus energy in order to melt or vaporize the target substrate. While not suitable for the majority of wells, laser drilling offers some unique opportunities for micro-holes. Pastras discusses methods to model and analyze this pulsed laser drilling [57]. The laser drilling process can be broken down into four phases: the heating phase, melting phase, vaporization phase, and cooling phase. This cycles occurs within the time of one laser pulse. It was found that a laser's drilling depth is contingent upon the available laser power and duty. Primary efficiency concerns are due to material reflectively, laser beam defocusing, and heat conduction.

The drilling strategies discussed up to this point utilize electrically focused energy. An alternative is to focus mechanical energy in order to reach the same destructive results. Percussion drilling is a technique that takes a large mass and and supplies it with a great deal of kinetic energy. This mass then impacts the target rock resulting in crushed, cracked, and damaged rock. In the early 70's Hustruild [58] performed an in depth analysis to the capabilities of percussion drilling.

A general rate of penetration vs thrust force was found for several different situations. Hustruild stresses the importance of the impact rate and as well as wear prevention. Mahdi Saadati [59] has created a model that is capable of exploring the effectiveness of such a method. It was found that preexisting cracks in the granite substrate will reduce the required force to created penetration. Furthermore, subsequent impacts will benefit from the damage caused up to that point. Further studies were conducted by Han where he investigated percussion methods with the conditions of the oil and gas industry in mind. Simulations as well as full scale models showed that tensile failure was key during percussion events. The sharp impact from the hammer is sufficient to damage the rock up to several diameters below the impact. However, the associated tensile forces during impact and retreat are what cause the rock to dislodge. [60]

An additional mechanical energy focusing method can be found in a piece of common shop equipment, the water jet. The premise is that a stream of water can be pressurized and focused into a small area where it becomes capable of cutting through items. Often there is some type of hard garnet that is mixed into the stream in order to improve cutting capabilities. This technique can be extending into the drilling environment. Water jet assisted drilling utilizes these pressurized streams to create internal stresses within preexisting rock cracks. Liu [61] has published work that quantifies the effectiveness of such methods. So long as the jet pressure exceeds the rock critical stress than the jet will reduce the required drilling force. An increase of up to 24% drilling rate was reported. Furthermore, a properly tuned water jet was shown to reduce the vibration within the system that may yield longer drill rod service life.

It is likely that hybrid methods such at the water jet mentioned above or the plasma bit discussed in this paper offer the ideal entry into the drilling industry. The oil and gas drilling industry is comfortable with the processes that are in place. Due to the expenses associated with oil drilling there is high financial risk involved with adopting a new strategy. With this in mind it makes sense to look to hybrid drilling and small upgrades to the process rather than a full remake of the process. One said hybrid technology exists that utilizes extreme heat to pre-damage the rock before a tradition bit cuts it. The process of heating the rock has been accomplished in several different

ways.

In order for this heat approach to work the heat gradient must be extreme enough to thermally spall the rock. The spalling process will introduce cracks into the rock that then makes it easier for a traditional rotary bit to drill through. Kant [62] discusses a hybrid design that creates an intense flame downhole through the use of combustible materials that are pumped down the drill string. A fuel and an oxidizer are ignited just above the PDC cutter within a large combustion chamber. With Kant's research a methane and air burner is used that is capable of generating a flame up to 1300 °C. Excess pressurized air is released on the perimeter of the flame in order to concentrate the heat as well as to protect the other components of the bit. Several tests were conducted to analyze the effectiveness of the flame. it was found the at temperatures as low as 400 °C could reduce the strength of the granite by up to 40%. Temperatures up to 800 °C averaged about a strength reduction of about 40% but could decrease the strength up to 45%.

This spalling approach holds promise in providing improvements to drilling rates. In 2020 Edoardo Rossi published data that expands upon Kant's earlier paper [63]. Rossi shows a breakdown of feasible designs and tested the capabilities of the system. The required power of the rig is roughly 40 kW and it produces temperatures up to 400 °C at the flame igniter. The flame-assisted drill head was capable of progressing through 100 mm of granite in about 30 minutes. When the flame component was removed the bit was only able to progress approximately 40 mm in the same amount of time. Rossi reports the wear rate of the flame-assited bit to be 3.35 mm^3/min vs the purely mechanical wear rate of 2.97 mm^3/min. The flame-assisted bit wears faster in time, but is still much more efficient per distance drilled. The calculated ratio of granite removed vs wear of the bit is 17600 and 7100 for the flame-assisted bit and the mechanical bit respectively. This technology shows much promise if the additional required infrastructure can be properly and cleanly implemented into tradition drilling processes.

The strategy discussed in Kant's paper requires a specialized bit as well as 2 additional gas lines to be plumbed through the drill string to the drill bit. An alternate approach to rock spalling may avoid those requirements. A high intensity laser has been shown to provide sufficient heat to intro-

duce additional cracks within the rock. Buckstegge investigated the capability of utilizing a high power disc laser system at 1030 nm wavelength. Similar to subjecting the rock to a flame, a laser can introduce a sharp temperature gradient that will yield damaged rock. In addition to spalling the rock, the laser will melt a volume of the rock resulting in further rock removal. A parametric study was conducted that investigated the specific power required to melt and remove the rock. It was found that the laser can achieve a rate of volume removal of around 5 m^3/h in hard limestone. The specific energy for this test was 40 J/mm^3. The power to maintain those removal rates is 55.56 MW. As a result it was determined that a pure laser approach is not economical. Instead, laser power paired with mechanical ablation is noted to be the preferred method. It was found that a 500 W laser can heat several μm^3 to 600 m^3/h within a few milliseconds. Unfortunately, within the test conducted Buskstegge was unable to clearly identify any spallation damage within the rock. It is noted that higher powers and longer cooling times may generate better conditions for spallation.

As discussed in the above approaches, hybrid methods seem to hold the most promise. In 2009 Moeny filed a patent for a pulsed electric drill head [64]. Money's approach is very similar to the design discussed in this paper. However this patented design utilizes higher energy plasma in conjunction with a mechanical drill head. Money's patent notes using plasma to more completely dislodge and break rocks as opposed to optimizing the discharge to create internal cracks. This is an important consideration as downhole power is very limited and producing the excess of power required for rock obliteration is not practical. By boosting modern drilling techniques with lower power discharges ROP in this system can be maximized while remaining within present day downhole power constraints. This optimization is only possible if there is an understanding of the necessary plasma characteristics. The remainder of this paper discusses the research and findings of the Staack plasma lab to better understand and optimize this plasma drilling hybrid technology.

3. EXPERIMENTAL SETUP

In order to perform the proposed experiments a test setup capable of generating plasma inside of a pressure vessel was created. This system is comprised of four major systems: the pressure vessel, the electrode assembly, the RC charging circuit, and the diagnostic system. The resulting system is capable of generating plasmas up to 25 kV, pressures up to 440 atm (depending on the configuration), and visual information about the resulting discharge. The pressure vessel, RC charging circuit, and diagnostic equipment are comprised of purchased items. The electrode assembly has been custom designed and 3D printed. The following sections discuss the expense, complexity, and design of all four systems.

3.1 Pressure Vessel

3.1.1 Requirements

The pressure vessel requirements necessary for high pressure discharge analysis are outlined in table 3.1. Initial investigation indicated that off the self reactors capable of meeting the pressure and voltage electrical feed requirements are obtainable. However, many reactors under the $10,000 price mark lacked viewing ports. Consideration was given toward creating an in house custom vessel; however, it was quickly discovered that certification of a vessel at the magnitude would easily exceed the expense requirement. Further investigation of pressure rated components found that specialized NPT fittings are commercially available, affordable, and rated up to 680 atm.

A bill of materials consisting of NPT high pressure rated parts and a corresponding CAD model were created. Table 3.2 identifies the components of the pressure vessel and their associated cost. Due to the variety of key components, a number of adapter fittings were required to ensure compatibility throughout the system. The primary pressure constraint within the system is 420 atm due to the limitations of the quartz sight glasses. This constraint may be bypassed through replacing these viewing windows with solid plugs. However, installing the plugs will eliminate the visibility of the test area. These changes will raise the available testing pressure to the limitations

Requirement	Notes
Pressure	300+ atm
Pumping Rate	Less than 5 minutes
Vision	Clear linear sight through test area
Electrical Feed through	High voltage power in/out
Pressure Release	Ability to safely release testing pressure
Safety	Controlled pressure release upon over-pressurization
Compliance with other system components	Usable with electrodes, charging system, and diagnostic equipment
Cost	Maintain a reasonable cost, preferably under $10,000
Lead time	Obtain parts and components within 4-8 weeks
Optional: Fluid Acceptance	Accept oils, acids, or alcohols

Table 3.1: Pressure Vessel Requirements

of the electrical feed through, 525 atm.

Selecting a design that utilizes off the shelf fittings has allowed for several key advantages. The cumulative cost of the bill of materials comes to $3151.50. This cost is dramatically cheaper than a prefabricated vessel or machined build. The sourced items are already pressure rated and designed for the testing conditions. This allows the unit as a whole to bypass additional certification requirements as all items are rated for the testing conditions. Utilizing cross fitting as the core of the vessel allows for a modular, easily modifiable design that may be retrofitted for additional or altered requirements. This flexibility is notable as testing conditions and needs are expected to change over time. This design meets all listed requirements and is cheap in comparison to other approaches. However, it comes with limitations and poses design constraints on other systems.

The size of the vessel becomes an important constraint in order to meet the 300 atm pressure requirement. As internal volume scales, the required wall thickness quickly increases. Assuming

Table 3.2: Bill of Materials

	Item	Manufacturer	Part Number	Cost
Key Components	1" NPT Cross	Fitok	SS-HPCR-NS16	$157.97 (2)
	3/8" NPT Cross	Fitok	SS-HPCR-NS6	$40.18
	Pressure Gauge	Fitok	GA-63-NS4-10000PM	$85.71
	Electrical Feed Through	Conax	HEGPK-125-A-CU	$350.00
	Pump	Sprague	SM-3S-100-H	$890.77
	Pressure Release Valve	Hawk Valve	15F-11NFC	$112.00
	Rupture Disk Fitting	Hawk Valve	15-61NMC	$64.50
	Sight Glass	Encole	324A1003	$404.68 (2)
Adapter Fittings	1" NPT x 1" NPT	Fitok	SS-HPHN-NS16	$41.79
	1" NPT x 3/8" NPT	Fitok	SS-HPHN-NS16-NS6	$41.79 (2)
	3/8" NPT Quick Connect	Fitok	HQCSS-NS6-CP	$117.49
	1/4" HP Quick Connect	Fitok	HQCSS-6MP4-NP1	$20.38
	1" NPT x 3/8" FNPT	Fitok	SS-HPA-NS6-NS16	$52.28
	3/8" NPT x 1/4" FNPT	Fitok	SS-HPA-NS4-NS6	$22.92
	1/4" HP x 3/8" NPT	Hawk Valve	30-21HM4NMC	$64.50
	1/4" NPT to 3/8" Hose	Hawk Valve	15-21NMBHA12	$42.50
	3/8" NPT to 3/4" Hose	Hawk Valve	15-21NMCHA12	$37.60
			Total:	$3151.50

that the vessel behaves similar to a pressurized cylinder, the approximate applied stress can be found using equation 3.1. In order to maintain a high pressure at a safe stress the vessel radius must be minimized or the wall thickness maximized. As a result it is very difficult to source large fittings that are rated for extreme pressures. The one inch cross was the largest available item that could be found for the pressure ranges of interest. The working space dimensions is shown in figure 3.1. This tight space makes it very difficult to maneuver equipment or samples within the vessel. A number of 3D printed components were utilized in order to alleviate the issues associated with this limited space.

$$\sigma_h = \frac{Pressure * Radius}{Thickness} \tag{3.1}$$

A sturdy high voltage electrical feedthrough rated to the working pressure of the vessel was also

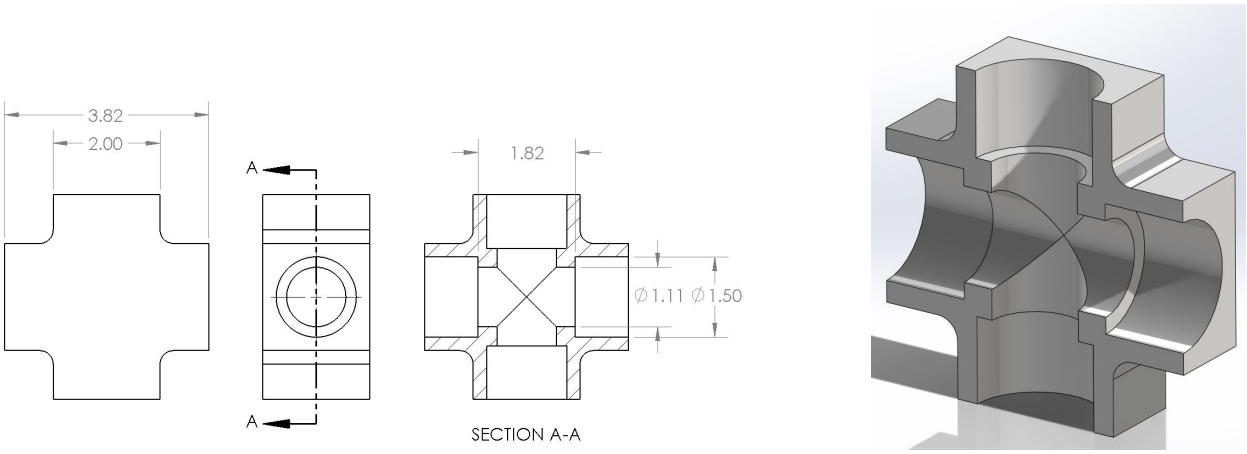

Figure 3.1: Working Space

required. Unfortunately the pressure and voltage ratings are competing characteristics as larger voltage ratings require more insulation but larger feedthroughs are less capable at high pressures. Two different feedthroughs were sourced through Conax that independently excel at either rated voltage or rated pressure. Their capabilities are shown in table 3.3. It was decided that voltage is the primary constraint for the system. If breakdown voltage is unable to be achieved, then the testing conditions are irrelevant.

Table 3.3: Conax Feedthroughs

	Voltage Rating	Pressure Rating	Cost
HEGPK-125-A-CU	8000 Volts	525 atm	$350
EGVSP-069-A-CU	15000 Volts	170 atm	$1200

The HEGPK-125-A-CU electrical feedthrough was installed to ensure this freedom when experimenting with testing pressures. As expected, there were issues in being able to reach breakdown voltages without exceeding the voltage limit. In order to achieve breakdown, the voltage rating was neglected. The resulting potential failure was considered non-dangerous as a voltage failure would simply result in an unexpected breakdown from the center of the feedthrough to the frame of the vessel. This type of failure would likely yield microcrack destruction of the insulating

material ruining the feedthrough. During testing the input voltage was raised cautiously, as need. After numerous tests it was determined that the feedthrough would operate safely and properly up to voltages of roughly 20000 volts. Upon pushing the feedthrough to higher voltages a failure occurred. At roughly 25000 volts the insulating material gave way and a premature breakdown occurred between the inlet wire and the feedthrough housing. A second, identical feedthrough was used to replace the damaged item. All following tests the voltage and feedthrough were watched closely.

A 3D rendering of the Conax Feedthrough is shown in figure 3.2. There are five elements to the feedthrough: the conductor, insulator, base, compression fitting, and spacer. The conductor consists of the orange piece running through the center of the assembly. It is a solid copper rod with threads on either end to allow for exterior inputs. The insulator is the peach colored part bordering the conductor. The purple and pink exterior parts are the base and compression fitting respectively. Lastly, the grey part is the spacer. The geometry of the insulator creates a compression fitting between both the base and conductor. Threads on the compression fitting allow it the screw in the base fitting resulting in the spacer to applying pressure on the flared portion of the insulator. This pinches both the conductor and insulator inside the base fitting. This geometry allows for an effective seal up to the rated pressure. The thickness of the insulator is what determines the voltage rating. A thicker insulator or stronger insulator will require a larger electrical potential to create unintended breakdown. Customizations to these components offer the potential to improve upon the rating as needed.

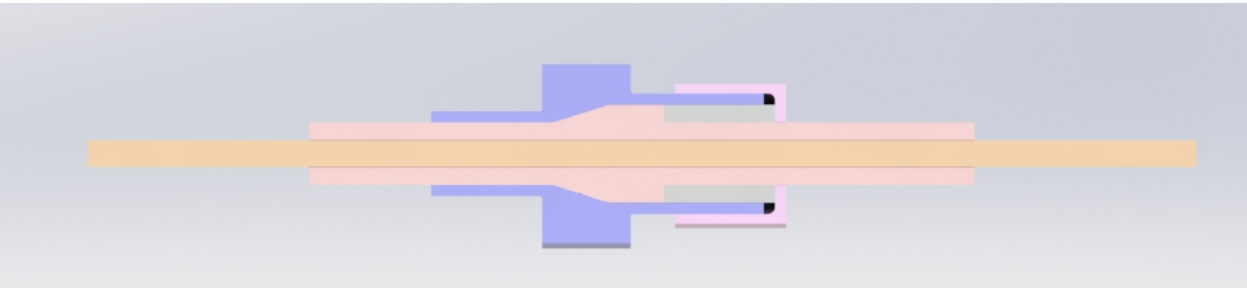

Figure 3.2: Conax Feedthrough

3.1.2 Setup and Troubleshooting

The assembly of the pressure vessel was tedious but straightforward. Each connection was carefully wrapped with Teflon tape and wrenched together. All of the connections are standard NPT which have tapered threads and a set engagement length. This created a small issue where the system had no flexibility upon the orientation of its components. Once tightened sufficiently tight to prevent leaks, each connection had roughly 1/4 turn of flexibility. The initial build resulted in an upside down, difficult to read pressure gauge. Despite the inconvenience, all aspects of the vessel operated as expected.

In order to secure the vessel a custom mounting interface was assembled. A simple rig made of square tubing was designed to create a connection between the pump and the optic table. Once installed, the pump and attached pressure vessel were securely fastened onto the optic bench. Further modifications were added to raise the entire assembly and hold the water reservoir. Upon completion the pressure vessel was constricted to one degree of freedom where it could pivot across the central axis of the pump.

Over the course of several experiments a number of items were addressed. Initially there were a few small leaks, mainly from around the sight glasses. Verifying that all of the connections were adequate torqued ensured that the leaks subsided. The flexibility limitations of the vessel began to cause issues with positioning a camera and light source for the visual experiments. A pressure rated quick release connection was installed between the pump and the vessel. This new connection allowed for another degree of freedom as well as the ability to disconnect the entire vessel if needed.

In order to maintain a good seal, all of the fittings are wrapped with Teflon tape prior to installation. The use of Teflon tape is essential for the functionality of the vessel, but it has also created an issue of foreign object debris (FOD). As fittings are installed and removed shreds of leftover tape tend to accumulate within the vessel. In addition the tape, dirt and other particles eventually pollute the water within the vessel. The small working space and complex interior geometry make it very difficult to remove FOD. Attempts to filter incoming water and carefully manage Teflon tape

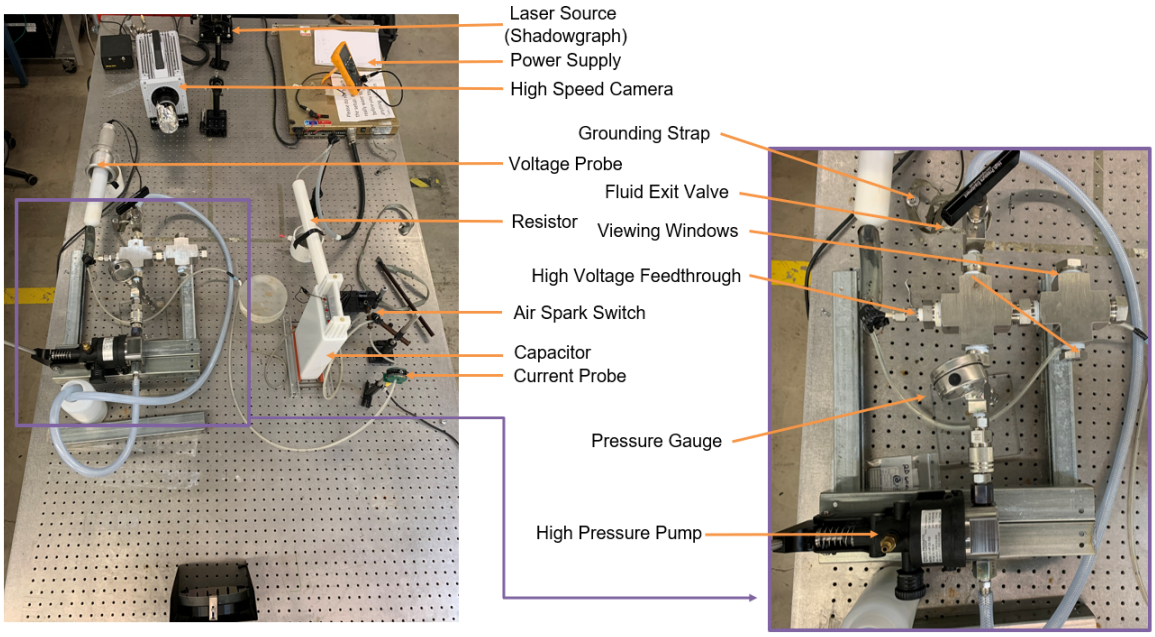

Figure 3.3: Experimental Setup

while sealing the vessel have allowed for marginal improvements concerning this issue. Figure 3.4 demonstrates the potential FOD issues associated with Teflon. Additional care and considerations to resolve this issue may be required at a future point.

3.1.3 CAD Model

A Solidworks CAD model was created in order to better understand the fit, form, and function of the pressure vessel. The shape and dimensions have been populated using any available information from suppliers in conjunction to physical measurements gathered from the parts. In order to keep the model simple fitting threads have been excluded. This allows for swifter modeling time while maintaining the ability to understand the role and fit of all components within the assembly. Figure 3.5a shows an overview of the vessel. Pressurized fluid leaves the pump and enters the vessel upon the opening on the right fitting. The pressure release valve on the left provides a means to depressurize the system. The cross sectional view shown in figure 3.5b reveals additional information on the inner working of the system.

This model was utilized to verify the bill of materials and to understand the fit of components

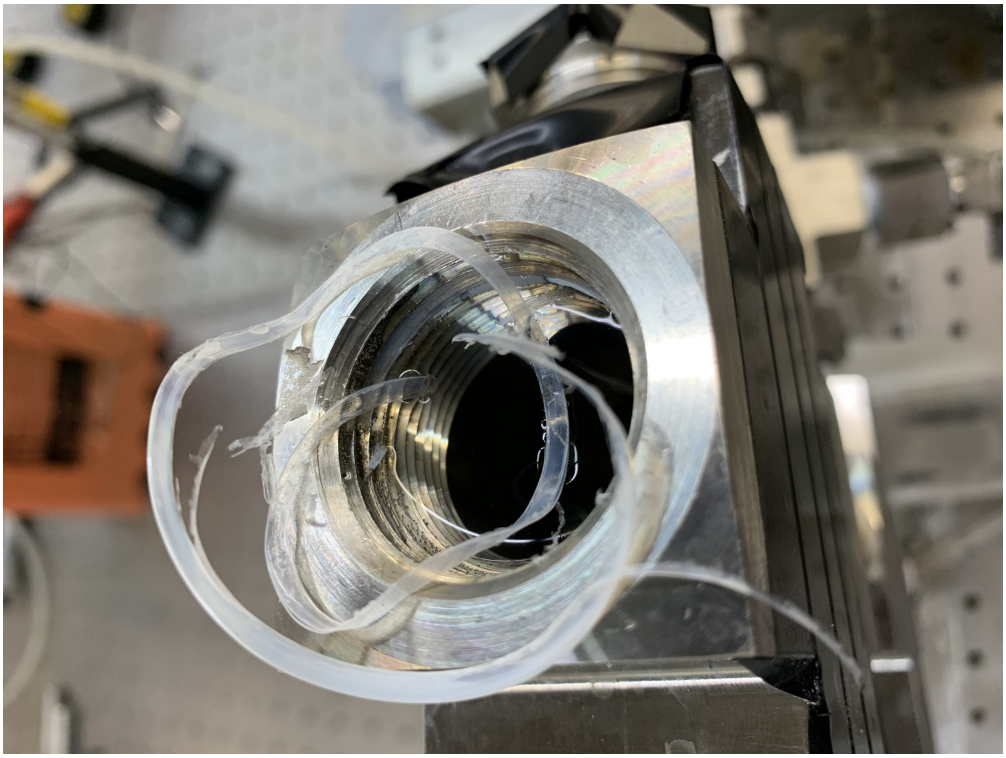

Figure 3.4: Foreign Object Debris

of the experiment. The working space measurements provided the information needed to produced 3D printed parts that create an interface between the electrodes, specimen, and the vessel itself. This interface has proved to be a primary design challenge as there is very little space within the vessel and even less accessibility. The following section discusses the challenges and requirements associated with internal mechanisms of the vessel.

3.2 Internal Designs

3.2.1 Feedthrough Sleeve

The high voltage requirements of the system require that any junction along the high voltage path must be insulated from ground to prevent accidental discharge outside of the test area. The vessel as a whole is used as the grounding point and therefore appropriate separation must be kept at all uninsulated points. The geometry of the feedthrough and its adapter create a concern with this issue. Figure 3.6 details the geometry within this area. A 3D printed sleeve (shown in

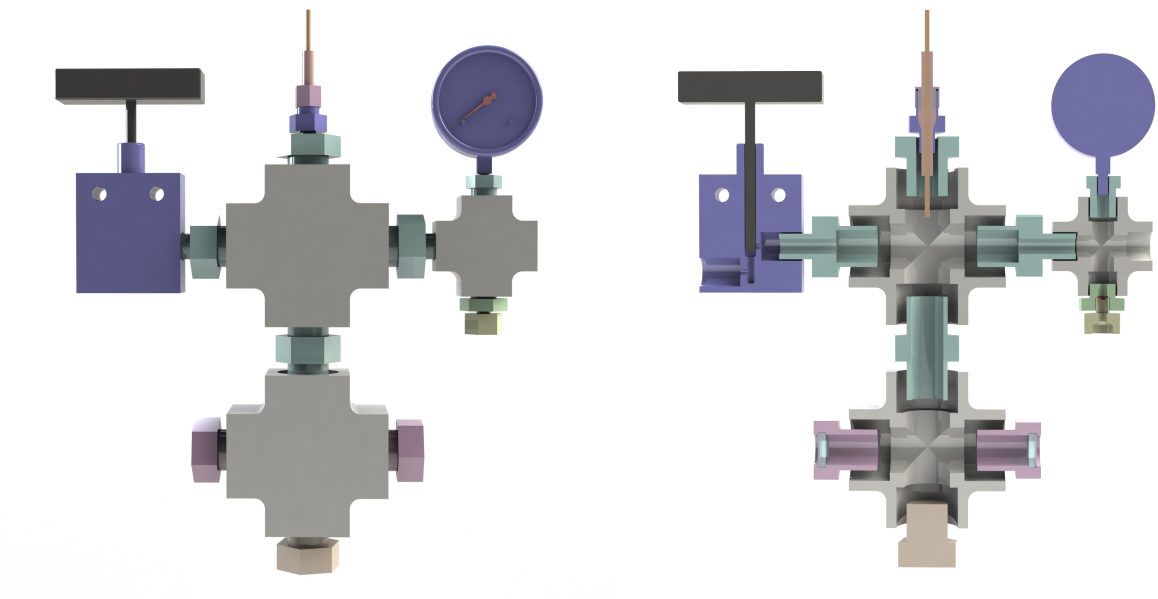

(a) CAD Model (b) CAD Cross Section

Figure 3.5: CAD Models

green) was designed to help create separation between the feedthrough and the vessel. Due to the requirement of a NPT adapter the feedthrough's insulation does not extend to a safe distance. The sleeve creates a physical, non-conductive barrier between the high voltage junction and the NPT adapter (shown as transparent). To further improve the performance of this mate the sleeve is filled with a non-conductive substance such as petroleum jelly.

3.2.2 Electrode Configuration

One of the most difficult challenges involved with the experimental setup was creating a configurable and accurate electrode arrangement within the limited volume. Several iterations of electrode configurations were used throughout the testing process. The requirements point toward an over-constrained design space resulting in lacking designs. Within the considered design space, an approach that meets all of the requirements has not been identified. Instead, each iteration of the design has made advances that improve upon issues present in previous approaches. The final internal design is shown in figure 3.7.

The wires present are silicone insulated 40 kV wires. This type of wire is used throughout the

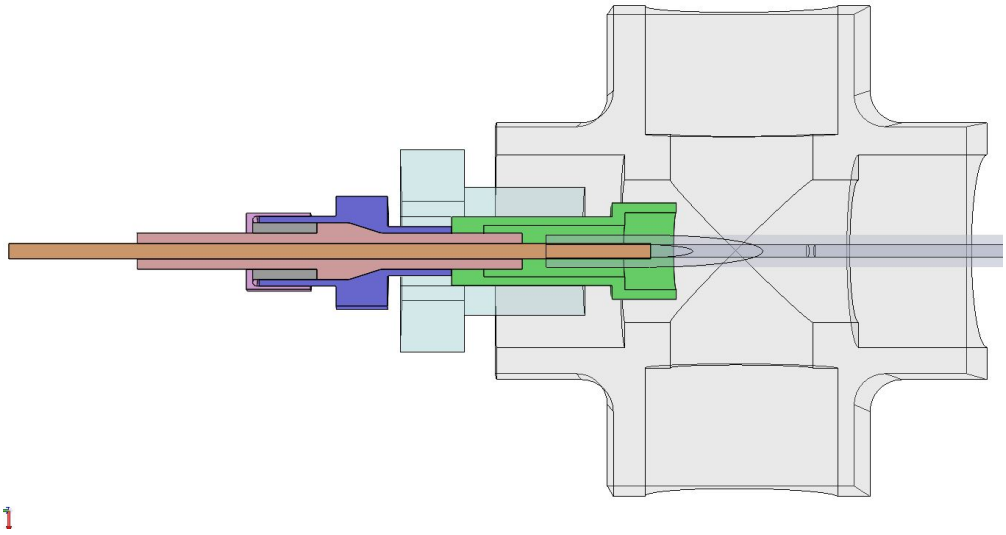

Figure 3.6: Feedthrough Sleeve

system on both the interior and exterior of the vessel. In addition to high rated wires, additional precautions have been taken ensure that inappropriate breakdown does not occur on either side of the feedthrough or elsewhere within the vessel. The orange wire shown in figure 3.7 carries current from the feedthrough to an electrode. The green wire is brazed onto the vessel and connects to the second electrode. In conjunction, an electrical potential between the high voltage input and ground connection is created.

The wiring of the system remained fairly consistent throughout the testing period. The consistency was more to do with a lack of flexibility than the satisfaction of the approach. The wires shown in figure 3.7 have been shortened for simplicity and clarity. In reality it is necessary for each wire length to extend past the bottom opening to allow for electrode-wire installation as well as electrode-holder installation. While this in of itself is not an issue, compressing the resulting wires and assembly back into the vessel has proved to be an inconvenience. The wires are fairly flexible, but their minimum radius of curvature is between 0.5-0.75 inches. Due to the silicone insulation a coiled wired will naturally attempt to spring back into its straightened shape. The electrode assembly is assembled outside the vessel near the bottom opening. It is then positioned

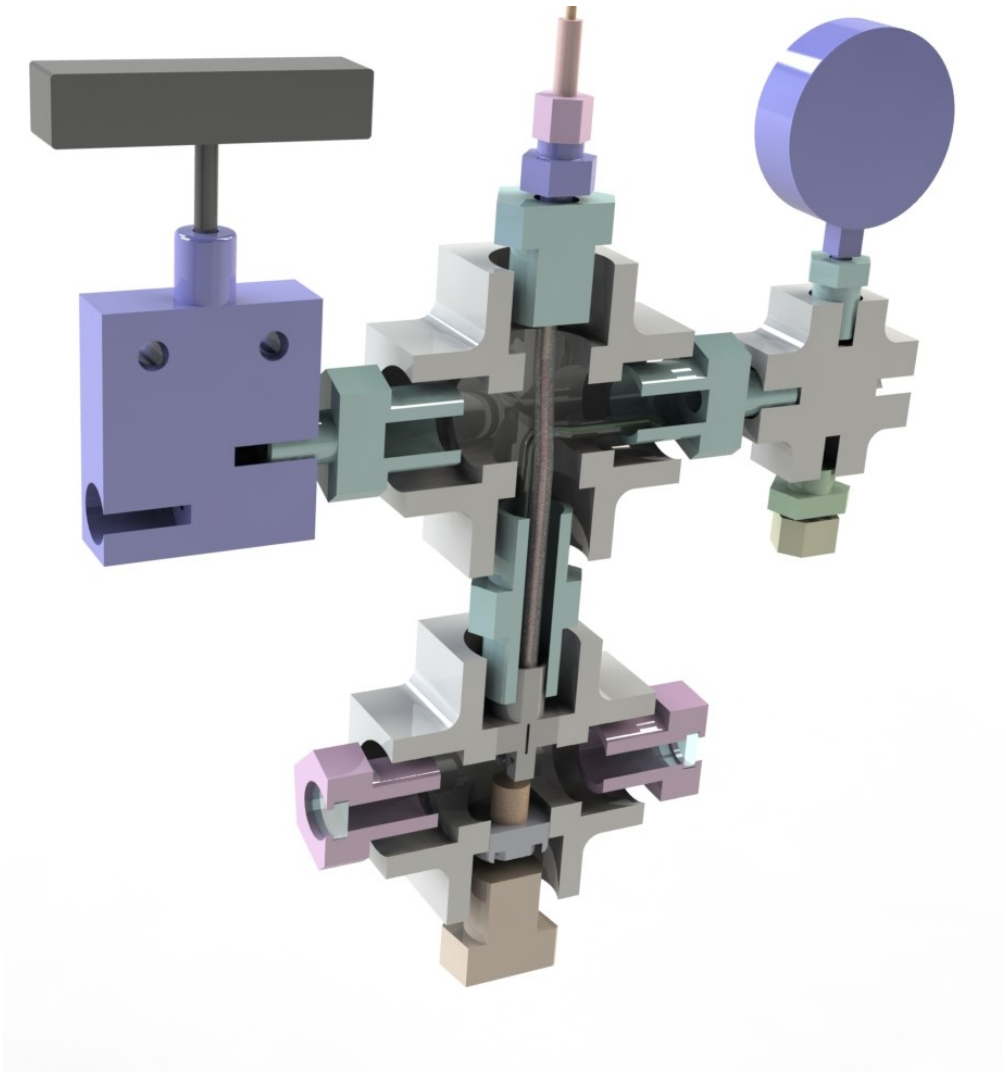

Figure 3.7: Electrode CAD

by pulling both wires from the top of the vessel until the electrodes are fully in place. The excess wire is then tucked to the pressure relief side of the upper cross.

At this point in the installation process the only remaining steps are to install the feedthrough, sample, and lower plug. The sample and lower plug installation are trivial. The sample is secured onto a friction fit 3D printed holder and placed inside the vessel. The plug is wrapped with teflon tape and torqued onto the vessel. Securing the feedthrough is typically straightforward but difficulties have been encountered throughout the testing period. As the feedthrough is screwed into the vessel the high voltage wire spins in conjunction with the feedthrough. This has caused the

electrode assembly to spin or displace out of the line of view in the testing space. On a single occasion the torsion from this event was sufficient enough to break the welded connection between the grounding wire and vessel resulting in complete disassembly of the vessel and the reconnection of the wire. An additional step of counter-rotating the feedthrough before installing was added the the setup procedure. This step seems to have alleviated the torsion issue in part. An additional "clock stop" solution is discussed below as a part of the final iteration.

A handful of approaches and strategies were employed in order to design a successful electrode assembly. Consulting with several colleges as well as Dr. Staack helped to encourage advancement in the design. The key requirements of this system are outlined in table 3.4. Several minor constraints and discovered issues are discussed below and not included within this list. There have been five primary iterations of the electrode assembly and rock holder. The initial four iterations are show in figure 3.8.

Table 3.4: Electrode Requirements

Requirement/Constraint	Notes
Stable gap	Electrode gap must not vary in between experiments
Rigid electrodes	Electrodes must not deflect during breakdown
Equal electrode height	Electrodes must meet at equal distance from the base
Adjustable electrode gap	The electrode gap should be tunable between 0.5 mm and 3 mm
No rotation	The electrode assembly must not rotate
Can be assembled	Components will assemble within the given volume
Electrodes touch substrate	The electrodes must extend far enough to make contact with the rock
No improper breakdown	The wires and electrodes do not breakdown to the sidewalls

Iteration one of the electrode assembly, shown in figure 3.8a offered a nice baseline design but lacked in many aspects. The pink sample support contains a deep counterbore that allows it be fasten to the lower plug within the vessel. The electrode assembly then notches into the sample support. The distance between the sample and the electrodes is set by this mate. Furthermore, it forces the lower plug, specimen holder, and electrodes to be clocked together. It is important for the plane of the electrodes to be perpendicular to the line of sight through he sight glasses. If the

electrodes are off axis they will obscure the breakdown region between the two electrodes. While it is possible to control the orientation of the assembly, it is difficult to tune their position. The lower plug has fairly small flexibility regarding its length of engagement. That being said it is difficult to match the exterior tuning with the fully positioned, screwed in orientation. Trial and error in conjunction with positioning marks help to alleviate this problem. Further issues arise due to the resulting wire torsion from installation. It is believed that this is a primary reason the grounding wire broke free from the interior weld of the vessel. All four primary iterations share these clocking and wire torsion issues. The designs of versions 2-4 move toward a base that is secured with two bolts and a slot that allows for additional holding power while maintaining some degree of rotational flexibility. The slots provide a hard stop that limits the occasional free spin that occurred within version one. A side effect of this design change forced the body to be hollowed out and side openings to be added for bolt access. These provided minor improvements to the clocking issues but offered space and flexibility for future changes.

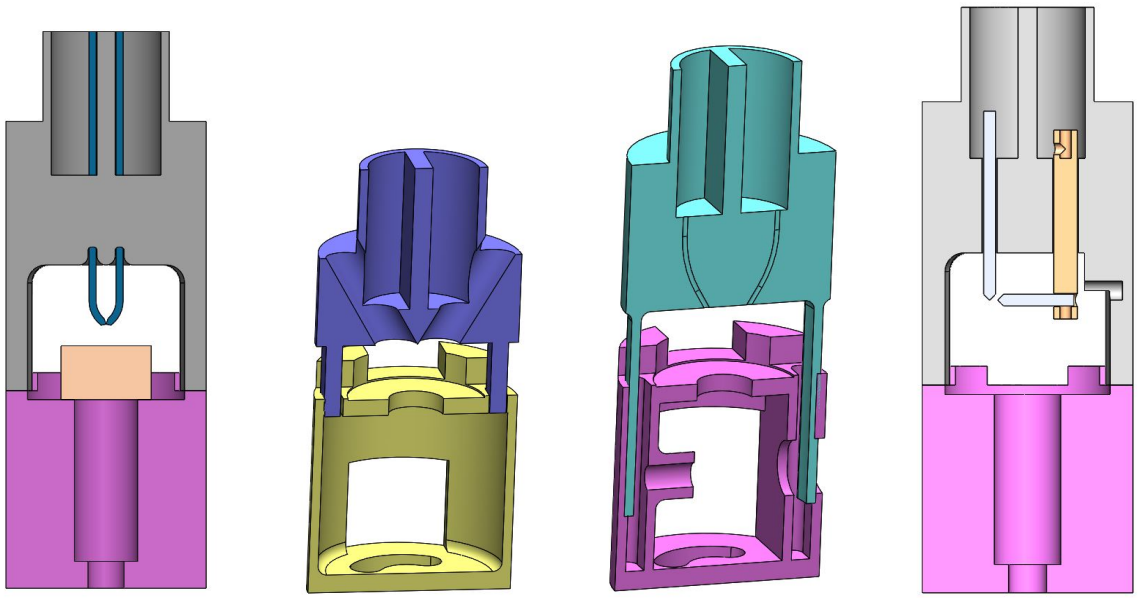

(a) Version 1 (b) Version 2 (c) Version 3 (d) Version 4

Figure 3.8: Iterations 1-4

Experiments conducted with the version one indicate that the electrode to substrate distance is critical. The flexibility of this design variable is limited within the version one layout. Iterations 2 and 3 focus on controlling the electrode/substrate gap in addition to the inter-electrode gap. An opening was added to create a degree of freedom along the gap direction. Version two allows the electrode assembly to slide freely toward the rock. Testing showed that while there was now a degree of freedom, it was variable and difficult to control. Version three makes an effort to secure the vertical position of the electrodes. The opening was changed into a channel, and a boss was added for set screw threads. Other minor changes were made to allow for these features. These channels prove to be difficult with regards to the nature of the 3D printer. After printing the channels were sticky and difficult to clean. Furthermore, they would create a vacuum making it very difficult to separate the two pieces. Adding a drain hole and additional curing time resolved this issue. Version four shown in 3.8d focuses on controlling the inter-electrode gap and therefore the simplified mate from version one was used.

The above designs inspired new design concepts, concerns, and requirements. Experimentation and several iterations resulted in the finalized design shown in figure 3.9. Three key requirements that were struggled with in previous designs were properly managed within this design. The distance between the sample and the electrodes is easily minimized by allowing the sample and its holder to float. Upon installation the sample can be positioned in contact with the electrodes or it may be spring loaded to ensure consistent contact. Secondly, the gap requirement between the electrodes that was found to be critical, especially at higher pressures, was resolved by utilizing electrodes that were not 100% tungsten. Tungsten is naturally very hard and brittle with a high melting point. When used as an electrode tungsten will maintain it's integrity much longer than most other materials. This design requires the electrodes to be flexible, however. A compromise was found by using electrodes that were a blend of tungsten and other materials; as these are capable of bending without brittle failure. In order to adjust the electrode gap the electrode can be pulled up/down within the electrode holder. The angled side walls will force the electrodes closer together as more electrode is pulled out. The flexibility within the sample holder maintains the

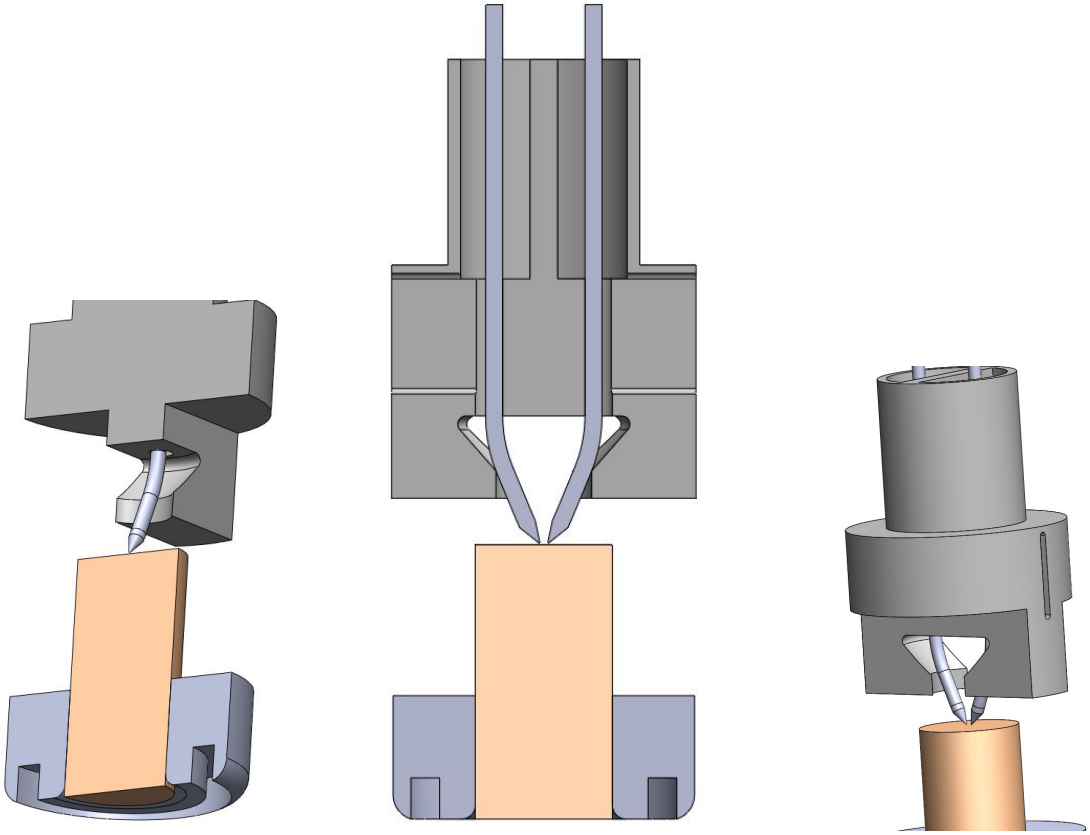

Figure 3.9: Final Iteration

electrode/sample distance despite the variation of electrode position in the vertical axis.

The final design issue that this iteration resolved is the rotational variation. The electrodes tend to spin freely, sometimes obscuring the discharge region. A 3D printed component was added to the system referred to as the clocking guide. This guide can be seen as the green piece in figure 3.10. Finding a solution to this problem that would not obscure the field of view or the ability to adjust the electrodes was difficult. The part is a tube that is oriented on line of view axis that has been sized to not obstruct vision. In order to install the guides the viewing ports on either side of the vessel have to be removed due to the lack of flexibility within the system. The component can slide freely along the axis of view allowing for them to displace in order to remove the electrodes when need. When the guides are positioned correctly it helps to keep the electrodes perfectly oriented within the field of view. They will also prevent the electrodes from sliding down in the

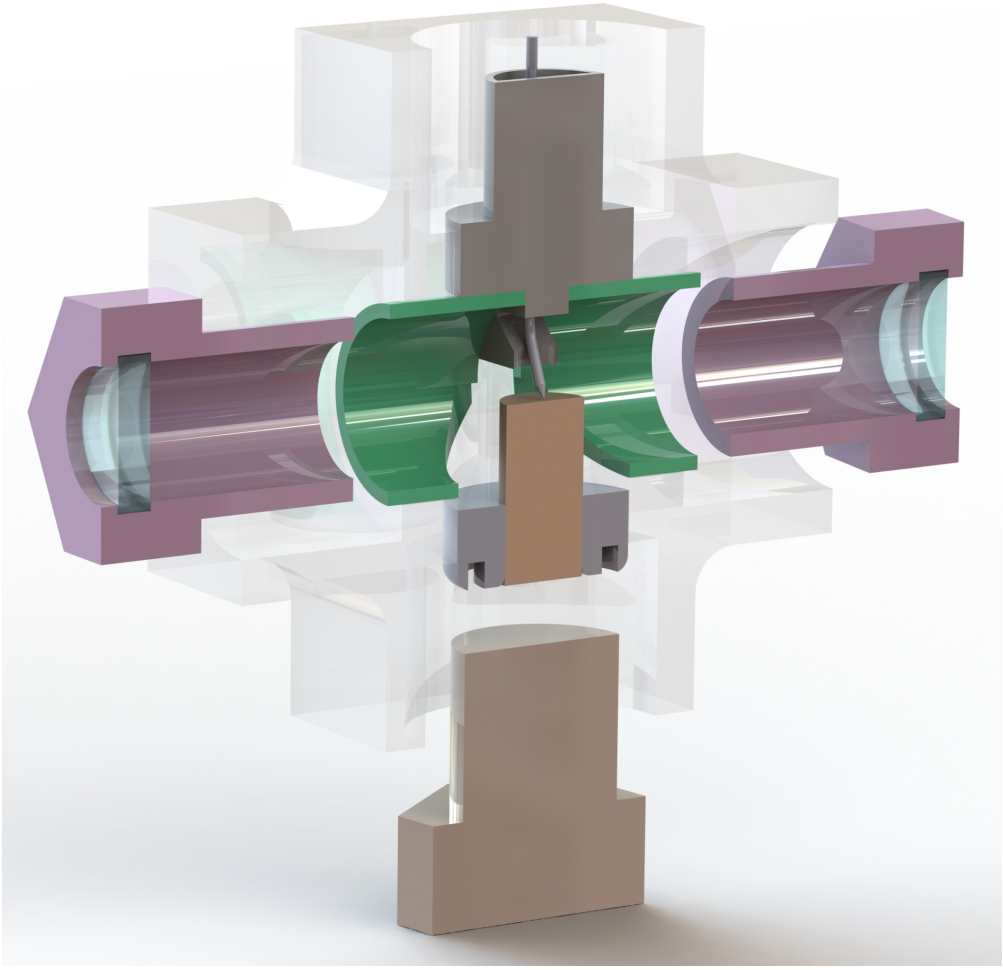

Figure 3.10: Clocking Guide

vertical direction.

The collection of the items discussed above work together to produce a vessel capable of producing reliable plasma discharges at pressures up to 400 atm. It took several iterations and creative solutions to reach this system with the versatility and consistency that is offered. The system is far from perfect, but it offers a reliable platform to gather imaging data, electrical data, and plasma feasibility within downhole conditions. The next phase of experiments will require a new vessel capable of increased temperatures, a rotary feedthrough, and a significantly increased working volume. The lessons learned while constructing and using this vessel will help to ensure that the upgraded vessel is design as best as possible.

3.3 Equipment Specifications

3.3.1 Resistor Capacitor Charging System

The electrical system used to create a nanosecond pulse discharge is a resistor-capacitor charging system in conjunction with an air gap spark switch. The circuit diagram for this setup is shown in figure 3.11. The power supply provides power to the system and the capacitor charges resulting in the gradual increase of voltage within the charging circuit. Once the voltage threshold of the air gap spark switch is met a plasma channel will form allowing for current to travel out of the charging circuit toward the primary plasma discharge. If the voltage is sufficient to generate a second plasma channel at the plasma discharge then a successful discharge will occur until the available energy can no longer sustain the discharge and the system will return to its charging state. If the voltage is insufficient to generate a plasma discharge at the load location then the current will stall and the voltage will bleed off through the various inefficiencies within the system.

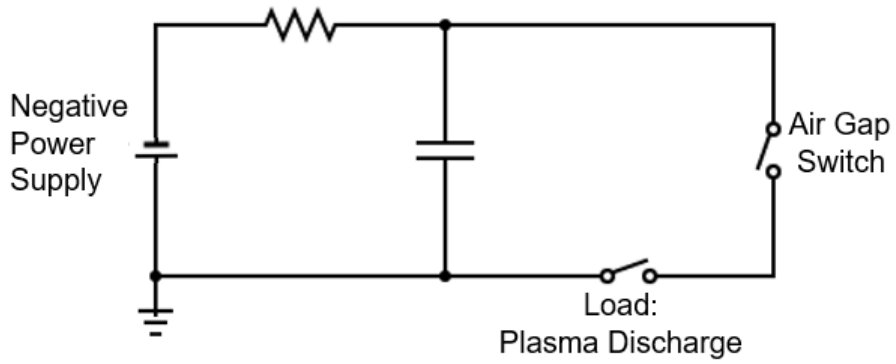

Figure 3.11: Circuit Diagram

3.3.2 Electrical Equipment

The power supply used within this system is the Spellman SL300. The exact device used is pictured in figure 3.12. Due to a damaged display, the proper output voltage is displayed on a multimeter connected to the rear pins of the power supply. This device will reach -100kV with a

current up to 3 mA. The wattage rating is 300 watts. The specific model number of this Spellman is "SL100N300/NAD/NSS/No".

The oscilloscope used in this project is the Tektronix DPO 3054, show in figure 3.13. This scope features 4 analog channels with a bandwidth of 500 MHz. The calculated rise time at 5 mv/div is typically 700 ps. The sampling rate of the analog channels is 2.5 GS/s with a recording length of 5 million points. Due to the high voltages and currents that occur during experiments, an attenuator is used to reduce the signal into the oscilloscope's range. The trigger feature is used for many experiments to activate either the high speed camera or ICCD. The trigger is capable of detecting a 0.50 div change at 50 MHz.

The current probe and voltage probe are pictured in figures 3.14 and 3.15 respectively. Both devices are fairly straightforward in that they measure the electricity within the circuit then send an output signal of volts within a magnitude that the oscilloscope is capable of recording. The current probe outputs 0.01 volt per Ampere at an accuracy of $\pm 0.5\%$. The probe has a rise time of 20 nanoseconds and can measure a maximum peak current of 25,000 Amperes. The voltage probe on the other hand is rated to 40 kV DC or 60 kV of pulsed voltage. The probe will output 1 volt for every 1,000 measured volts. The rise time of the device is 2.5 ns and its accuracy depends on the Hz within the system. DC - 2 Hz signals will carry an error of up to 0.15%. However, signals above 5 Mhz may contain errors up to 5%.

The system typically utilizes one capacitor, but a second one may be added when higher energy discharges are desired. The two capacitors used for these experiments are shown in figures 3.16 and 3.17. Both capacitors have a capacitance of 0.10 μF. The larger white capacitor is rated to voltages up to 100.0 kV while the smaller orange capacitor is only rated to 60 kV. When fully charged at 100 kV the white capacitor will store 1 kJ of energy. Under maximum conditions, the orange capacitor will store 360 J of energy at 60 kV.

The spark switch used within this system was made in house and is pictured in figure 3.18. The switch consists of two acorn nuts that have been positioned at a sufficient distance from any potential grounds. The powered side of the switch is used as a junction for both the power supply

and the capacitor. Furthermore, it has been positioned on top of a micrometer stage to allow for the switch gap to be accurately positioned. By increasing the gap between the two acorn nuts the voltage to the downstream components (pressurized plasma discharge) can be increased as desired. Due to the intensity of the discharges, the acorn nuts occasional become pitted and damaged. Their integrity is monitory and they are replaced as needed.

3.3.3 Imaging Equipment

Two imaging devices were used to record the plasma discharge events. A high speed camera was used to gather top level characteristics and bubble dynamics while an Intensified Charged Coupled Device (ICCD camera) was used to image the plasma event itself. The camera that was used is the Photron Fastcam SA5 pictured in figure 3.19. This camera is capable of recording at a frame rate as high as 1,000,000 frames per second with a resolution of 128x24 pixels. At this maximum frame rate it is very difficult to extract useful information due to the limited resolution. As a result, a frame rate of 11 μs with a resolution of 256x256 was used for many experiments. The intensity of the plasma event will saturate the camera during all frames that it occurs. This intensity typically lasts 15-20 μs which results in one to two frames of the video. Due to these limitations, the high speed offers limited usability when attempting to image shock waves or the event itself. The camera excelled at providing clear images of the resulting bubble and any pressure gradients (when shadowgraph and schlieren methods were used). To ensure correct image timing a trigger from the oscilloscope or ambient EMI was used to begin recording.

In order to obtain information about the plasma event directly the ICCD was utilized. A Stanford Computer Optics 4 Picos camera pictured in figure 3.20 was used to achieve these images. This camera is capable of a 200 picosecond shutter speed and gating timing as low as 200 ps. The jitter of the internal system is as low as 10ps. The internal timing control can delay the shutter speed within steps of 10 ps. In order to utilized these incredibly swift timing controls, the camera is triggered from the oscilloscope off of the rise in current during the plasma event. The intensity of the plasma event creates issues similar to the problems that occurred with the high speed camera. However, because the ICCD is imaging only during plasma event itself it is possible to adjust the

shutter speed and gain in order to not over expose the image. Unlike the high speed camera that takes many images of the same event, the ICCD is only capable of taking one or two well timed images of a single event. As a result, 150+ events are photographed with varying delays in the shutter timing. These images can then be tied together to show a representative video of the event. In addition to giving a general image of the plasma, the ICCD images can be utilized to extract intensity data from individual events.

3.4 Analytics

The primary data analysis tool used for both oscilloscope data and ICCD data was Matlab. Two scripts were made to meet the demands of this data. The first script accepted the voltage and current data from each run. An algorithm was created in order to identify the time and voltage of both the air spark discharge (V1) as well as the main spark discharge (V2). The algorithm identified the first rise in voltage (event start) then identified the peak over the next 100 ns which was defined as the air spark discharge, V1. In order to find the V2 discharge location the data is searched for peaks after the V1 event. It is verified that data on either side of the peak have a large slope (indicative of the breakdown). This point is marked as V2 and the voltage is recorded. V2 is then defined as time=0. From there the power and energy calculations are calculated and recorded.

The second script analyzed the ICCD data. The data was extracted and organized in such a way that the each pixel was represented as a node within an array with the dimensions 1360x1024. Each value within the matrix represents the intensity observed on a scale of 0 to 4096. A number (10+) of background images were created in order to quiet the inherent noise present within the ICCD output. The background values were averaged and the standard deviation was found. The amount 2 sigma for each node of the background images was then subtracted from the corresponding node of each data set. From there any negative values were set to zero and the remaining non-zero values were used to represent effects created by the plasma with a 98% confidence. A region of interest (ROI) was utilized in order to omit some of the reflections present outside of the discharge area. A circle was drawn around the point of highest intensity which was expected to be the center of the discharge. All values outside of the ROI were ignored in any calculations. In order to calculate the

Figure 3.12: Power Supply

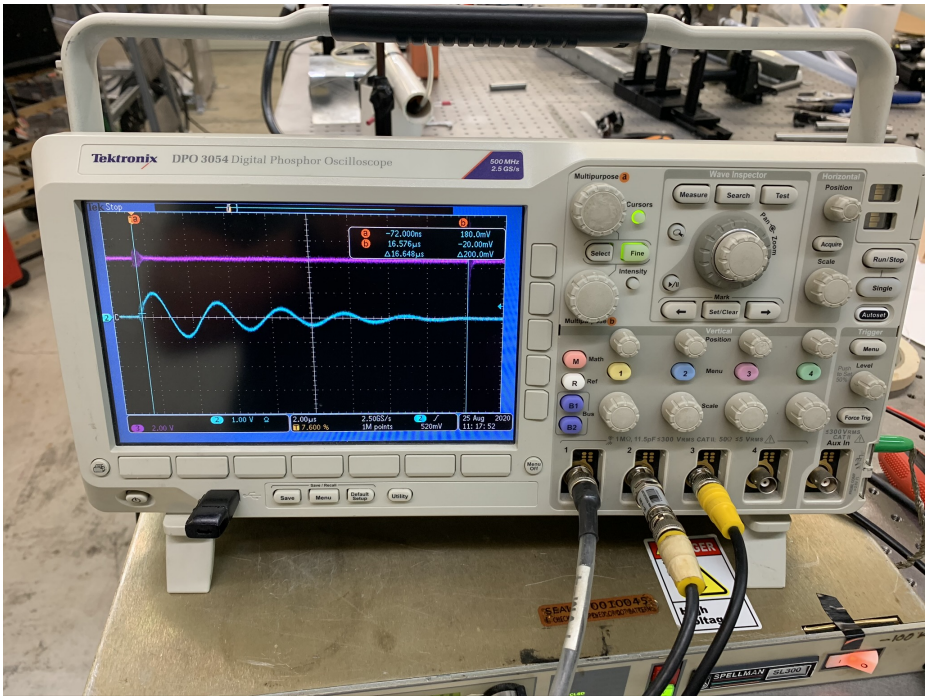

Figure 3.13: Oscilloscope

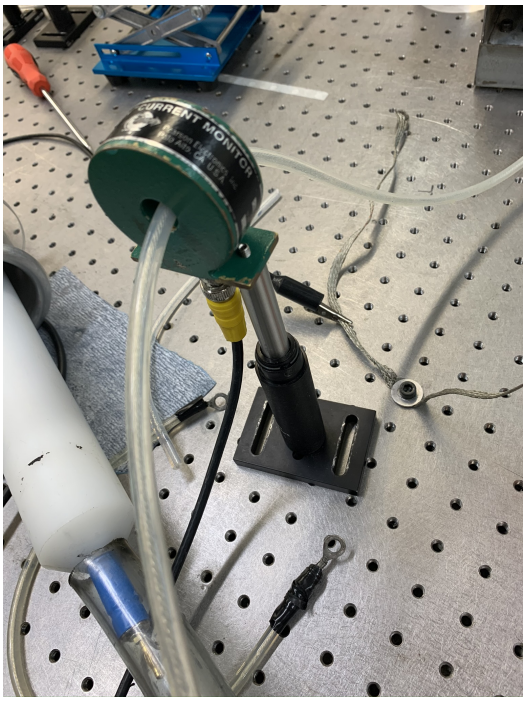

Figure 3.14: Current Probe

Figure 3.15: Voltage Probe

Figure 3.16: Orange Capacitor

Figure 3.17: White Capacitor

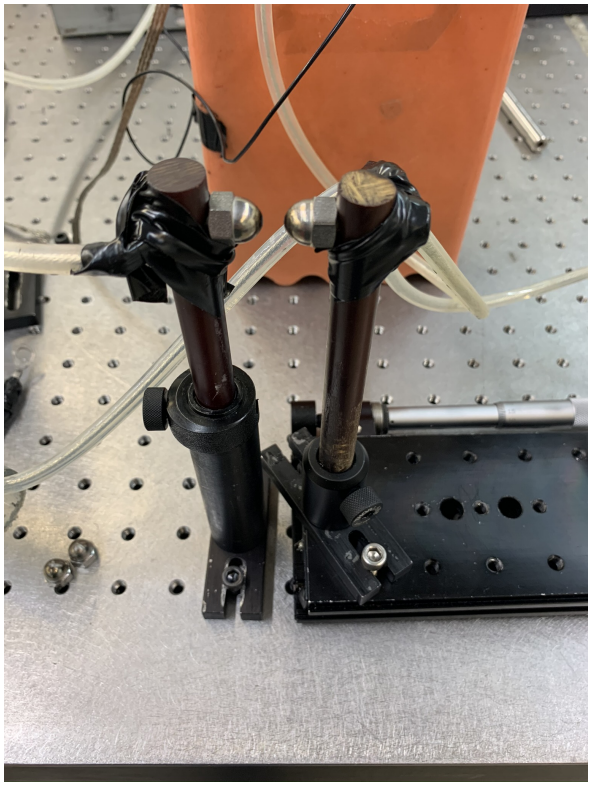

Figure 3.18: Air Gap Spark Switch

Figure 3.19: High Speed Camera

Figure 3.20: ICCD, Intensified Charged Coupled Device

Figure 3.21: Laser

intensity values the sum of all non-zero intensities was taken and the total represented the intensity of the discharges as a whole. The spot size was calculated by counting every non-zero element. This sum represents the footprint of the discharge and as such was used as the spot size value.

3.5 Experimental Procedures and Safety

Due to the inherent danger of these experiments several precautionary measures have been taken to ensure the safe operation of all the involved equipment. The primary dangers involved with these experiments are due to the high voltage/high current electricity from the power supply and capacitor as well as the dangers associated with highly pressurized chambers. In order to ensure safe operation of the electrical components standard operating procedures are followed. These procedures can be found in the list below. It is strongly encouraged that a lab mate double checks and verifies the integrity of any electrical setup before use.

1. Perform safety check and adorn PPE.
2. Check grounding rod circuit and ground all circuit elements (you never know how the system was left). Then ensure all electrical connections are correct and adequate. This includes voltage probe connections to the oscilloscope.
3. Ensure structural integrity of the pressure vessel by visual inspection.
4. Place the rock sample, on which the discharge will be performed, in the sample holder inside the pressure vessel.
5. Seal pressure vessel by appropriate method. Hand clamps for small vessel. Pneumatic ratchet for high pressure vessel.
6. Fill the pressure vessel chamber to the desired pressure.
7. Set temperature controller to the desired temperature and turn on vessel heaters.
8. Wait for appropriate conditions to be reached.
9. Set electrode spacing appropriate for desired breakdown voltage. Power on high voltage/high current power supply.
10. Set power supply voltage to the desired breakdown voltage using minimal current (less than

0.1 mA). Slowly adjust spark gap (air switch) distance until breakdown occurs. Lastly, power off the power supply.

11. Determine electrode spacing.
12. Perform the experiment. Send in the desired amount of plasma pulses onto the rock sample. Record oscilloscope data as necessary. Power high speed camera and capture image/videos of the spark on the rock surface simultaneously.
13. After the experiment is done turn off the power supply. by following the standard shutdown procedure.
14. Standard shut down procedure:
    (a) Return power supply voltage and current knobs to their zero positions
    (b) Shut off the power supply
    (c) Discharge all capacitors and circuit nodes which may have stray capacitance using grounding stick
    (d) Ground all capacitors
15. Emergency shut-down procedure
    (a) Power off power supply directly
    (b) Follow standard shut down procedure

The pressure vessel is capable of reaching pressures up to 680 atm under the correct conditions. It is very important to ensure that the correct steps and precautions are taken to ensure that the vessel does not fail and potentially injure someone. The pressure ratings for each component can be found in tables 3.2 and 3.3. The vessel is equipped with a safety rupture disk as a way of ensuring the point of failure. These disks are certified to rupture at a specific pressure and it is critical that the chosen disk has a failure pressure that is lower than the next weakest component. The pump within the system is capable of being actuated manually or pneumatically. The pneumatic mode is critical in order to bleed the pump of any gasses, but this mode must never be used to pressurize the system as it can reach critical pressures faster than the user may be able to react. The proper

operating procedures from set up to shut down are listed below.

1. Adjust the internal components of the vessel as desired.
2. Identify and note the safety rupture disk in use. Do not exceed said pressure.
3. Ensure any removed fittings other than the plug nearest the electrodes are taped with teflon and torqued sufficiently.
4. Orientate the vessel with the electrode section pointed upward.
5. Operate the hand pump via the pneumatic port until water is flowing and air is removed from the pump inlet. ENSURE THE VESSEL IS OPEN TO AVOID RAPID PRESSURIZATION.
6. Fill the remainder of the vessel with water. Ensure pressure relief valve is closed.
7. Teflon tape and loosely hand tighten the remaining plug.
8. Actuate the hand pump until the remaining air is bleed out of the system and water is leaking from the plug. Removing as much air as possible is critical to minimizing the potential energy within the system.
9. Secure the plug and perform a final visual inspection.
10. Orientate the vessel as desired and pressurize via manual actuation of the hand pump. Never pressurize the system pneumatically.
11. Perform a visual inspection for any water leaks. Gradual drop in pressure will also indicate a leak.
12. Perform experiments as desired.
13. Slowly open the pressure relief valve to bring internal pressure back to ambient.

In addition to the two primary safety risks, those who aided on these experiments were exposed to a number of general lab risks that require careful consideration. The plasma discharges can emit sounds similar to a small gunshot. It is important to equip hearing protection when necessary, especially in the event several discharges will occur. A number of oils and basic chemicals such as acetone are utilized on a as needed basis. Proper clothing and glove use will prevent any irritation or issues during their use. Lastly, a number of the items in use are of substantial weight. Closed toed footwear and care when handling such item will lessen the likelihood of accidents and injury.

4. BREAKDOWN THRESHOLDS IN HIGH PRESSURE WATER

4.1 Voltage and Timing

4.1.1 Process and Terminology

A parametric study was conducted that explores the feasibility of a plasma discharge with respect to various high pressures. The study was performed using the experimental setup discussed in chapter three. The exact electrode orientation is shown in figure 4.1. The electrode gap in this configuration is approximately 0.03 inches (0.75 mm). In addition to the core electrical system and pressure vessel, a current probe and a high voltage probe were used for diagnostics. The voltage probe measured the voltage entering the pressure vessel and the current probe measured the current along the same wire between the spark switch and the main plasma discharge. Through these diagnostics it is possible to discern whether a plasma event has occurred. Furthermore, the plasma power consumption, voltage needs, and some efficiencies can be identified or calculated. Figure 3.3 shows the exact layout and instruments that were used for this experiment (the laser source and high speed camera were not used).

During the experiments the data from the oscilloscope was saved and later processed in Matlab. A Matlab output plot from a single successful discharge can be seen in figure 4.2. Two separate events can be clearly identified within this experiment. First is the spark switch discharge referred to as V1. This is shown through the sharp increase in voltage accompanied by current oscillations under 100 amps. The settled voltage value immediately after the peak will be used for calculations as it better represents the voltage within the system. At this point a channel of plasma has closed the circuit between the capacitor and the first electrode of the pressurized system allowing electricity to flow into the test chamber. Once this occurs one of two events will happen. The preferred event is a full discharge that results in a second voltage spike and the release of a large current output on the scale of hundreds to thousands of amps. In the event of a successful discharge this moment will define time = 0. This event will be referred to as V2. In the case that this occurs, a second plasma

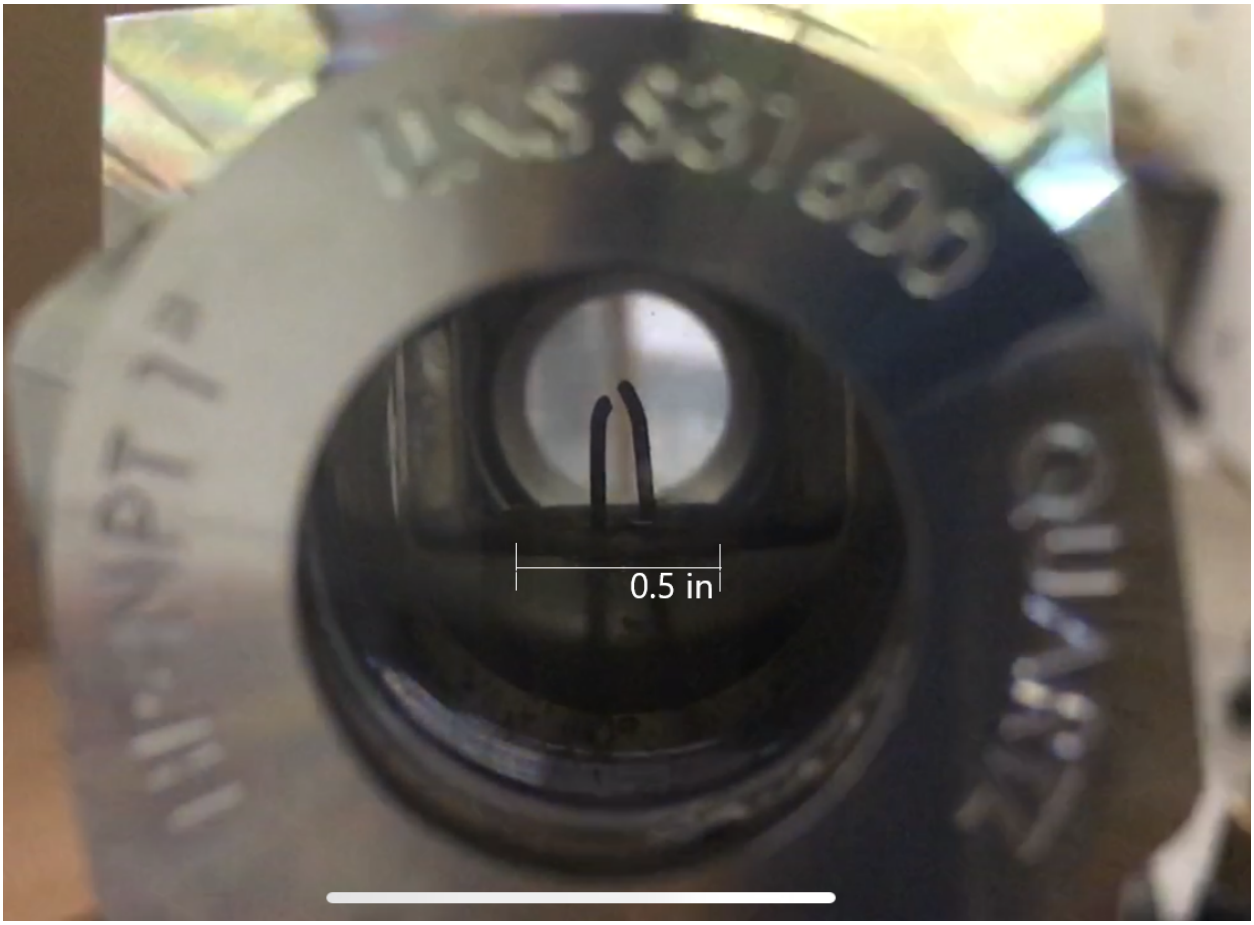

Figure 4.1: Electrode Orientation

channel has formed between the two electrodes within the test chamber. This plasma creates a conductive path for stored electricity to travel from the capacitor to ground through the second electrode. This can be seen from the sudden drop in voltage as energy has a path out of the system. The ending sinusoidal waves are an artifact of the plasma settling and ringing within the system after both events have occurred.

The second potential outcome is an incomplete discharge. Figure 4.3 shows the Matlab output of oscilloscope data in such an event. This event begins exactly the same as a complete discharge where the spark switch triggers creating a spike in voltage. However in this case a secondary discharge never occurs, and therefore time = 0 is defined as the discharge at V1. The voltage will continue to bleed off until it returns to zero. Being the unfavorable outcome, this study aims to

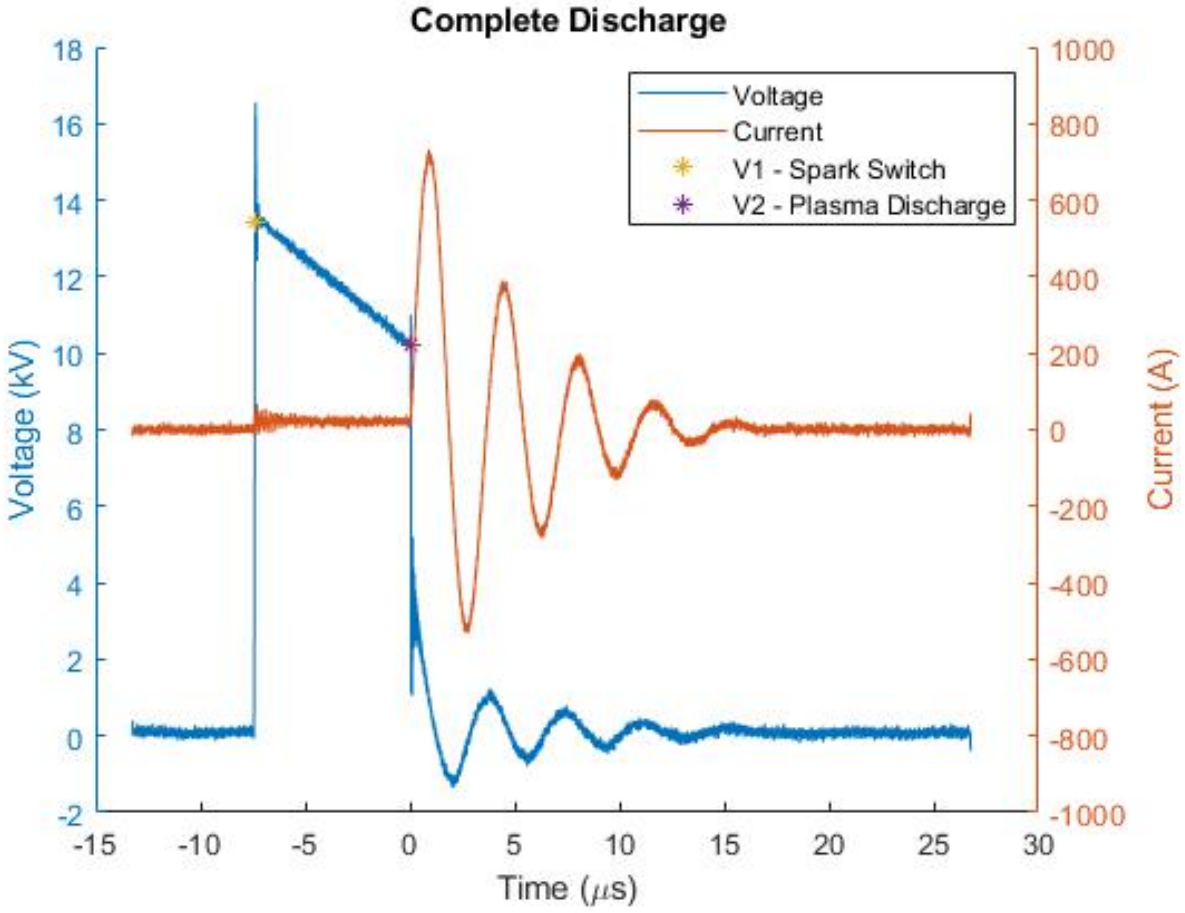

Figure 4.2: Oscilloscope Data - Complete Discharge

understand the driving differences between an incomplete discharge and a complete discharge.

The oscilloscope data will clearly describe whether the discharge event was complete or not. However, there are additional indicators that make the outcome obvious. The corresponding visual and audio outputs of the discharge provide enough information to make the determination. A full discharge produces a much brighter light and stronger sound than its incomplete counterpart. In order to obtain a full understanding the electrical characteristics as well as the light output have been investigated.

Figures 4.2 and 4.3 highlight many important facets that are discussed in this section. As noted above, the two marked discharge points and their relative voltage are important factors. As pressure is a key factor that may affect downhole plasma, knowing what voltage it will take to make

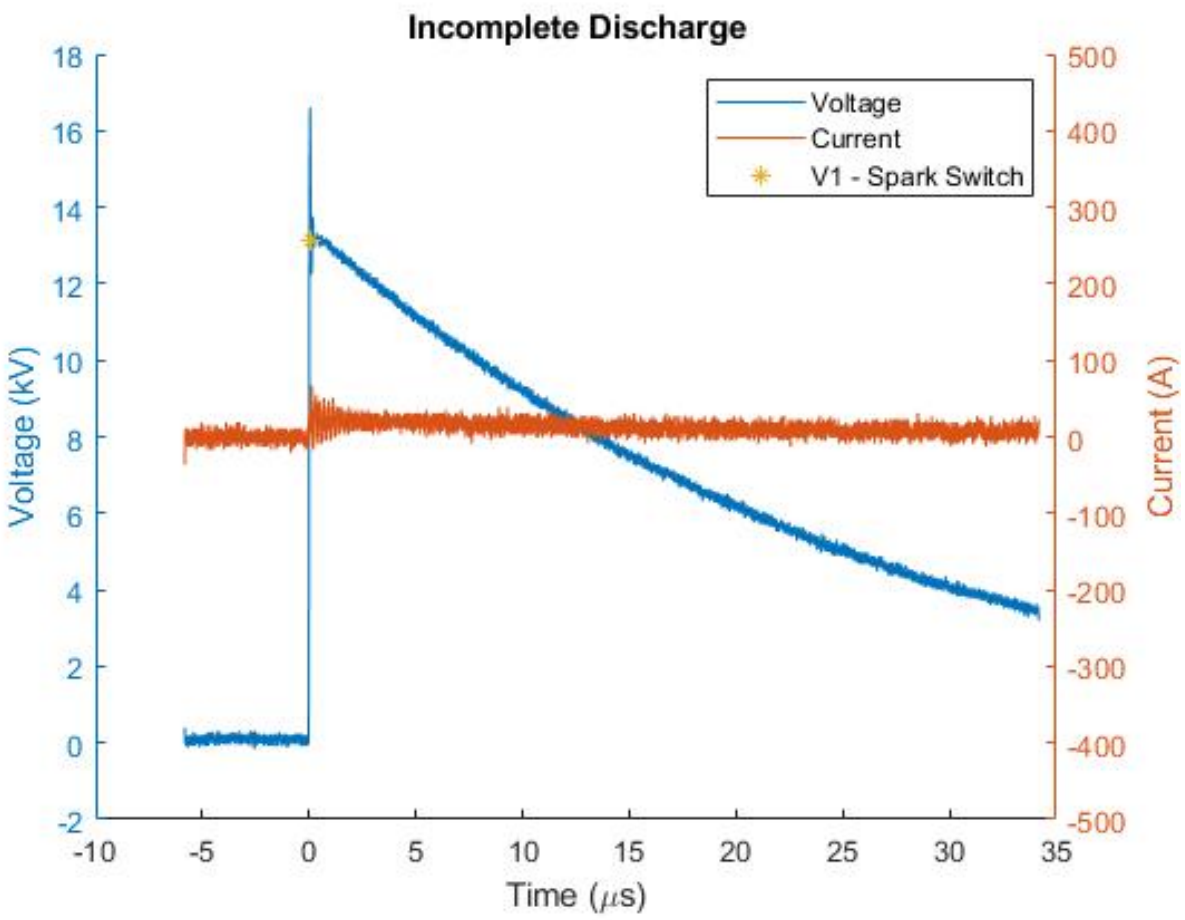

Figure 4.3: Oscilloscope Data - Incomplete Discharge

a complete discharge is important. Secondly, there is a voltage loss between the two discharges. Future sections will refer to this decrease as *voltage drop*. An incomplete discharge is dominated by this loss as it leads the voltage all the way to zero. This loss of voltage is an inefficiency within the system that opens opportunity to optimizations. Next is the amount of time between the first and second discharge. The later sections will refer to this as the *breakdown lag*. A different approach to optimizing the lost voltage is to minimize the time available for voltage to bleed away. Lastly, understanding the variation of the current magnitude and how to maximize it will allow for more intense discharges. The remainder of this section focuses on exploring the affect that pressure has on these listed variables.

4.1.2 Voltage and Current

As the ambient pressure is increased the system events before V2 tend to be fairly variable. However, the behavior of the voltage and current after the initiation of the V2 breakdown seem to be surprisingly consistent regardless of pressure. Figures 4.4 and 4.5 show that the output electrical frequency remains constant regardless of the ambient pressures. The period of both traces seem to align nearly perfectly throughout the duration of the event. The magnitudes of the voltage and current traces will to vary due to different input energies and inefficiencies from discharge to discharge. The resulting lifetimes seems to be a function of how quickly the event damps and its initial magnitude.

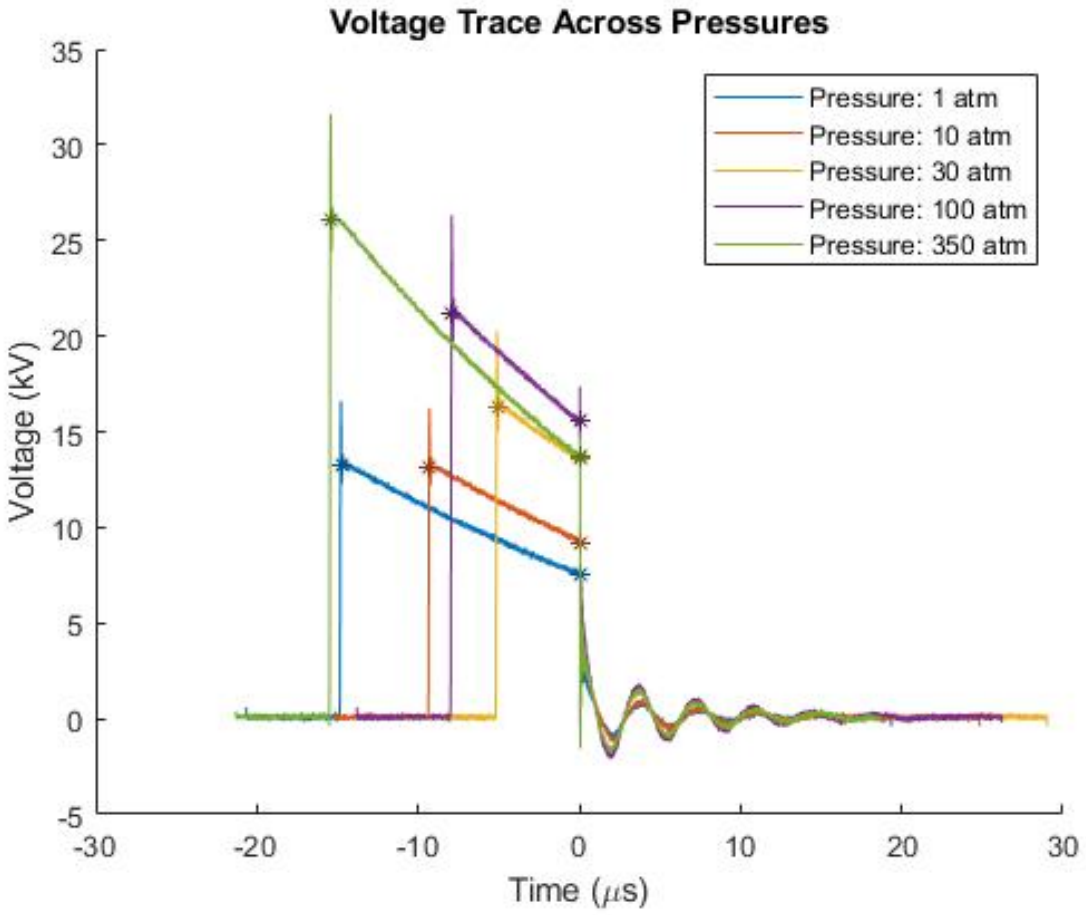

Figure 4.4: Voltage Trace Across Pressures

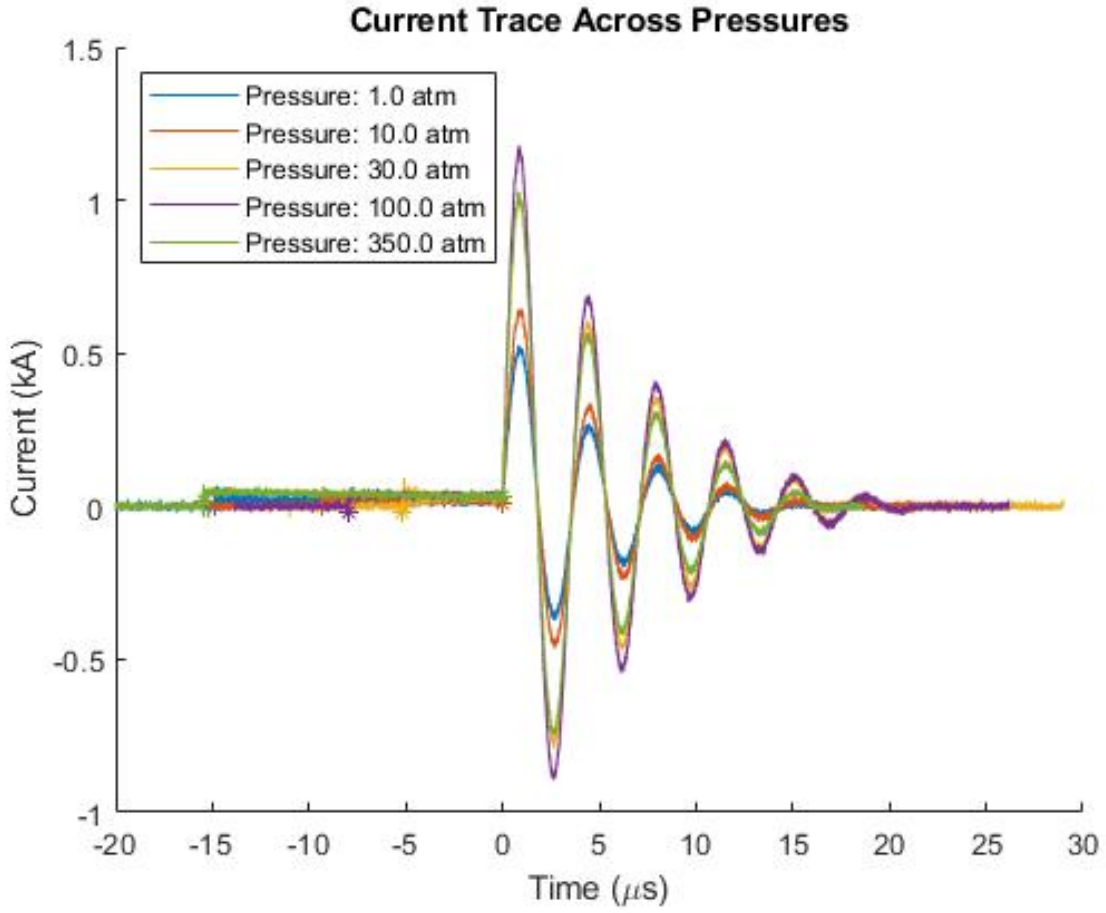

Figure 4.5: Current Trace Across Pressures

4.1.3 Voltage Drop

A key inefficiency within the observed system is the drop in voltage between the spark switch, V1, and the primary discharge, V2. Figure 4.6 depicts the voltage during the first breakdown at the spark switch. Instances of both the complete discharges and the incomplete discharges are shown. There is a noticeable trend of a higher required voltage as pressure is increased. Figure 4.7 shows the voltage of the system at the moment when the fluid discharge occurs. While an upward trend is still noticeable, it is not nearly as distinct or sharp. Furthermore, the magnitude of the voltage shown is lower than the earlier spark switch. This delta highlights the loss of energy present between the two events. Figure 4.8 overlays figures 4.6 and 4.7. The inefficiency discussed

can be clearly seen in this graph along with some potential pressure effects.

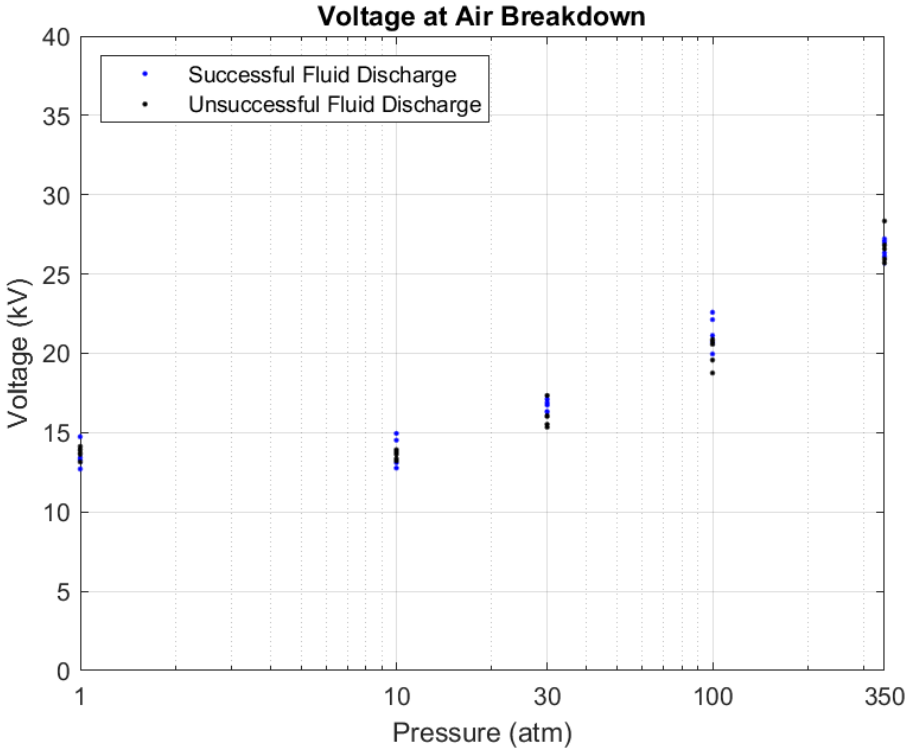

Figure 4.6: Voltage at Spark Switch

In order to better understand the loss of energy present in the time between the two discharges a plot of the average voltage delta vs pressure was created. Figure 4.9 pieces together the above data regarding this loss and offers a general feel for the average losses with respect to pressure. It is clear that the loss increases with pressure. This may have to do with the increased difficulty to breakdown or an increase in the lag time. The following section discusses the breakdown lag variable and it's affect on this inefficiency.

4.1.4 Breakdown Lag

In the event of a complete breakdown the time in between the spark switch discharge and the vessel discharge is quite variable (5 μs to 30 μs). Figure 4.2 highlights this pause between

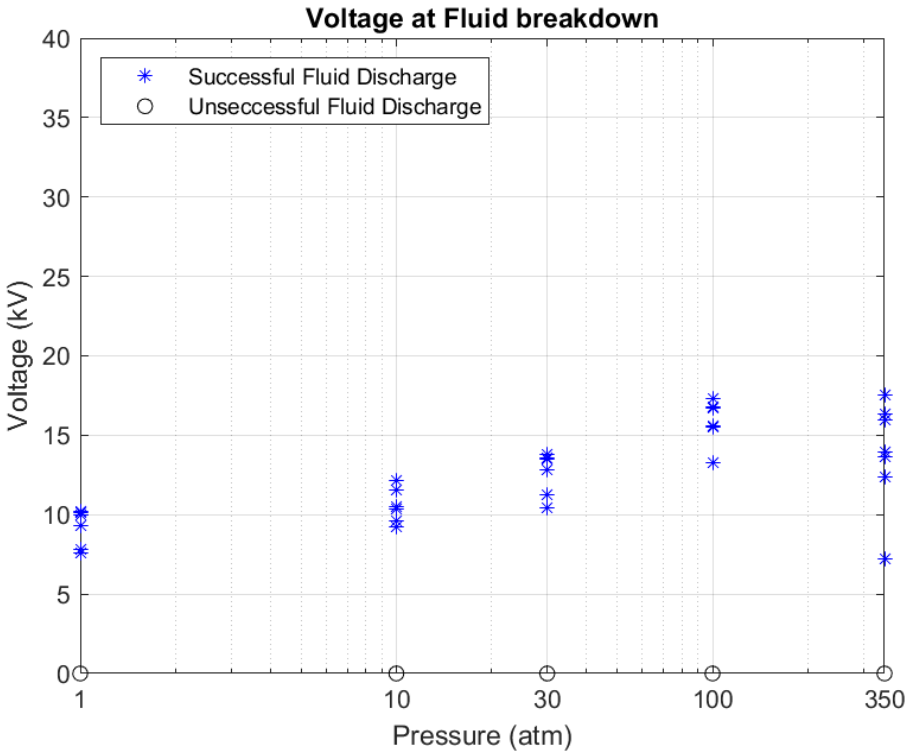

Figure 4.7: Voltage at Primary Breakdown

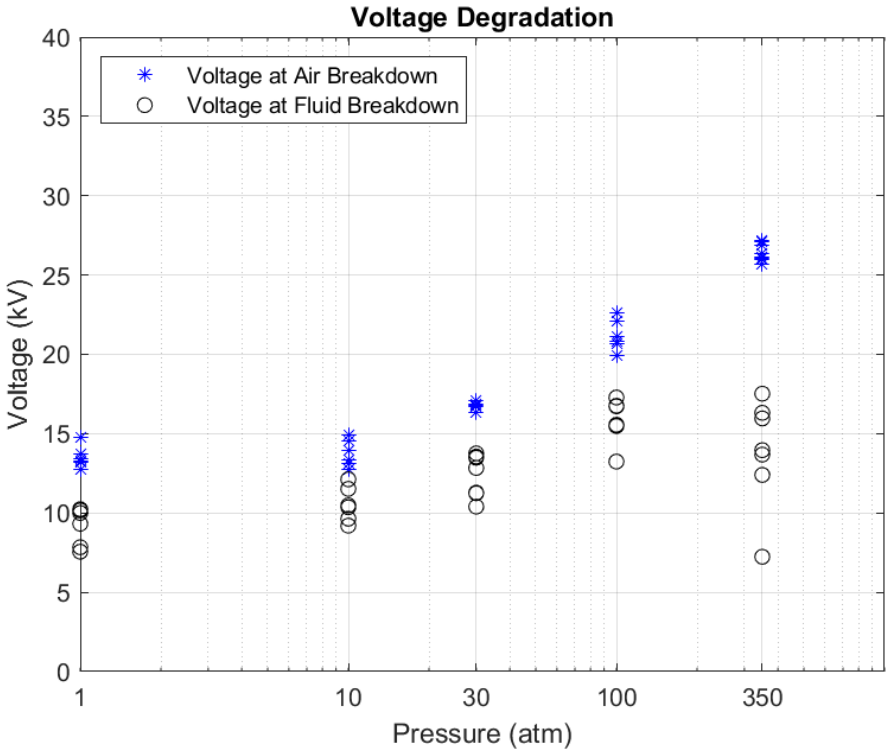

Figure 4.8: Voltage During Successful Discharge

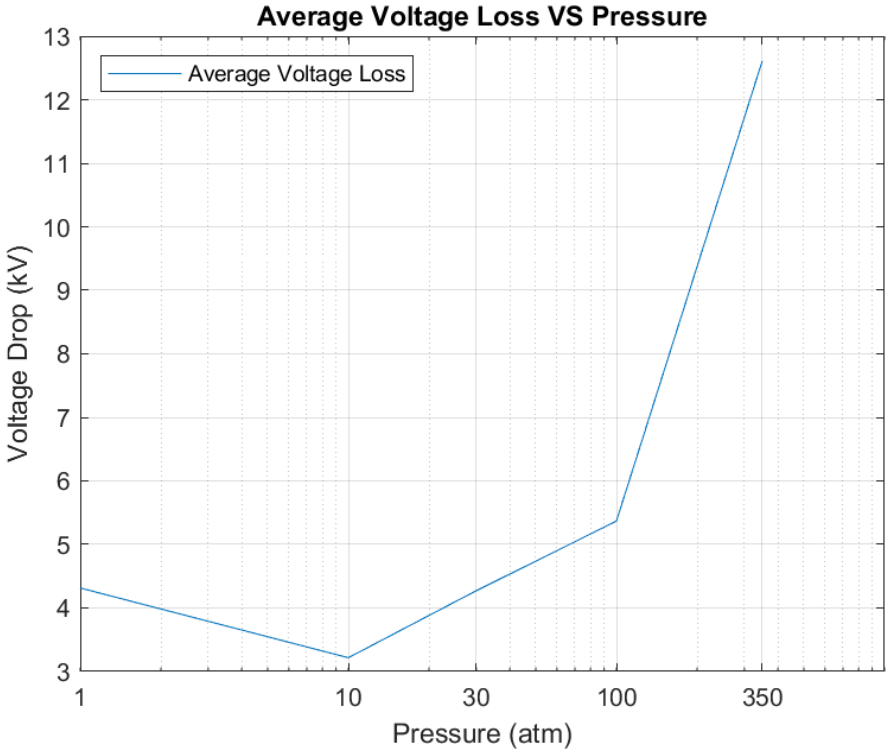

Figure 4.9: Voltage Loss Between Switch and Primary Breakdown

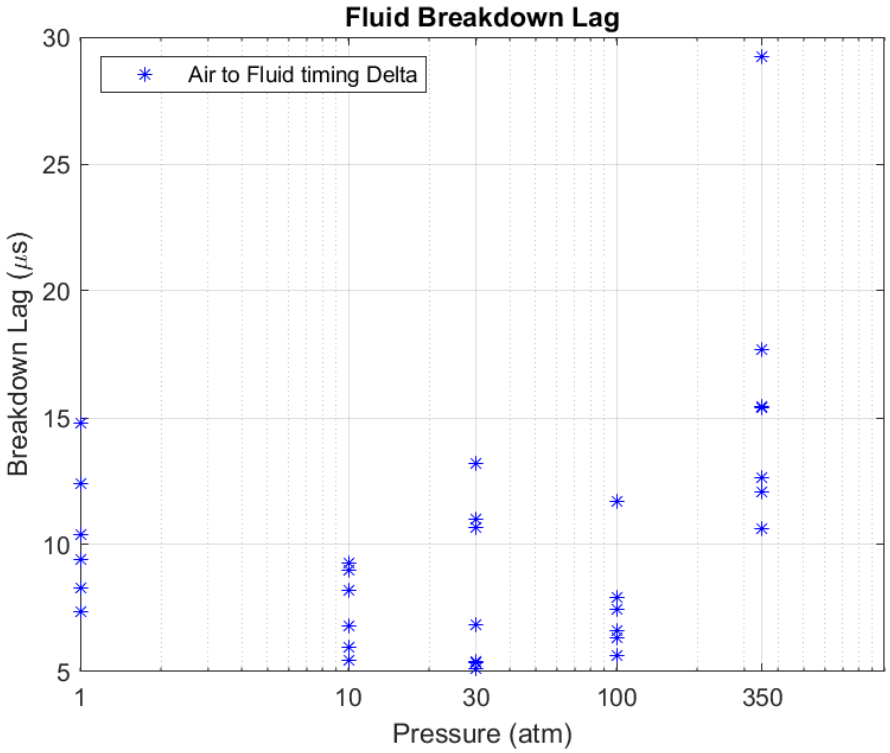

Figure 4.10: Breakdown Lag

breakdowns. The issue concerning this lag involves the inefficiency discussed above. In the event of an incomplete discharge, as can be seen in figure 4.3, the lag time is infinite and a full discharge is never reached.

The spread of breakdown lag times can be seen in figure 4.10. It is clear to see that the variability ranges over many μs and seems to be unaffected by pressure. the discharges at 350 atm are notably slower, which encourages a positive correlation, however the breakdowns at 100 atm seem to remain quite similar to the results at 10 and 30 atm. Overall, this figure does not encourage any strong conclusions directly between the lag time and pressure. Ultimately this lag is not a concern, but rather it's effect on the voltage degradation is the important consideration.

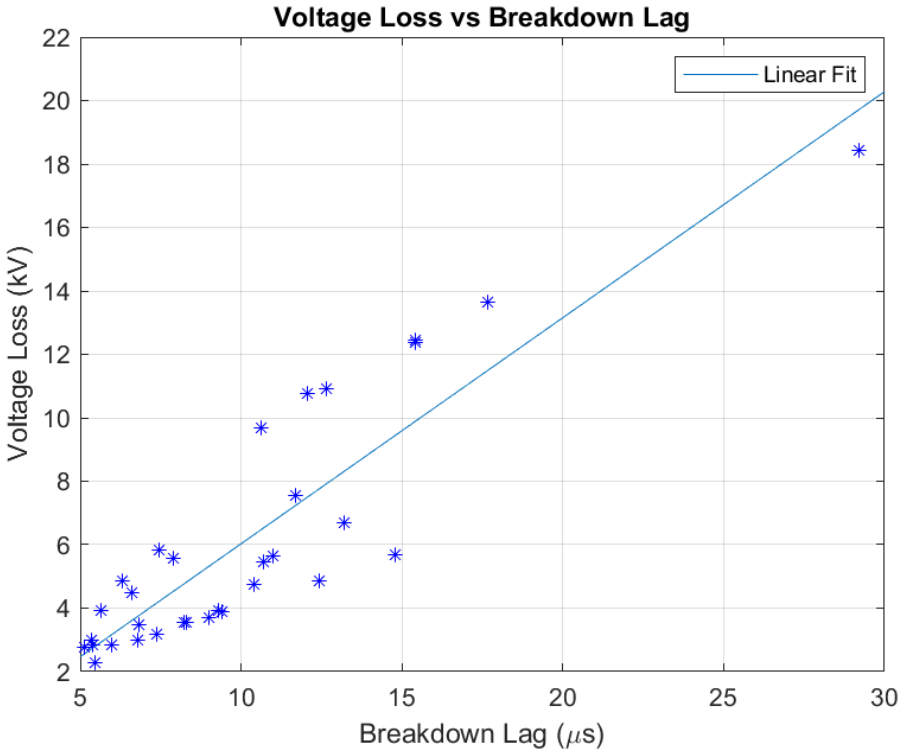

Figure 4.11: Breakdown Loss vs Lag

The relationship between voltage loss and voltage lag is show on figure 4.11. A fit line is shown that clearly demonstrates a positive correlation between the two variables. That is to say,

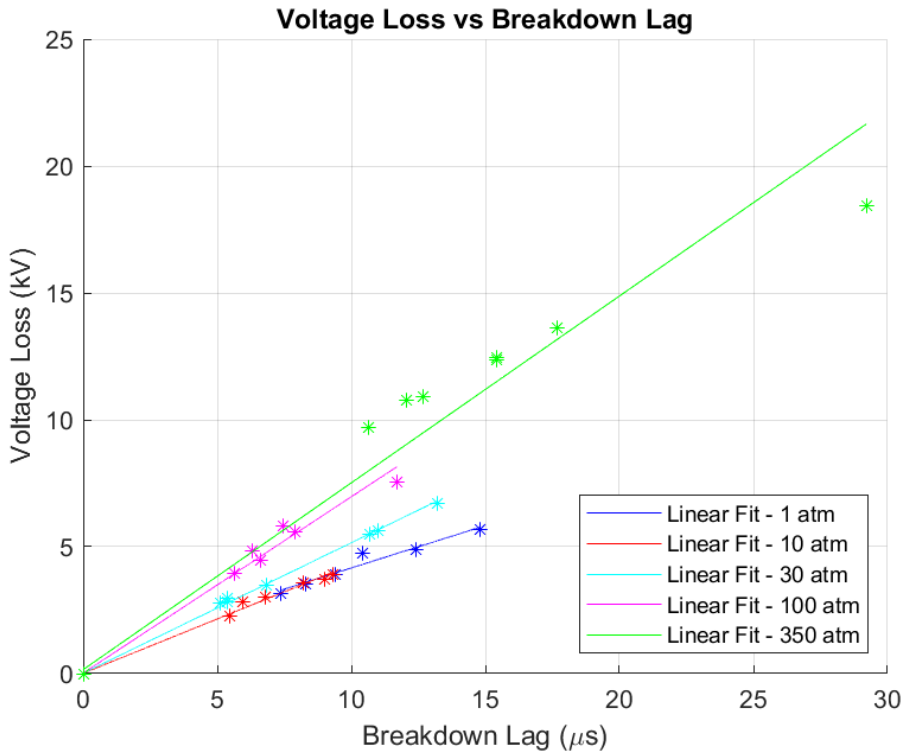

Figure 4.12: Breakdown Loss vs Lag

as the breakdown lag increases, the lost voltage is likely to increase as well. This graph highlights the importance to minimize the breakdown lag as a means of optimizing system inefficiencies. Further information can be extracted from this plot by separating the data according to pressure and overlaying the results. Figure 4.12 offers an interesting perspective of the data shown in 4.11. Here it is clear to see that voltage loss increases with pressure. The breakdown lag does not seem to increase until the pressure rises well above the critical pressure of water (218 atm).

A different way of displaying the data shown in figure 4.12 can be seen in figure 4.13 where the ratio of voltage to lag is displayed with respect to each pressure. Displaying the data in this way makes it more clear to see the cost of a longer lag time. The higher the loss/lag ratio is, the more voltage will be lost per unit time. This relationship is then plotted vs pressure which yields interesting results. Increased pressures yield an increased ratio.

In order to better understand the inefficiencies present between V1 and V2 the resistance of the

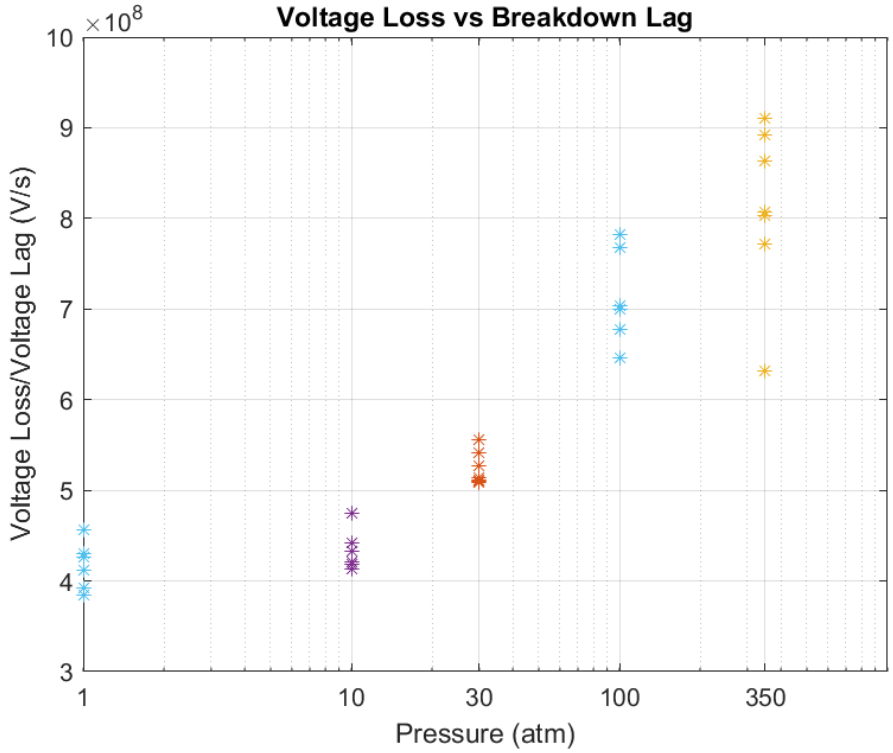

Figure 4.13: Breakdown Loss vs Lag

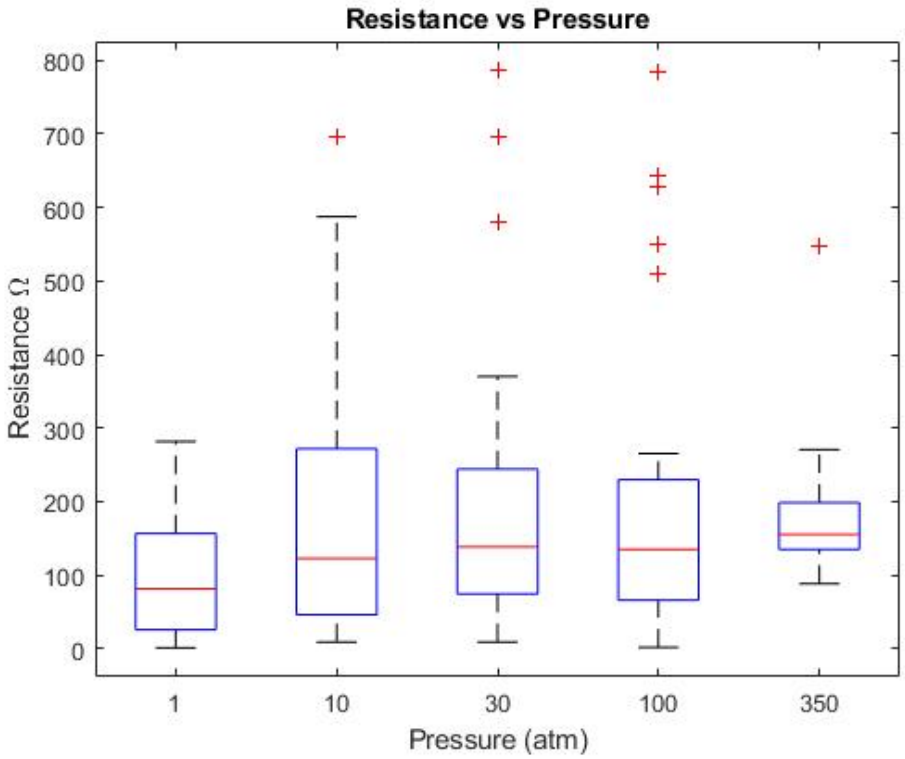

Figure 4.14: Resistance vs Pressure

system was calculated by dividing voltage with current. This value is then averaged over the time between V1 and V2. The results from this calculation can be found in figure 4.14. From this data it is evident that the resistance remains mostly consistent throughout the pressure changes. This highlights the importance of the lag time over pressure related conductivity changes with respect to the voltage drop.

4.2 Energy Analysis

The energy within the system can be derived from the voltage and current traces by following equation 4.1. The resultant energy trace can be found in figure 4.15. The energy traces can be broken into four sections: pre-breakdown, V1 breakdown, V2 breakdown and final energy. The pre-breakdown region the flat area before time zero where no activity happens. Once V1 breakdown occurs the system will consume energy in a logarithmic trend. This is due to energy losses through heating effects and other inefficiencies. At the moment that V2 begins the resistance within the system drops due to the plasma channel that offers a path toward ground. This causes a surge of current that will spike the energy upward. The energy then oscillates briefly before it settles into the final energy portion of the curve. This concluding energy value represents the energy used by the system.

$$E = \int_0^t V * I dt \tag{4.1}$$

The connection of these four sections and their complementing voltage traces is easily seen in figure 4.16. Just as in early voltage traces, the first '*' marking indicates V1 and the second V2. All of the curves are centered around V2 (t=0) which makes the consistent discontinuity of the energy traces clear. Furthermore, it can be seen that V1 marks the start of the energy bleed off. Due to the sustained high voltages the loss of energy before V2 can become quite substantial. This helps to highlight the importance of minimizing both the voltage loss and the lag time discussed above.

The energy that each discharge creates will vary slightly from event to event. Figure 4.17

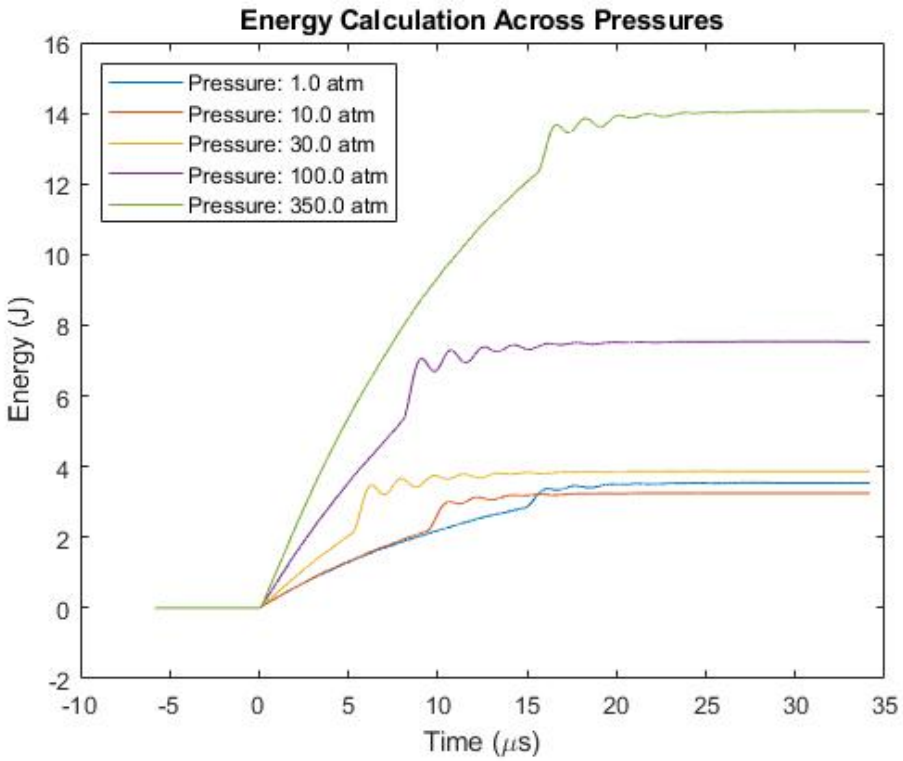

Figure 4.15: Sample Energy Traces

shows the statistics of the discharges at each pressure. This graph shows that higher pressure discharges will increase outputted energy. While this is true, energy is coupled with voltage and it was shown above the the minimum breakdown voltage increases as the pressure increases. Figure 4.18 takes this data a step further and separates the energy into energy used before and after V2. It is clearly seen here that higher pressure don't necessarily result in a higher energy discharge, but rather significantly higher inefficiencies. At each pressure's respective breakdown voltage, the breakdown energy (after V2) remains fairly constant.

As noted above, higher pressures require higher voltages for breakdown, and it therefore makes sense that they would have higher energies. Figure 4.17 shows a scatter plot of discharge voltages at V1 and V2 with respect to the total energy from the discharge event. A very obvious trend emerges that correlates an increase of voltage with an increase in energy. A number of data points can be found at the bottom of the curve. These points represent incomplete discharges (V2 =

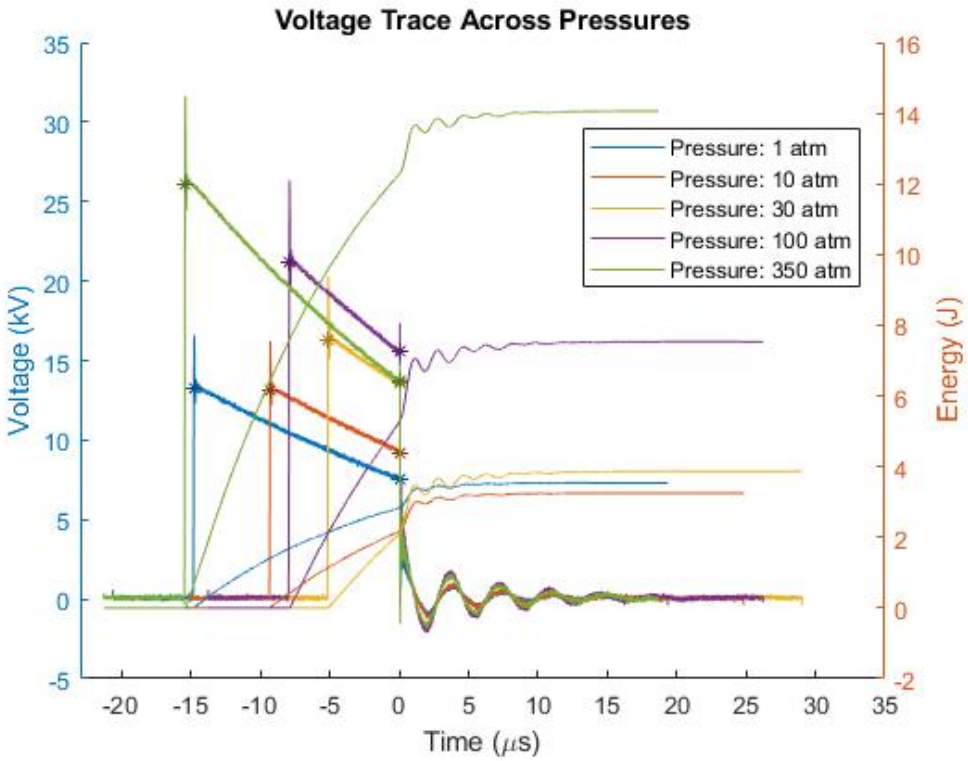

Figure 4.16: Sample Voltage and Energy

0). These values have an associated energy value because the system still bleeds all of its energy through heating and inefficiencies despite lacking a full breakdown.

The system energy is important in terms of overall requirements and design, but the energy succeeding the V2 discharge is the energy that is imparted upon the rock substrate. As such, it makes sense to maximize this portion of the energy curve. Figure 4.20 shows a similar scatter plot to the one above but instead of total energy this graph only shows the energy used after V2. A general positive correlation can be found within this part of the data as well. It is important to note that increasing V1 does seem to correspond to an increase in V2, that is to say the pressurized breakdown voltage can be manipulated by changing V1 despite the pressure changes. The data points on the left portion of the graph represent the incomplete discharges. In this case an incomplete discharge yields zero discharge energy, a V2 voltage of zero, and a V1 voltage that bleed to zero through losses.

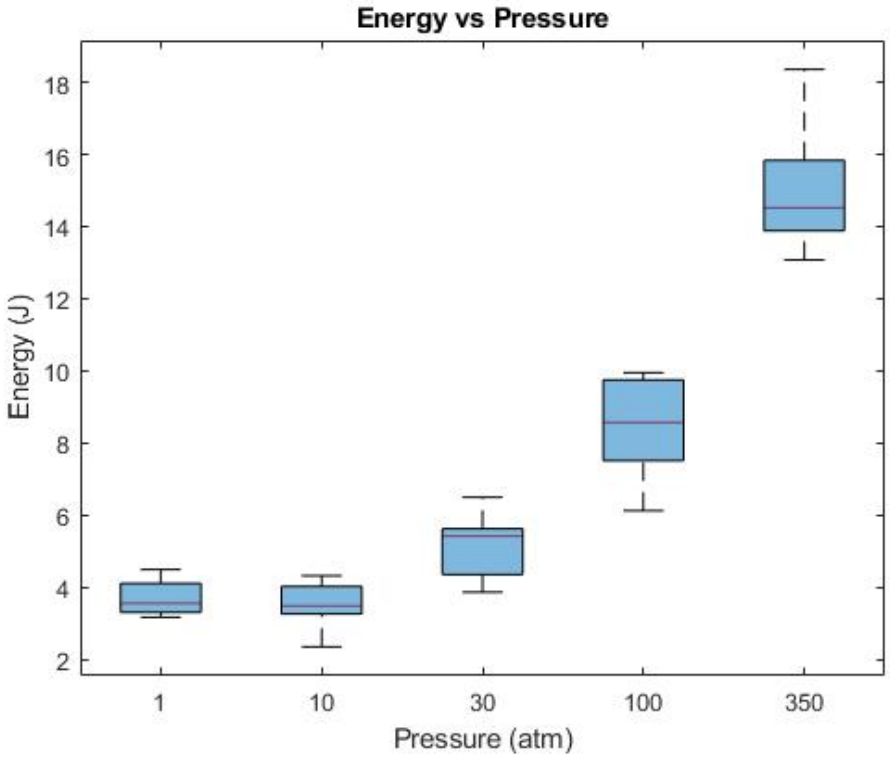

Figure 4.17: Total Energy vs Pressure

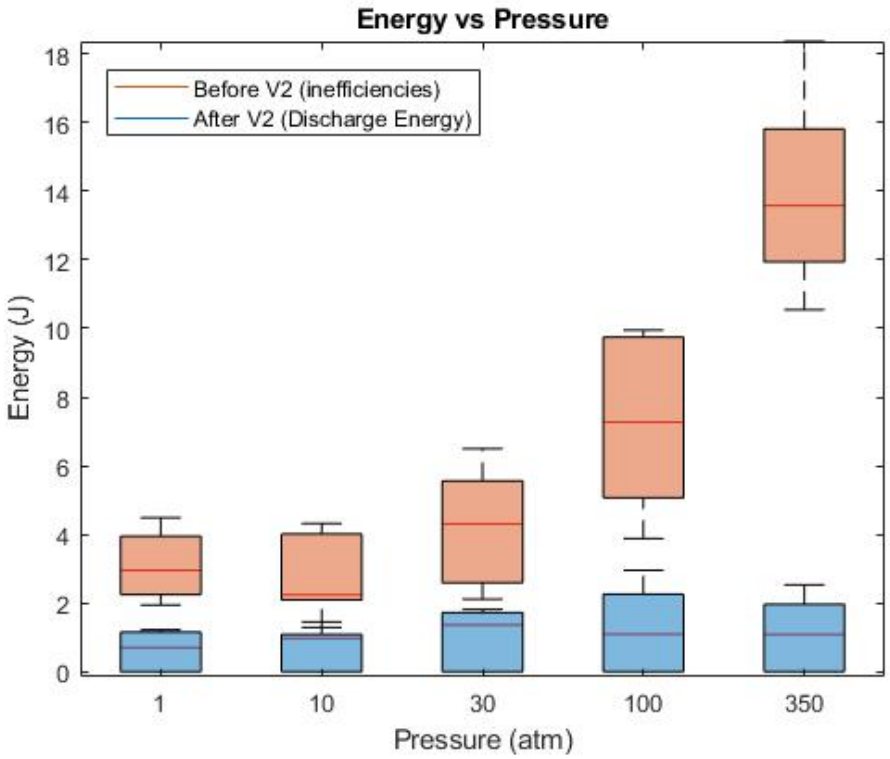

Figure 4.18: Energy vs Pressure, Before and After Plasma Breakdown

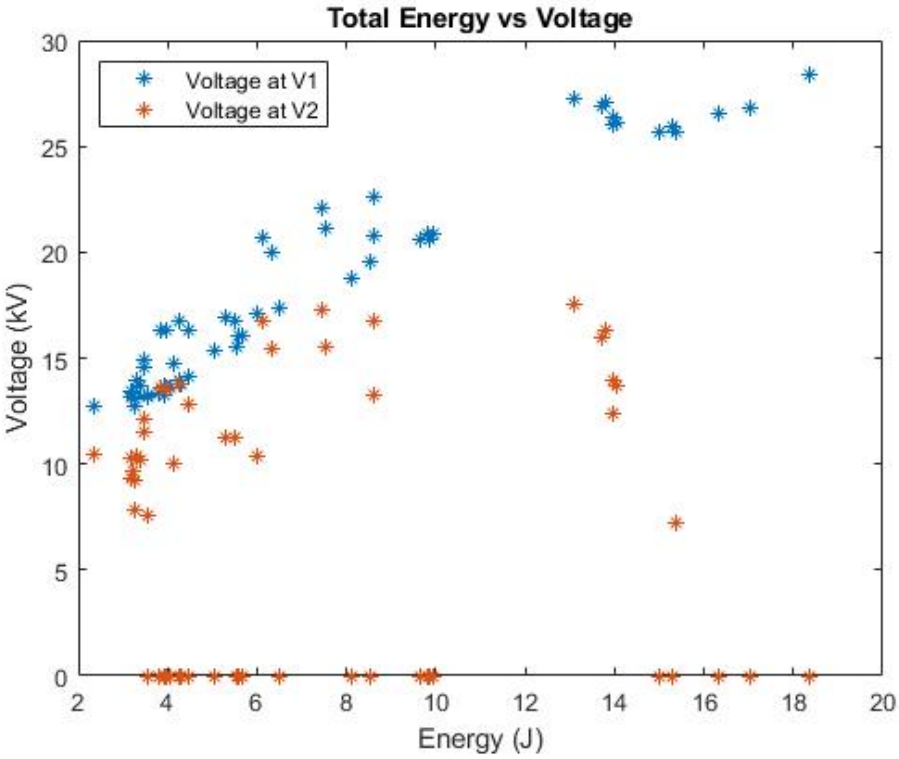

Figure 4.19: Total Energy vs Voltage, V1 & V2

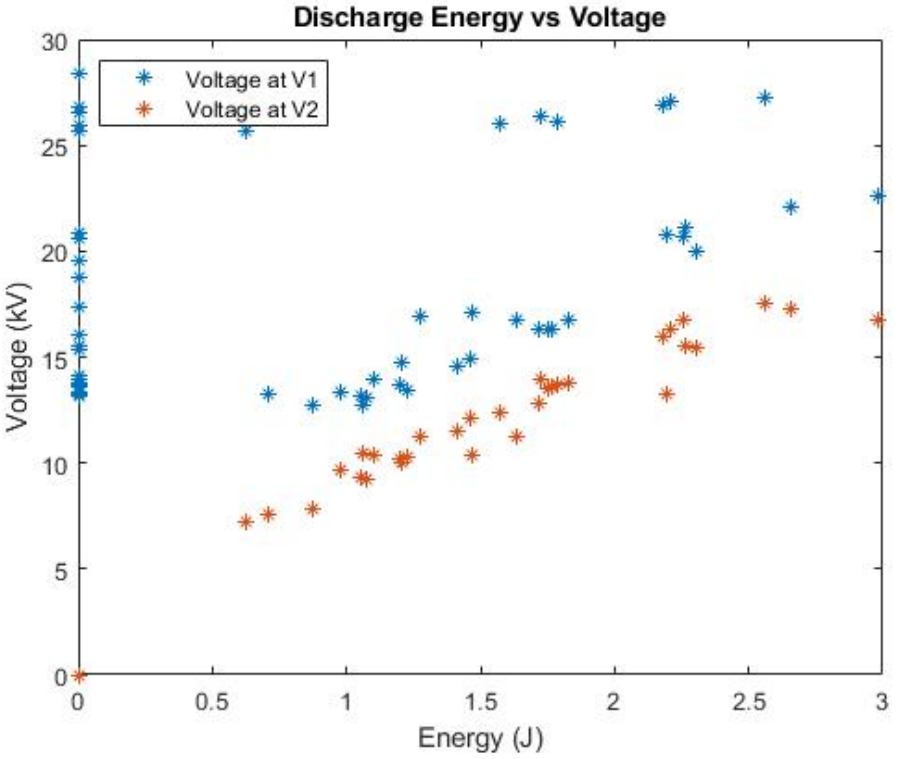

Figure 4.20: Discharge Energy vs Voltage, V1 & V2

4.3 Pressure Effects Near Minimum Breakdown Voltage

The whole purpose of this experiment was to gain an understanding of the event behavior near the minimum breakdown voltage. Ensuring that breakdown occurs is a key requirement and also a primary liability. Understanding the minimum allowed input voltage will highlight the design thresholds regarding voltage. Figure 4.21 clearly highlights the success region (colored in green), the transition region (colored in yellow), and the failure region (colored in red). It is important to note that this graph is dependent upon the electrode configuration and will vary with different electrode gaps. Within the conditions explored (pressures up to 350 atm), voltages at or exceeding 35 kV seems to be a safe baseline design threshold.

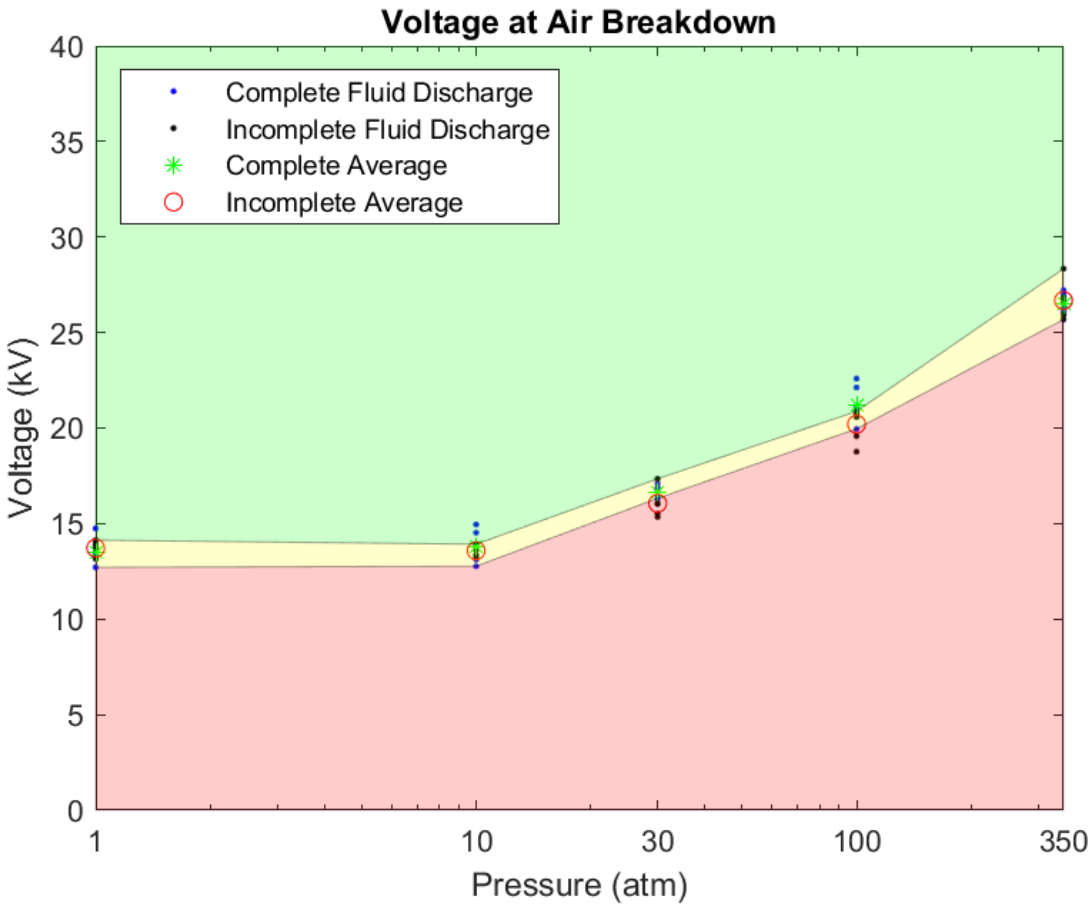

Figure 4.21: Pressure Analysis

The primary pressurized spark gap (V2) associated with these discharges is roughly 0.03 inches (0.75 mm). A clear trend of requiring high voltage as pressure increases can be identified. It is worth noting at lower pressures (1 atm - 30 atm) there is very little change in the required voltage. It isn't until the ambient pressure extends past 50 times atmospheric pressure that a more significant voltage is required. The trend of increasing voltage is proportional to the increasing pressure. This ratio be written as approximately $V \sim Pressure^{0.18}$. The yellow transition band of 2kV-4kV remains fairly consistent throughout the pressure ranges suggesting that this uncertainty region is unaffected by the pressure difference.

5. EFFICIENCY IMPROVEMENTS: OVER-VOLTAGE AND GAP MINIMIZATION

The previous section discusses the importance of minimizing the lag between V1 and V2 in order to focus the discharge energy into the plasma event as opposed to the inefficiencies present before V2. A new experiment was conducted with the same equipment, however the electrode gap was minimized and voltage ranges outside of the minimum breakdown voltage were explored. The gap used for this experiment can be seen in figure 5.1. The two electrodes are as close as possible while ensuring that they were not in contact. The gap distance is roughly 0.01 inches (0.25 mm). The smaller electrode gap has an effect on the voltage required to break down. This then enables the ability to reach voltages well above the minimum voltage for breakdown.

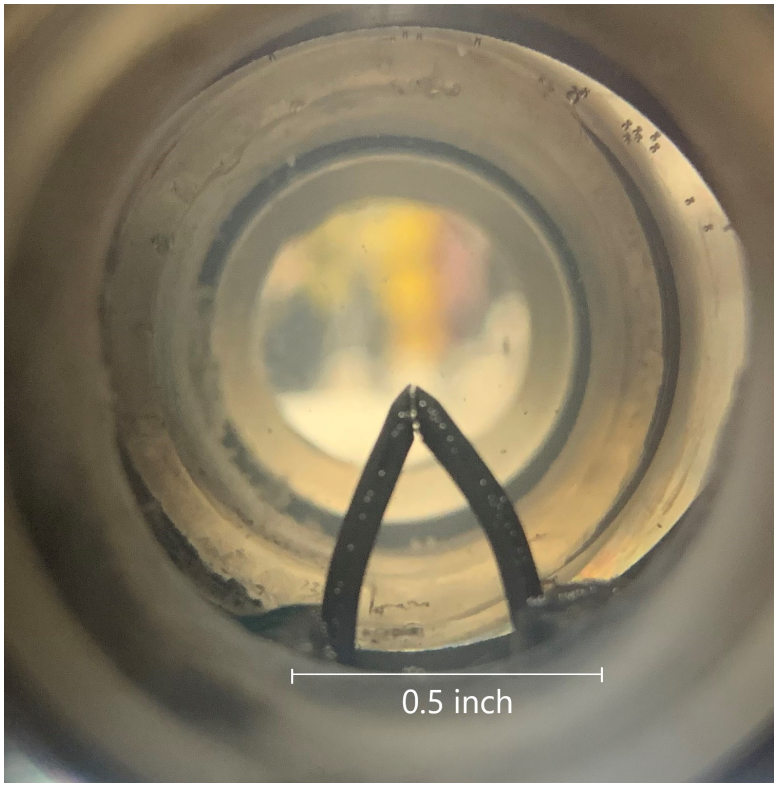

Figure 5.1: Electrode Configuration, Minimized Gap

5.1 Zero Lag Scenario

This experiment revealed a condition that was outside the scope of the experiment above. By providing a voltage that is much greater than the required minimum voltage it is possible to "over-voltage" the V2 plasma discharge. Under these conditions it is possible to minimize the time gap between V1 and V2 to the point where they are nearly indistinguishable. Figure 5.2 shows the voltage and current traces of such an event. On the microsecond time scale it seems that the event begins with a single peak and continues as it would normally after V2. Figure 5.3 takes a closer look at the same data reveling that the voltage spikes from 0 to roughly 10 kV where it bounces for the next 100 ns until the sharp V2 discharge event occurs. The absence of several microseconds of lag and inefficiency opens a possible step change to the plasma discharge efficiency and power delivery.

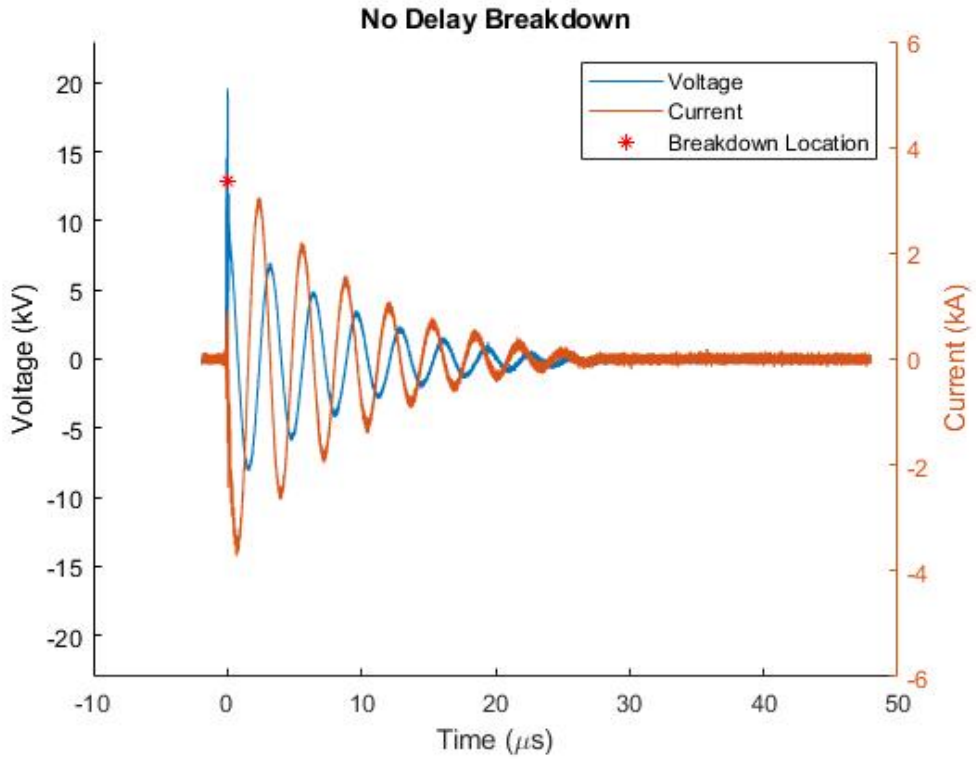

Figure 5.2: Event With No Lag Between V1 and V2

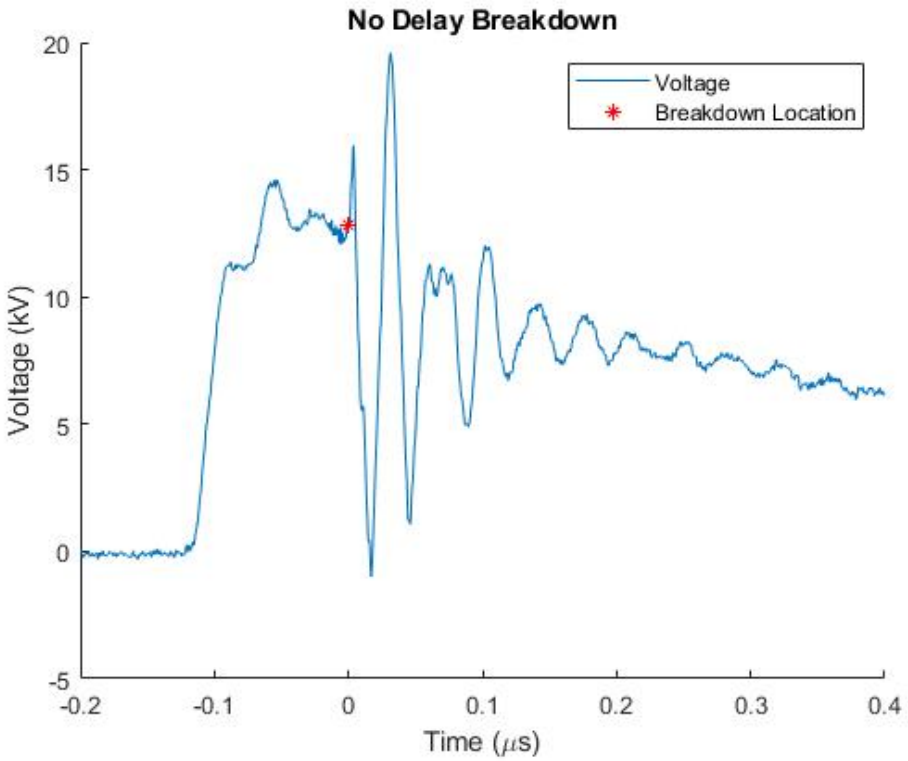

Figure 5.3: Event With No Lag Between V1 and V2, Zoomed

5.2 Gap Effects

The reduction of the space between the electrodes allows for lower breakdown voltages. In air the breakdown voltage can be calculated using Paschen's law. The equation to generate this curve can be found in equation 5.1. V_B is the breakdown voltage, p is the ambient pressure, d is the gap distance, γ_{se} is the secondary-electron-emission coefficient, A and B are constants. This equation is designed to the breakdown voltage of gasses within low pressures. It is reasonable that the form of this equation could shed some insight on the breakdown voltages of the conditions studied here. The main take away is that a decrease in gap distance, d will cause V_B to decrease.

$$V_B = \frac{Bpd}{ln(Apd) - ln(ln(1 + \frac{1}{\gamma_{se}}))} \tag{5.1}$$

As estimated above, a decrease in gap distance does indeed correspond to a decrease in the required voltage for breakdown. Figure 5.4 illustrates the required breakdown voltage across the experimental pressures. The same illustration for the larger gap was explored in Chapter 5 was shown in figure 4.21. This new figure has less resolution near the the breakdown region, but it clearly shows that the voltage required for breakdown is 5-10 kV lower than the larger gap explored in chapter 4.

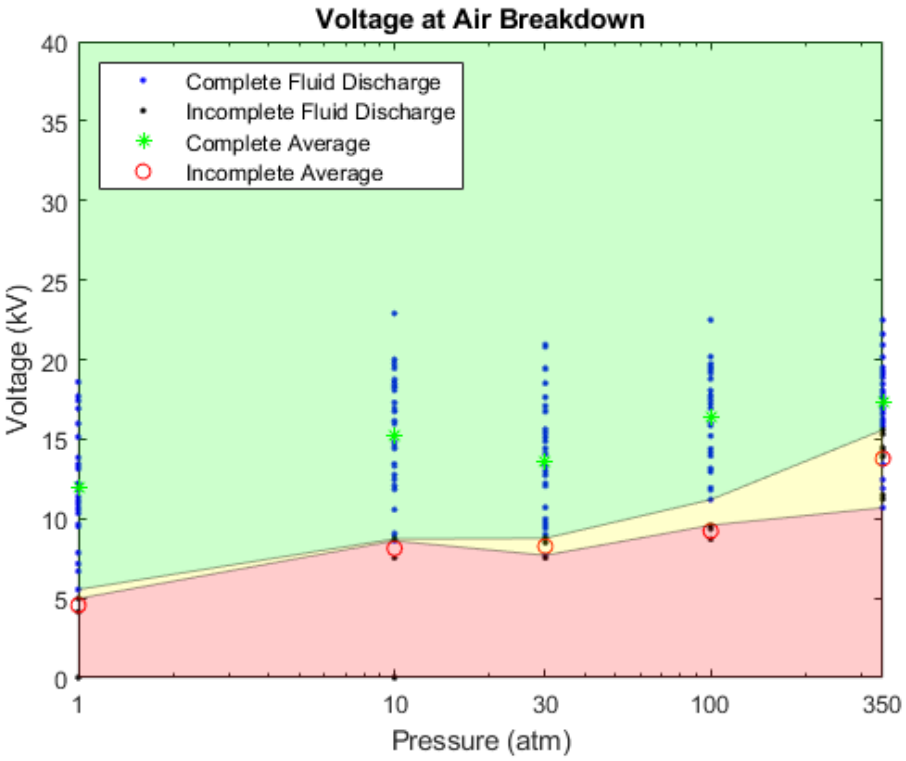

Figure 5.4: Required V2 voltage for a Complete Breakdown

5.3 Energy

The energies associated with the smaller gap and larger voltages appear to be slightly different than the energies discussed in chapter 4. Typical energy curves under these conditions can be found in figure 5.5. There are two primary differences between these energy curves and the ones found

in figure 4.15. First, the energy created before time zero (V2) tends to be much shorter. This leads to significantly more energy occurring within the primary discharge. Secondly, the discharge event has much larger and longer lasting oscillations. This is likely due to the larger discharge energies seen.

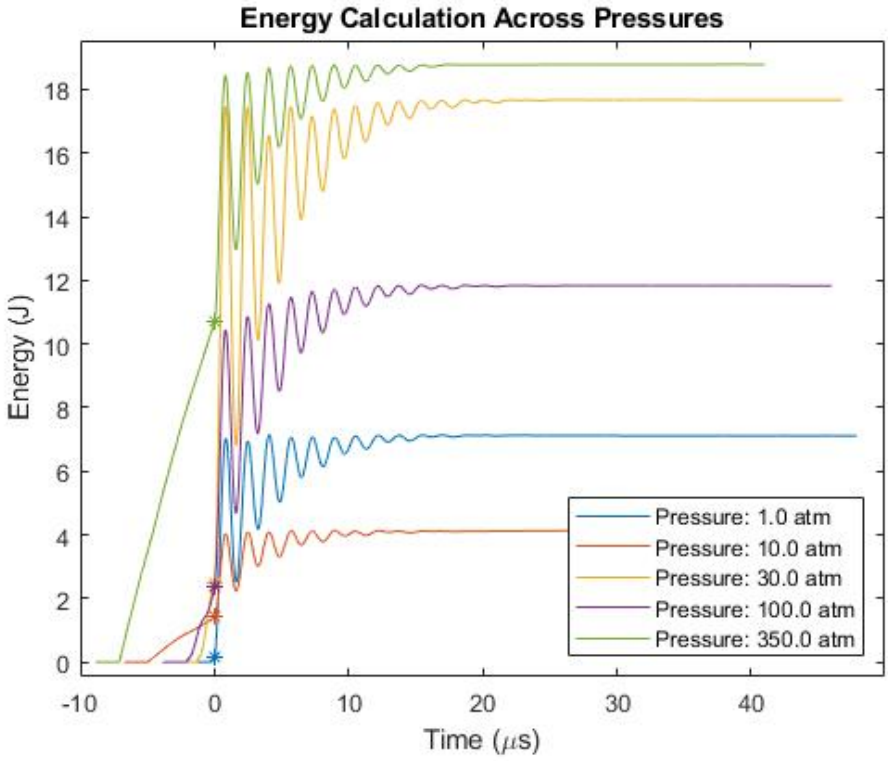

Figure 5.5: Typical Energy vs Time Curves

The change of energy from before V2 to after V2 can be easily seen in figure 5.6. A significantly smaller amount of energy is lost to inefficiencies and instead much of it is deposited into the primary plasma discharge. It seems the minimized gap and voltage range that was explored (5kV - 25 kV) provided sufficient potential to push majority of the discharge to after V2 in all of the pressures except for 350 atm. The data here suggests that the arrangement of this setup is much better suited for drilling applications.

The lag between V1 and V2 was explored extensively within Chapter 4. Figure 5.7 explores

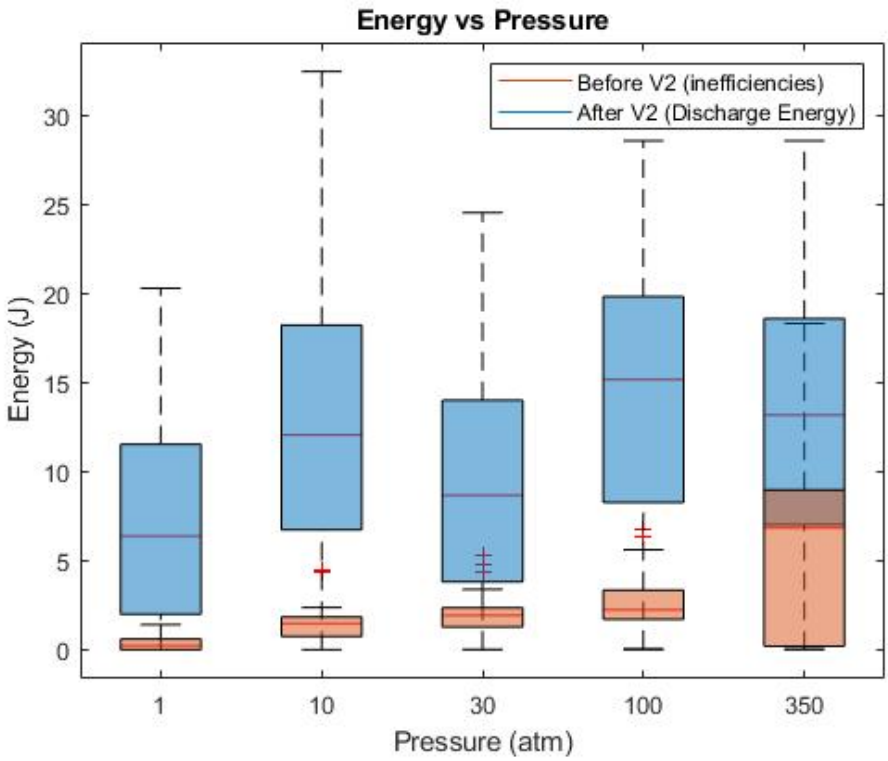

Figure 5.6: Energy vs Pressure, Before and After Plasma Breakdown

the connection between this lag time and the energy of the discharge. This graph makes it clear that a reduction in this lag time results in an increase of Energy. However, as you increase in pressure lag time tends to increase. Furthermore, there is a threshold where lag seems to stop effecting the discharge energy. Once the event becomes rapid enough the majority of the energy occurs after V2 and no additional gains are found with lower breakdown times. At pressures between 1 atm and 100 atm this happens before 2 μs of lag. For this reason, a 2μs or shorter lag time is recommended to achieve efficient discharges.

5.4 Overvoltage

In order to achieve these efficient, instant discharges a specific criteria must be made. Namely, it seems that a certain voltage threshold above the minimum is needed. Figure 5.4 shows the minimum breakdown threshold for this small gap setup (shown in yellow). Exceeding this threshold will be referred to as overvoltaging the system. In other words, the voltage that meets the primary

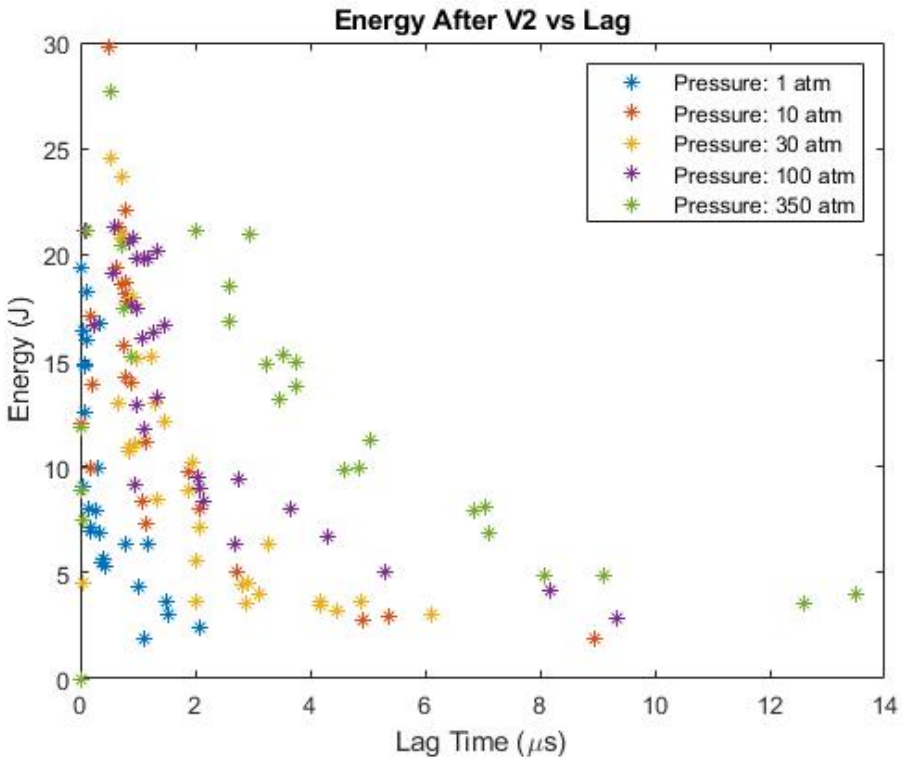

Figure 5.7: Discharge Energy vs Lag Time

spark gap is more than sufficient to create breakdown. Figure 5.8 explores this characteristic by plotting voltage above minimum required (overvoltage) vs the lag within the system. It is clear to see from this graph shows that reaching sufficient overvoltage values directly correlates to lower lag times. Namely it seems that reaching at least 7 kV over the threshold allows for the lag time to be minimized under 2 μs. This corresponds to the objective gathered from figure 5.7 of keeping the lag time under 2 μ for best efficiently.

The energy figures above can be moderately misleading as an increase within voltage will directly increase the energy. To clarify the benefit of overvoltaging, figure 5.9 shows how increasing voltage above the lower threshold shifts the energy from before V2 to after V2. This graph makes it clear that increasing the percent of energy within the primary discharge over early inefficiencies can be achieved by increasing the overvoltage value. Furthermore, it seems higher pressures require a higher overvoltage values to meet the same efficiency values. In coordination the the

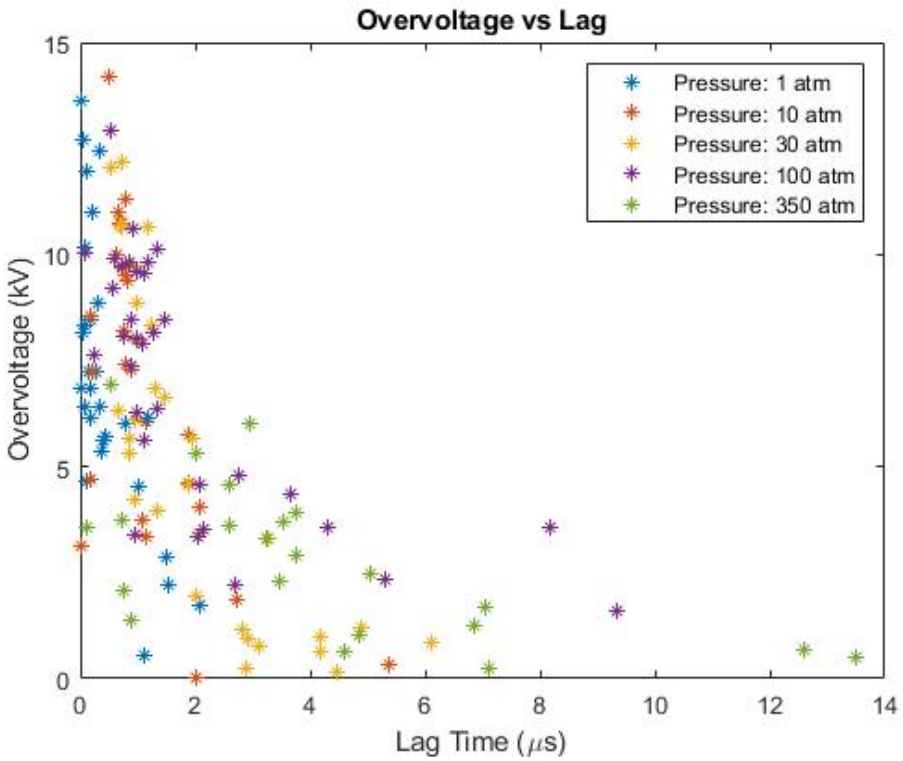

Figure 5.8: Overvoltage vs Lag Time

discussion above, 7 kV above the threshold seems to ensure 80% of the energy after V2, especially in lower pressures.

In order to understand the correlation between the overvoltage value and the discharge energy figure 5.10 was created. The first thing to note about this graph is that higher pressures seem to generate more discharge energy for any given Voltage. This is due to the fact that higher pressures require larger baseline voltages in order to create breakdown. This baseline increase in voltage corresponds to the rightward shift of higher pressures on this plot. Secondly, and less obvious, a discontinuity can be seem at most pressures around 5 kV. It is expected that energy will increase with voltage, but the slope seems to shift slightly at this point. That is to say after a threshold near 5 kV that your J/kV efficiency increases slightly.

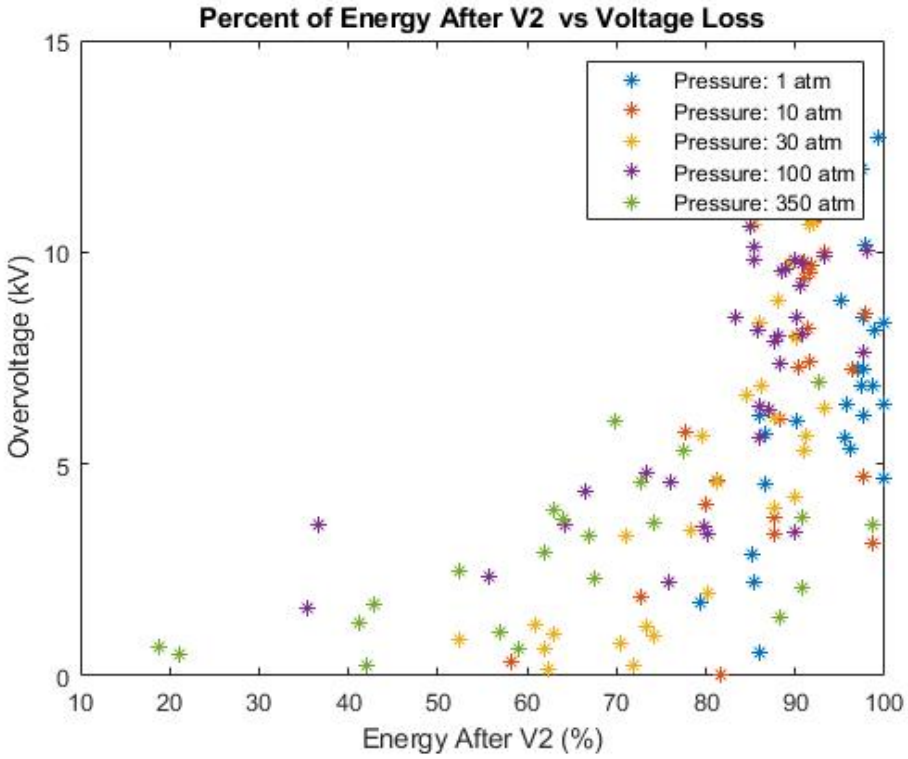

Figure 5.9: Percent of Energy within Main Discharge vs Overvoltage

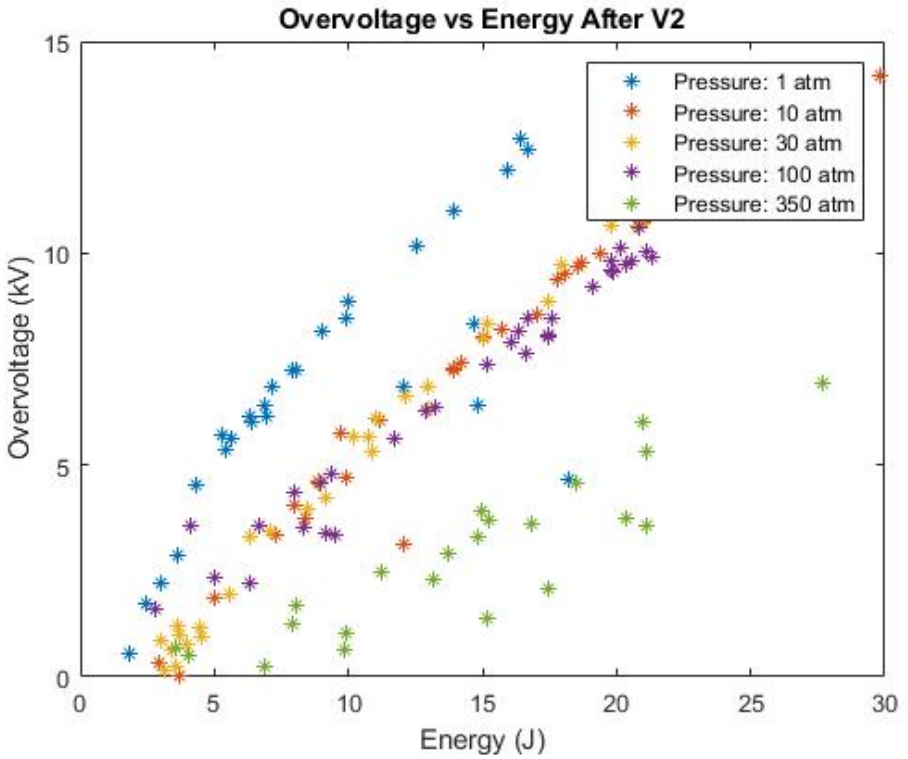

Figure 5.10: Overvoltage Vs Energy

6. PLASMA VISUALIZATION AND CHARACTERIZATION

6.1 Intensity Analysis

An experiment was conducted that evaluated the time resolved light emission of the pressurized plasma at several different pressures. The data was gathered through ICCD images triggered by the rise in current. Each data point consists of an individual discharge and matching ICCD image. The timing of image was manually read from the oscilloscope and is measured from the moment the current begins to increase during the primary discharge event. This experiment was repeated at seven different pressures.

The intensity values for each experiment can be found by taking the sum of each pixel that has a value statistically greater than the background. As a result, a discharge with more, bright pixels with measure as more intense. Figure 6.1 shows this data. Each curve is stitched together with 150-200 discharges and then binned by time to increase readability. The data is inherently choppy due to the natural variation from discharge to discharge, but the binned data makes drawing conclusions much easier. It is clear to see that the majority of the the intensity occurs within the first 5 microseconds of the event. The curve at 340 atm the most intense for almost all points along the graph. On the other hand, the 1 atm curve seems to represent the lower bound for the intensity values. This encourages the possibility that light emission increases with pressure.

Furthermore, figure 6.2 illustrates the number of pixels that are statistically significant. This metric can be correlated to the size of the event. That is to say the more pixels that show as intensely bright, the larger the even is. The peak area of the plasma seems to occur at roughly the same time as intensity, but it maintains it's size for much longer than it holds its intensity. This dimming nature is evident below when in figures 6.6 and 6.7.

In order to gather a better understanding of the intensity that occurs at each pressure a histogram of intensity at each pressure was created. Figure 6.3 illustrates the statistics associated with all the data points for each pressure. An interesting bi-modal behavior can be identified. The upper limit

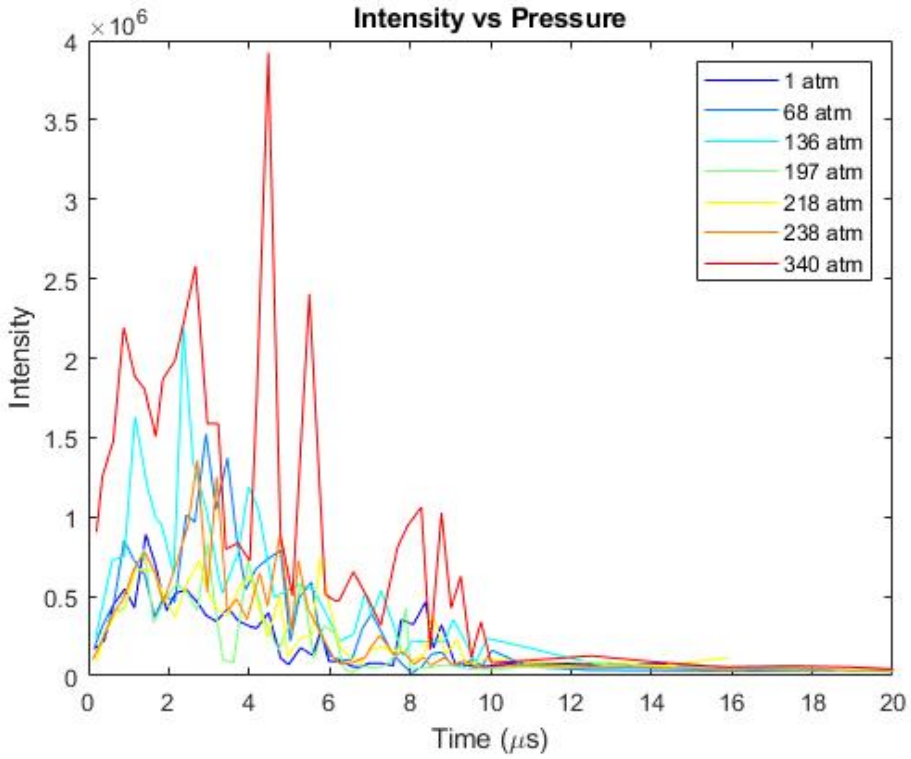

Figure 6.1: Intensity vs Pressure

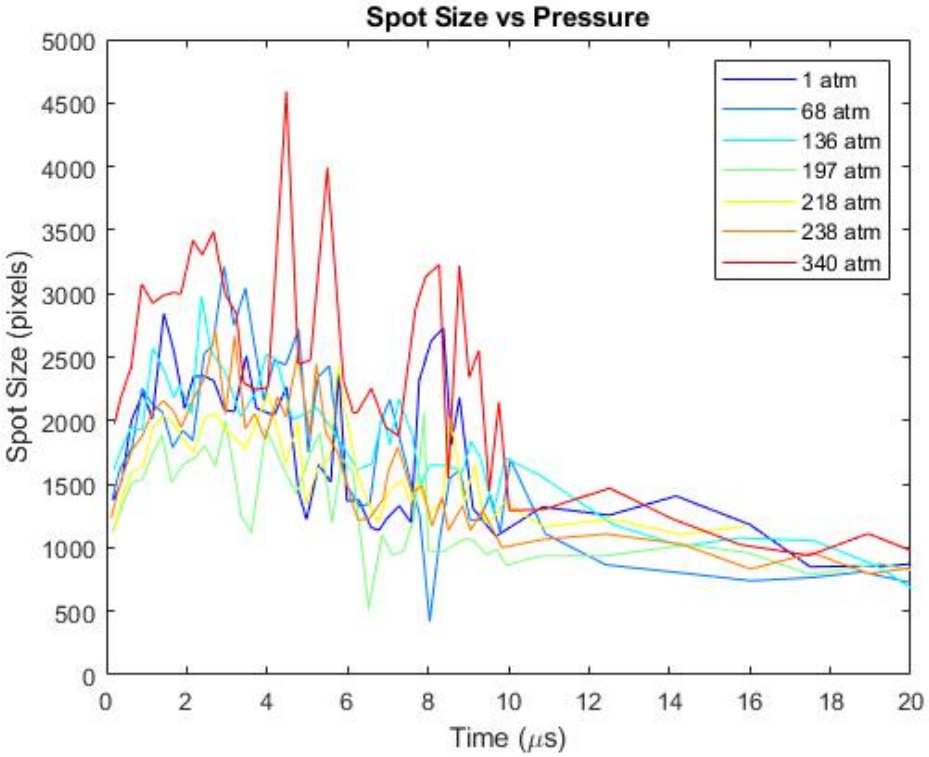

Figure 6.2: Spot Size vs Pressure

of the intensity seems to increase, then decrease near 218 atm, then increase from there out. The interesting aspect of this behavior is that the second minimum point seems to occur at the critical point of water (218 atm). This could indicate changes in absorption or reflectivity within the water near this point. The average values represented by the red lines do not vary significantly until 340 atm is reach when the intensity is significantly increased. Further experiments would need to be conducted to determine the exact reason for this dip maximum intensity and the large increase associated with 340 atm.

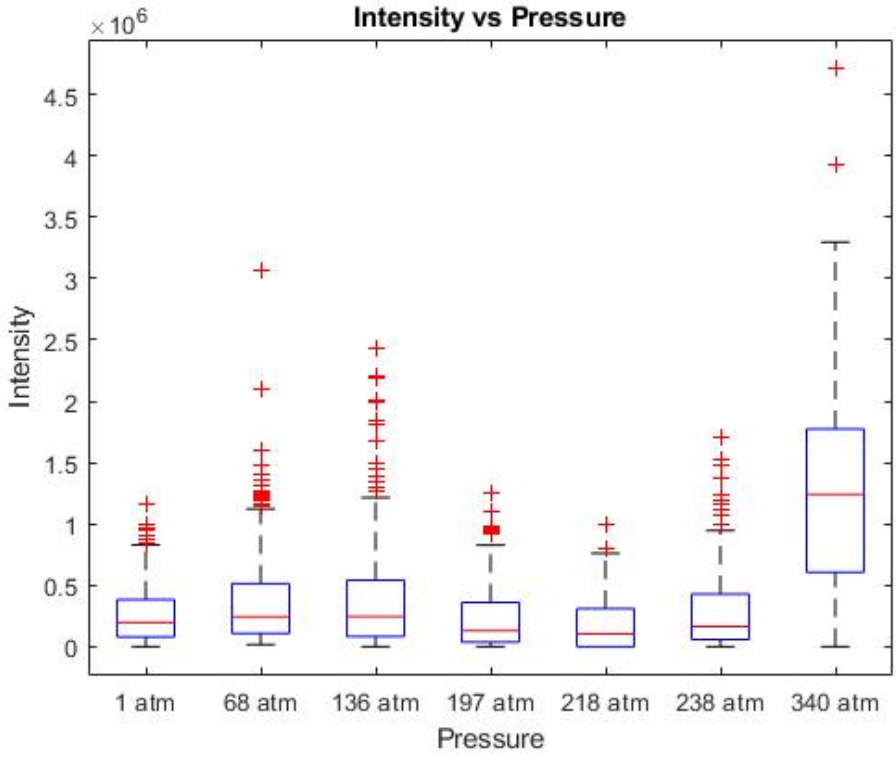

Figure 6.3: Intensity Statistics

It has been noted that the majority of the intensity values occur before 5 μs. In order to gain a better understanding of what is happening there figure 6.3 has be recreated utilizing intensity values only before 5 μs. These histograms can be found in figure 6.4. The differences between the two graphs remain quite small. The primary difference is that the second observes higher averages

and less outliers.

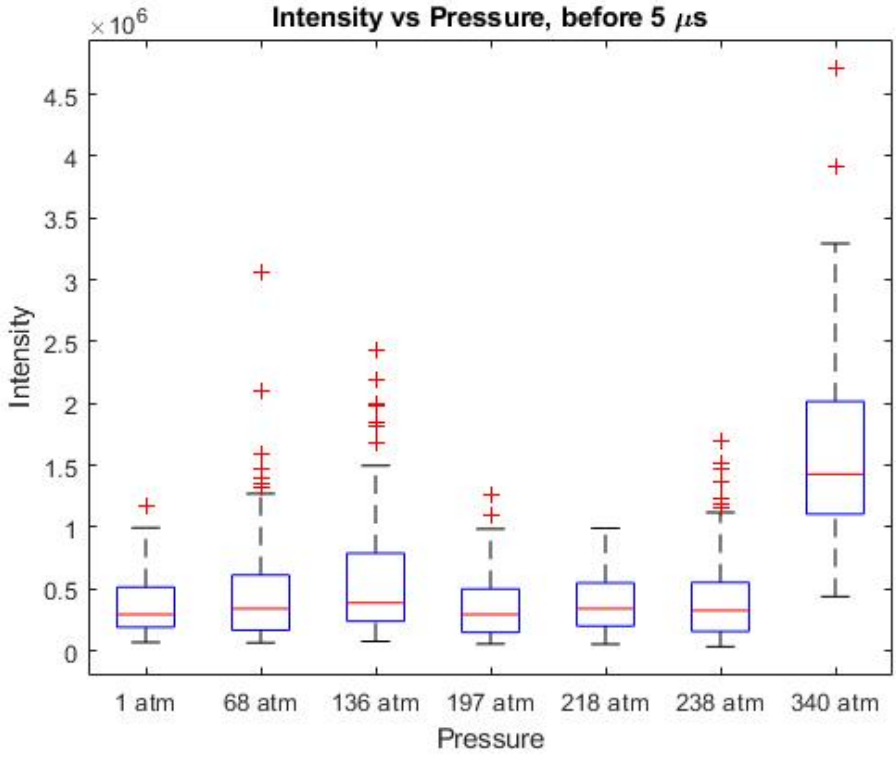

Figure 6.4: Intensity Statistics, Before 5μs

The oscilloscope data was saved from two of these experiments - 68 atm and 197 atm. Due to the time intensive nature of saving these results the data was not collected at every pressure. Figure 6.5 shows a scatter plot of instantaneous current vs light intensity. A clear floor can be seen that as the current increases, the intensity will increase to a certain extent or more. There is a large amount of variability on many of the more intense points as to where they fall within the plot. This data does go to show that there is come correlation between the current the plasma is experiencing at any given moment and the light intensity it is emitting.

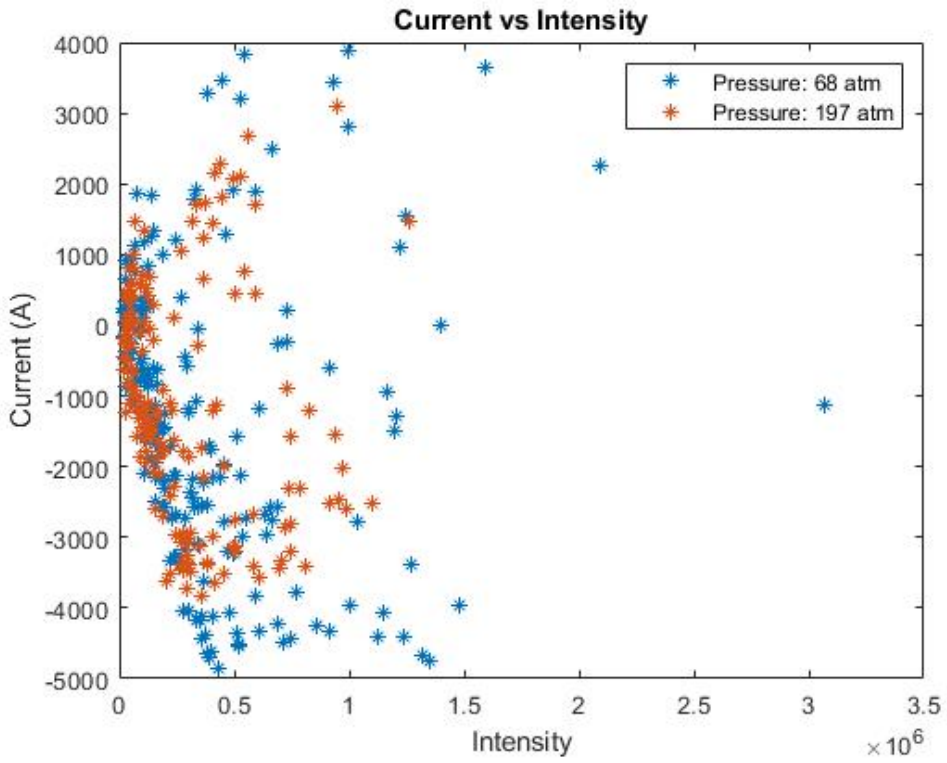

Figure 6.5: Intensity vs Current

6.2 Imaging of Pressurized Discharges

6.2.1 ICCD Results

Still images from the ICCD are shown below in figures 6.6 and 6.7. The yellow circle represents the region of interest and the colors correspond to the intensity at each pixel. As each image is analyzed, a correlation can be drawn between the growth and intensity of the discharge with the data shown above within the current/intensity plots. The discharge will grow, become bright and intense before it will fades and spreads out. By 2000 ns the majority of the intense light has gone and a dim patch of light will linger for the remaining several microseconds. Additional ICCD images of different pressures can be found in apendix A.

These images highlight a few characteristics. First, it is apparent that there is some amount of variability from event to event. As each one of these images is a separate event they will tend to represent different shapes or peak intensity from discharge to discharge. Furthermore, a subtle

pulsing can be seen as the current oscillates. The events that occur at higher currents will show brighter on average than the moments of lower current.

6.2.2 High Speed Camera

The experiment above was conducted while being filmed from a high speed camera. Figure 6.8 shows a complete discharge at 135 atm. The high speed camera is at a disadvantage as it is not capable of measuring under the 1 μs per frame, but it has the benefit of capturing several frames of the same event. It can be seen that the event begins near 4μs where a small amount of light is emitted from the left electrode. At 42 μs the camera becomes saturated (another downfall of the high speed camera). The camera remained saturated for the next 13 μs until 55 μs into the event where the intensity began to wane. Light emission remained until 59 μs into the event where it lessened. From that point onward the camera was able to image the resultant haziness that is likely caused by small created bubbles.

Figure 6.9 shows an incomplete discharge. Traces of the event begin near 9 μs. Instead of forming a complete plasma channel the energy is bleed off through heating, electrolysis, and other effects. Foggy shapes can be seem being emitted from both electrodes as the event occurs. An incomplete discharge (similar to the one pictured in 4.3 can last longer than 35 μs but typically less than 100 μs. At some point before 6.9d the energy will have depleted and the remaining images show the flow of the haze after the fact.

6.3 Plasma Characterization

Plasma can be characterized by the electron density and temperature within the plasma channel. The data gathered within these experiments is sufficient to approximate the peak electron density of the plasma. By finding this value it is possible to gain a better understanding of the type of plasma that is occurring. Furthermore, it offers some level of reference to other similarly design plasma devices.

The electron density can be found using equation 6.1 from Raizer[30]. Where j is current density, I is current, A is plasma area, e is electron charge, n_e is electron density, and v_d is electron

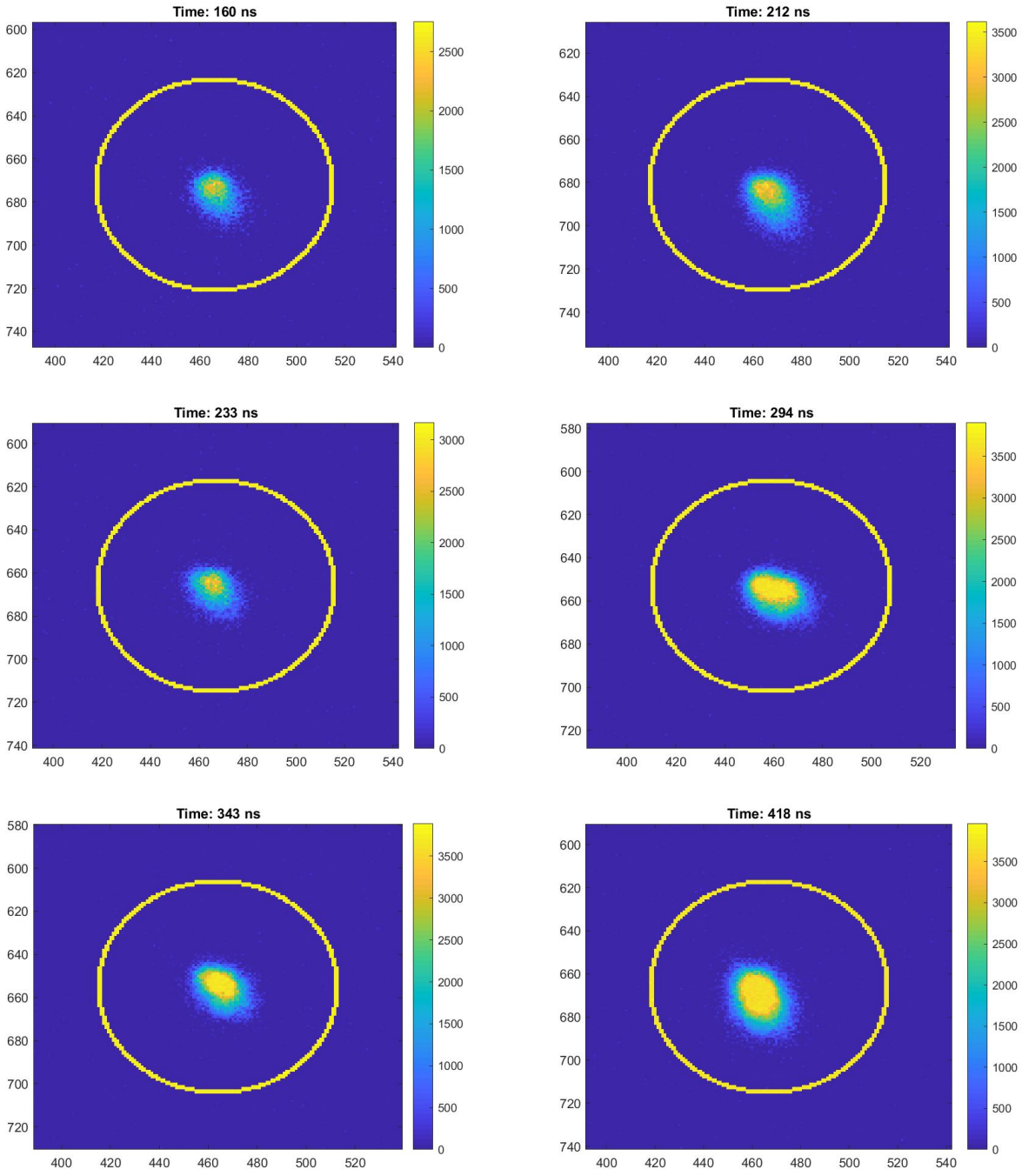

Figure 6.6: ICCD Images, Pressure: 340 atm, Time: 160 ns - 418 ns

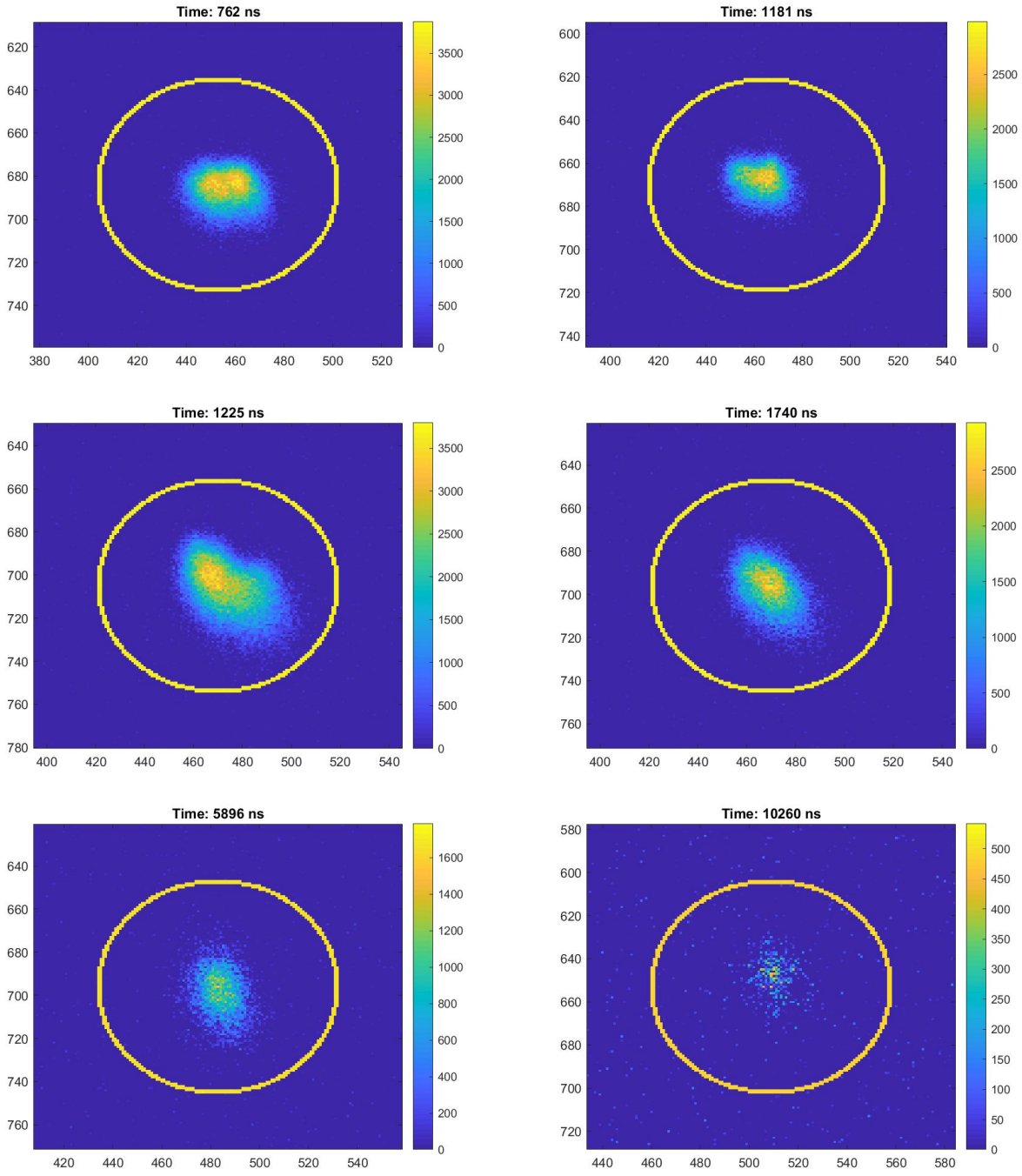

Figure 6.7: ICCD Images, Pressure: 340 atm, Time: 762 ns - 10260 ns

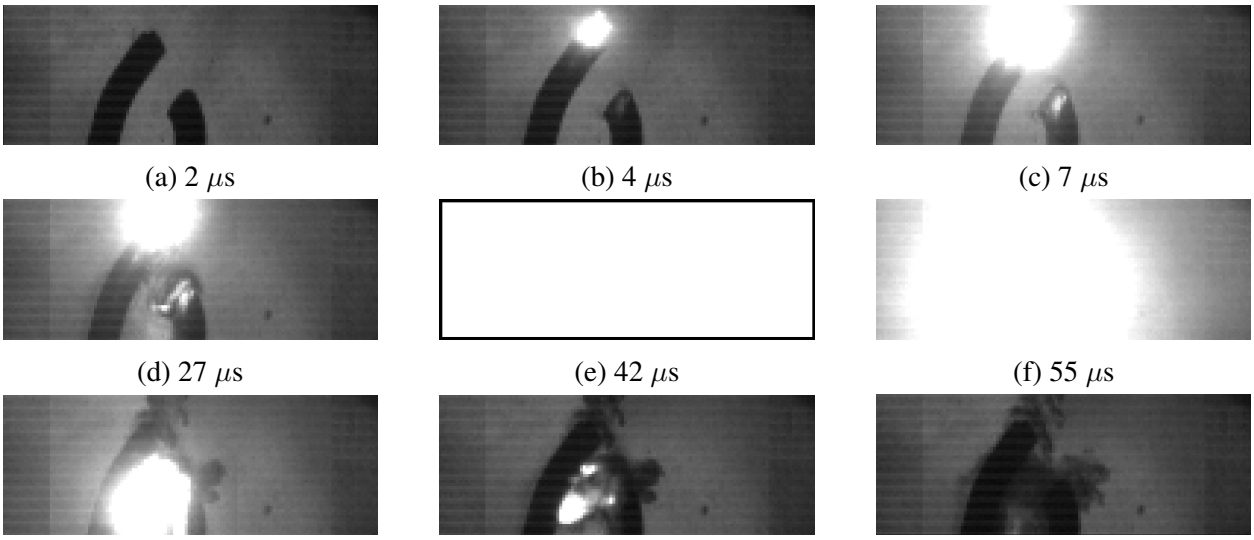

(a) 2 μs (b) 4 μs (c) 7 μs

(d) 27 μs (e) 42 μs (f) 55 μs

(g) 57 μs (h) 59 μs (i) 135 μs

Figure 6.8: High Speed Imaging of a Complete Discharge at 135 atm

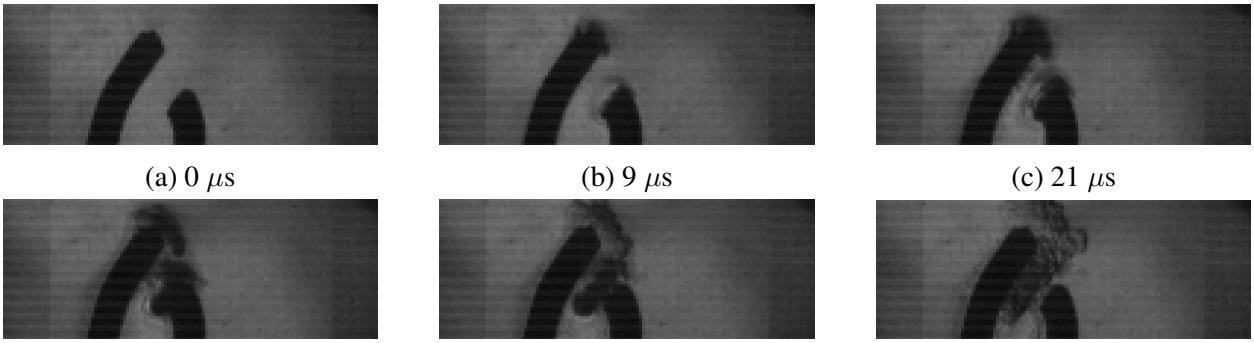

(a) 0 μs (b) 9 μs (c) 21 μs

(d) 122 μs (e) 453 μs (f) 1242 μs

Figure 6.9: High Speed Imaging of a Incomplete Discharge at 375 atm

drift. Current and area have been calculated from experimental results. The electron charge and electron drift can be estimated from known data in Raizer's book. This leaves electron density as the only unknown.

$$j = \frac{I}{A} = en_e v_d \tag{6.1}$$

A breakdown of equation 6.1 with know values is shown in equation 6.3. It can be seen that

the electron density of these charges should be somewhere on the order of $3 * 10^{18} \frac{1}{cm^3}$. This value will change slightly as the area and current fluctuate during each discharge.

$$j = \frac{I}{A} = \frac{1000C/s}{.000625cm^2} = en_e v_d = 1.60217646 * 10^{-19} C * n_e * 3 * 10^6 cm/s \tag{6.2}$$

$$n_e \approx 3.3 * 10^{18} \frac{1}{cm^3} \tag{6.3}$$

7. CONCLUSIONS

7.1 Conclusion

Plasma research and technology has been present for many years. However, there has been a surge of plasma related technologies across the last decade. It is proposed that the rapid energy release involved within a nanosecond pulsed plasma discharge is significant enough to weaken rock structure to allow for improvements in traditional drilling. The proposed research above has laid the groundwork necessary to design a plasma system capable of utilization at downhole conditions. The findings of these experiments has also help to fill the gap of a little researched area in plasma science.

A number of pressurized plasma events were studied at pressures ranging from 1 atm to 350 atm. The trials evaluated were near the minimum voltage required for breakdown. A characteristic lag between the air spark switch and the primary plasma discharge was identified. During this lag substantial voltage and energy is lost. The characteristics of this lag and loss was evaluated over the observed pressures. It was found that the lost voltage increased as pressure increased, the lag time increased only at 350 atm, and the voltage loss per second increases as the pressure is increased.

The energy of these discharges was calculated and evaluated for each pressure. It was found that high pressures require higher energy discharges. This is primarily due to the higher required breakdown voltage. Despite an increase of energy with pressure, the discharge energy remained fairly constant throughout every pressure. The importance of minimizing the lag between discharges and voltage loss before the pressurized discharge is highlighted. The minimum breakdown voltage for each observed pressure was reported showing a slight upward trend as higher pressures were met. The breakdown voltage at 1 atm for this configuration was around 14 kV while the breakdown voltage for 350 atm was roughly 25 kV.

A second experiment was conducted utilizing a smaller pressurized spark gap and overvoltaged input voltages in an attempt to improve the efficiency of the system. It was found that a significantly

overvoltaged system (7+ kV over the minimum breakdown voltage) could bypass the observed lag time in the first experiment. Once sufficiently overvoltaged the primary discharge is capable of discharging within 100 ns of the air spark switch. This leaves no time for any significant loss of energy allowing the majority of the stored energy to be released within the primary discharge. Furthermore, by decreasing the spark gap from 0.75 mm to 0.25 mm it was possible to reduce the minimum required voltage by up to 10 kV at all pressures. These changes made it possible to shift the majority (80%+) of the energy into the primary discharge as opposed to the inefficiencies that occurred during the lag time.

Two more experiments were performed that focused on imaging the pressurized discharge. The first was an extensive test that characterized the intensity of the plasma throughout the duration of the discharge with ICCD imaging. It was found that higher pressure discharges tend to be more intense. Furthermore, the majority of that intensity occurs within the first 5 μs. On the other hand, the size of the discharge tends to peak around 3 or 4 μs and then tapers out until the end of the event. Several time resolved images of the plasma event were reported as a means of understanding the change of shape and intensity as the event progresses. The second experiment was very similar but utilized a high speed camera instead of an ICCD. Time resolved images from this event are reported as well. The high speed camera enables visualization of both the complete discharges and the incomplete discharges. It's clear to see the plasma begin at one point on a single electrode the grow into a completely saturated image. The saturated image persisted for up to 13 μs before fading away. Upon the completion of the event a visible fog remains for hundreds of microseconds. Lastly, the current and spot size data is utilized to calculate an approximate electron density. This value was found and reported to be $3.3 \cdot 10^{18} \frac{1}{cm^3}$.

The hypothesis of this paper is that a plasma discharge will remain feasible throughout the pressures explored indicating its potential for downhole application. It has been shown that strong plasma discharges are capable up to 350 atm. This is evidence in of itself that this plasma interaction is possible at most downhole pressures. A number of recommendations have been made in order to optimize the downhole plasma event. First, minimizing the lag between the air spark

switch and the primary discharge to under 2 μs will improve efficiencies. This can often be reached by providing an input voltage that is at least 7 kV above the minimum voltage required for breakdown. Lastly, Minimizing the electrode gap will lower the minimum required voltage at every pressure. The plasma events explored here excel focusing significant energy within a very short time-span allowing for destructive results. The results of this paper encourage further research of this technology as a means of improving traditional drilling.

7.2 Future Work

The research within this paper serves as a foundation for hybrid plasma drilling. There are many avenues that will need to be explored to further prove this technology's feasibility. Extreme pressures in downhole drilling can reach pressures higher than the range explored here. In order to understand the mechanisms at such pressures many of the experiments discussed here would have to be repeated at those more extreme conditions. Furthermore, it will be critical to prove the plasma's ability to operate up against a substrate and its potential for inducing cracks, especially at high pressures. In order to maximize the induced cracks the input energy and frequency will need to be explored. There is undoubtedly an upper limit for both where the costs outweigh the benefits. Finding the ideal input parameters to induce rock cracks will greatly aid in making the technology feasible. Assuming this technology remains viable at ultra high pressures and creates suitable cracks within the rock then the economics and feasibility of implementation will need to be explored.

A single traditional drill bit will be used in operation for as long as possible, typically up to four days of continuous use. A work/wear analysis of the electrodes will need to be conducted to ensure that they are able to outlast the drill bit within these downhole conditions. The economics of adding the equipment required to implement this technology compared to the benefits it brings will have to be proven. As is evident there are still many hurdles for this technology. The experiments discussed here help to highlight the path moving forward. This technology shows promise in many ways and will undoubtedly find a spot within the oil, gas, and geothermal industry where it is capable of creating an impact.

REFERENCES

[1] K. Takaki and S. Katsuki, "Industrial applications of pulsed power technology," 2009.

[2] G. Fridman, G. Friedman, A. Gutsol, A. B. Shekhter, V. N. Vasilets, and A. Fridman, "Applied plasma medicine," aug 2008.

[3] K. R. Stalder, D. F. McMillen, and J. Woloszko, "Electrosurgical plasmas," in *Journal of Physics D: Applied Physics*, vol. 38, pp. 1728–1738, jun 2005.

[4] M. S. Hutson and X. Ma, "Plasma and cavitation dynamics during pulsed laser microsurgery in vivo," *Physical Review Letters*, vol. 99, oct 2007.

[5] C. Jiang, M. T. Chen, A. Gorur, C. Schaudinn, D. E. Jaramillo, J. W. Costerton, P. P. Sedghizadeh, P. T. Vernier, and M. A. Gundersen, "Nanosecond Pulsed Plasma Dental Probe," *Plasma Processes and Polymers*, vol. 6, pp. 479–483, aug 2009.

[6] M. Deilmann, M. Grabowski, S. Theiß, N. Bibinov, and P. Awakowicz, "Permeation mechanisms of pulsed microwave plasma deposited silicon oxide films for food packaging applications," *Journal of Physics D: Applied Physics*, vol. 41, jul 2008.

[7] N. Puač, M. Gherardi, and M. Shiratani, "Plasma agriculture: A rapidly emerging field," *Plasma Processes and Polymers*, vol. 15, feb 2018.

[8] L. Sivachandiran and A. Khacef, "Enhanced seed germination and plant growth by atmospheric pressure cold air plasma: combined effect of seed and water treatment," *RSC Advances*, vol. 7, no. 4, pp. 1822–1832, 2017.

[9] M. Sato, "Environmental and biotechnological applications of high-voltage pulsed discharges in water," *Plasma Sources Science and Technology*, vol. 17, may 2008.

[10] K. Shimizu, "Pulsed-plasma treatment of polluted gas using wet-/low-temperature corona reactors," *IEEE Transactions on Industry Applications*, vol. 33, no. 5, pp. 1373–1380, 1997.

[11] A. Pokryvailo, Y. Yankelevich, M. Wolf, E. Abramzon, S. Wald, and A. Welleman, "A high-power pulsed corona source for pollution control applications," *IEEE Transactions on Plasma Science*, vol. 32, pp. 2045–2054, oct 2004.

[12] A. B. Ustimenko, "Plasma Application for Coal Combustion Activation COMPUTATIONAL EXPERIMENTS ON COMBUSTION PROCESS OF LOW-GRADE COAL View project," tech. rep., 2004.

[13] J. E. Foster, "Plasma-based water purification: Challenges and prospects for the future," *Physics of Plasmas*, vol. 24, may 2017.

[14] C. Yamabe, F. Takeshita, T. Miichi, N. Hayashi, and S. Ihara, "Water treatment using discharge on the surface of a bubble in water," *Plasma Processes and Polymers*, vol. 2, pp. 246–251, mar 2005.

[15] G. R. Stratton, C. L. Bellona, F. Dai, T. M. Holsen, and S. M. Thagard, "Plasma-based water treatment: Conception and application of a new general principle for reactor design," *Chemical Engineering Journal*, vol. 273, pp. 543–550, aug 2015.

[16] S. I. Serbin, I. B. Matveev, and N. A. Goncharova, "Plasma-assisted reforming of natural gas for GTL-part i," *IEEE Transactions on Plasma Science*, vol. 42, pp. 3896–3900, dec 2014.

[17] G. Prieto, M. Okumoto, K. I. Shimano, K. Takashima, S. Katsura, and A. Mizuno, "Reforming of heavy oil using nonthermal plasma," *IEEE Transactions on Industry Applications*, vol. 37, no. 5, pp. 1464–1467, 2001.

[18] H. S. Kim, K. Wright, J. Piccioni, D. J. Cho, and Y. I. Cho, "Inactivation of bacteria by the application of spark plasma in produced water," *Separation and Purification Technology*, vol. 156, pp. 544–552, dec 2015.

[19] S. K. Chellappan, F. Al Enezi, H. A. Marafie, A. H. Bibi, and V. B. Eremenko, "First application of plasma technology in KOC to improve well's productivity," in *Society of Petroleum Engineers - SPE Kuwait Oil and Gas Show and Conference*, pp. 11–14, 2015.

[20] C. Chelaru, I. Diaconu, and C. I. Simionescu, "Polyacrylamide obtained by plasma-induced polymerization for a possible application in enhanced oil recovery," *Polymer Bulletin*, vol. 40, no. 6, pp. 757–764, 1998.

[21] I. V. Lisitsyn, H. Inoue, S. Katsuki, H. Akiyama, and I. Nishizawa, "Drilling and demolition of rocks by pulsed power," in *Digest of Technical Papers-IEEE International Pulsed Power Conference*, vol. 1, pp. 169–172, 1999.

[22] H. Schittenhelm, G. Callies, and P. Berger, "Characteristics of Plasma Shock Waves Generated in the Pulsed Laser Ablation Process Related content Investigations of extinction coefficients during excimer laser ablation and their interpretation in terms of Rayleigh scattering," tech. rep., 2002.

[23] M. N. Shneider and M. Pekker, "Cavitation in dielectric fluid in inhomogeneous pulsed electric field," *Journal of Applied Physics*, vol. 114, dec 2013.

[24] R. Caenn and G. V. Chillingar, "Drilling fluids: State of the art," *Journal of Petroleum Science and Engineering*, vol. 14, no. 3-4, pp. 221–230, 1996.

[25] S. Thorhallsson and B. M. Sveinbjornsson, "GEOTHERMAL DRILLING COST AND DRILLING EFFECTIVENESS," tech. rep., 2012.

[26] X. Tang and D. Staack, "Bioinspired mechanical device generates plasma in water via cavitation," *Science Advances*, vol. 5, no. 3, 2019.

[27] H. M. Jones and E. E. Kunhardt, "Pulsed dielectric breakdown of pressurized water and salt solutions," *Journal of Applied Physics*, vol. 77, no. 2, pp. 795–805, 1995.

[28] P. Xiao and D. Staack, "Microbubble generation by microplasma in water," *Journal of Physics D: Applied Physics*, vol. 47, sep 2014.

[29] J. Kriegseis, S. Grundmann, and C. Tropea, "Power consumption, discharge capacitance and light emission as measures for thrust production of dielectric barrier discharge plasma actuators," *Journal of Applied Physics*, vol. 110, jul 2011.

[30] B. H. Crichton, "Gas discharge physics," *IEE Colloquium (Digest)*, no. 173, p. 449, 1996.

[31] F. Romanelli, "Plasma Physics and Engineering," in *Nuclear Energy Encyclopedia*, pp. 371–388, Taylor & Francis, 2011.

[32] G. A. Mesyats, Y. I. Bychkov, and V. V. Kremnev, "To cite this article: É D Lozanski," tech. rep., 1975.

[33] J. F. Kolb, A. A. Mohamed, R. O. Price, R. J. Swanson, A. Bowman, R. L. Chiavarini, M. Stacey, and K. H. Schoenbach, "Cold atmospheric pressure air plasma jet for medical applications," *Applied Physics Letters*, vol. 92, no. 24, 2008.

[34] C. Campbell, X. Tang, Y. Sechrest, K. Fezzaa, Z. Wang, and D. Staack, "Ultrafast X-ray imaging of pulsed water plasmas for investigation of breakdown mechanisms and demonstration of a benchmark imaging target," pp. 1–6, 2020.

[35] T. J. Lewis, "Breakdown Initiating Mechanisms at Electrode Interfaces in Liquids," in *IEEE Transactions on Dielectrics and Electrical Insulation*, vol. 10, pp. 948–955, 2003.

[36] Y. Seepersad, M. Pekker, M. N. Shneider, A. Fridman, and D. Dobrynin, "Investigation of positive and negative modes of nanosecond pulsed discharge in water and electrostriction model of initiation," *Journal of Physics D: Applied Physics*, vol. 46, sep 2013.

[37] H. M. Jones and E. E. Kunhardt, "Development of pulsed dielectric breakdown in liquids," *Journal of Physics D: Applied Physics*, vol. 28, no. 1, pp. 178–188, 1995.

[38] J. Bernardes and M. F. Rose, "Electrical Breakdown Characteristics of Sodium Chloride - Water Mixtures," pp. 308–311, 1983.

[39] R. P. Joshi, J. Qian, K. H. Schoenbach, and E. Schamiloglu, "Microscopic analysis for water stressed by high electric fields in the prebreakdown regime," *Journal of Applied Physics*, vol. 96, pp. 3617–3625, oct 2004.

[40] A. Starikovskiy, Y. Yang, Y. I. Cho, and A. Fridman, "Non-equilibrium plasma in liquid water: Dynamics of generation and quenching," *Plasma Sources Science and Technology*, vol. 20, apr 2011.

[41] N. Y. Babaeva, D. V. Tereshonok, and G. V. Naidis, "Initiation of breakdown in bubbles immersed in liquids: pre-existed charges and proximity of bubbles," tech. rep., 2015.

[42] W. An, K. Baumung, and H. Bluhm, "Underwater streamer propagation analyzed from detailed measurements of pressure release," *Journal of Applied Physics*, vol. 101, no. 5, 2007.

[43] P. Tardiveau, N. Moreau, S. Bentaleb, C. Postel, and S. Pasquiers, "Diffuse mode and diffuse-to-filamentary transition in a high pressure nanosecond scale corona discharge under high voltage," *Journal of Physics D: Applied Physics*, vol. 42, no. 17, 2009.

[44] H. M. Jones and E. E. Kunhardt, "The influence of pressure and conductivity on the pulsed breakdown of water," *IEEE Transactions on Dielectrics and Electrical Insulation*, vol. 1, no. 6, pp. 1016–1025, 1994.

[45] Z. Lujun, "An energy-saving oil drilling rig for recovering potential energy and decreasing motor power," *Energy Conversion and Management*, vol. 52, no. 1, pp. 359–365, 2011.

[46] A. Vogel, S. Busch, and U. Parlitz, "Shock wave emission and cavitation bubble generation by picosecond and nanosecond optical breakdown in water," *The Journal of the Acoustical Society of America*, vol. 100, no. 1, pp. 148–165, 1996.

[47] D. L. Shmelev and S. A. Barengolts, "Kinetic modeling of initiation of explosion center on cathode under dense plasma," *IEEE Transactions on Plasma Science*, vol. 41, no. 8, pp. 1959–1963, 2013.

[48] J. R. Sukovich, P. A. Anderson, A. Sampathkumar, D. F. Gaitan, Y. A. Pishchalnikov, and R. G. Holt, "Outcomes of the collapse of a large bubble in water at high ambient pressures," *Physical Review E*, vol. 95, no. 4, pp. 1–13, 2017.

[49] E. Klaseboer, K. C. Hung, C. Wang, C. W. Wang, B. C. Khoo, P. Boyce, S. Debono, and H. Charlier, "Experimental and numerical investigation of the dynamics of an underwater ex-

plosion bubble near a resilient/rigid structure," *Journal of Fluid Mechanics*, vol. 537, pp. 387–413, aug 2005.

[50] P. Hartlieb, B. Grafe, T. Shepel, A. Malovyk, and B. Akbari, "Experimental study on artificially induced crack patterns and their consequences on mechanical excavation processes," *International Journal of Rock Mechanics and Mining Sciences*, vol. 100, pp. 160–169, dec 2017.

[51] L. R. O'Hare, "Shock Plasma Earth Drill," 1972.

[52] F. Howell, "Novel drilling techniques," *International Journal of Machine Tool Design and Research*, vol. 9, no. 2, p. 215, 1969.

[53] F. Kitzinger and J. Nantel, "Plasma blasting method," 1991.

[54] I. V. Timoshkin, J. W. Mackersie, and S. J. MacGregor, "Plasma channel miniature hole drilling technology," *IEEE Transactions on Plasma Science*, vol. 32, pp. 2055–2061, oct 2004.

[55] Y. Sun, R. Fu, A. Fan, Y. Gao, and P. Yan, "Study of rock fracturing generated by pulsed discharging under confining pressure," in *Digest of Technical Papers-IEEE International Pulsed Power Conference*, vol. 2015-Octob, Institute of Electrical and Electronics Engineers Inc., oct 2015.

[56] C. Li, L. Duan, S. Tan, and V. Chikhotkin, "Influences on high-voltage electro pulse boring in granite," *Energies*, vol. 11, sep 2018.

[57] G. Pastras, A. Fysikopoulos, P. Stavropoulos, and G. Chryssolouris, "An approach to modelling evaporation pulsed laser drilling and its energy efficiency," *International Journal of Advanced Manufacturing Technology*, vol. 72, no. 9-12, pp. 1227–1241, 2014.

[58] W. A. Hustrulid and C. Fairhurst, "A theoretical and experimental study of the percussive drilling of rock Part IV-application of the model to actual percussion drilling," *International Journal of Rock Mechanics and Mining Sciences and*, vol. 9, no. 3, pp. 431–442, 1972.

[59] M. Saadati, P. Forquin, K. Weddfelt, P. L. Larsson, and F. Hild, "A numerical study of the influence from pre-existing cracks on granite rock fragmentation at percussive drilling," *International Journal for Numerical and Analytical Methods in Geomechanics*, vol. 39, pp. 558–570, apr 2015.

[60] G. Han and M. Bruno, "Percussion drilling: From laboratory tests to dynamic modeling," in *International Oil and Gas Conference and Exhibition in China 2006 - Sustainable Growth for oil and Gas*, vol. 2, pp. 751–759, 2006.

[61] S. Liu, H. Li, and H. Chang, "Drilling Performance of Rock Drill by High-Pressure Water Jet under Different Configuration Modes," *Shock and Vibration*, vol. 2017, 2017.

[62] M. A. Kant, E. Rossi, D. Becker, R. Von Rohr, and E. Zurich, "Enhancing the Drilling Process for Geothermal Resources by Combining Conventional Drilling and the Spallation Technology," tech. rep., 2017.

[63] E. Rossi, S. Jamali, V. Wittig, M. O. Saar, and P. Rudolf von Rohr, "A combined thermo-mechanical drilling technology for deep geothermal and hard rock reservoirs," *Geothermics*, vol. 85, may 2020.

[64] W. M. Moeny, "Method of Drilling Using Pulsed Electric Drilling," 2009.

APPENDIX A

FIRST APPENDIX - ICCD IMAGES

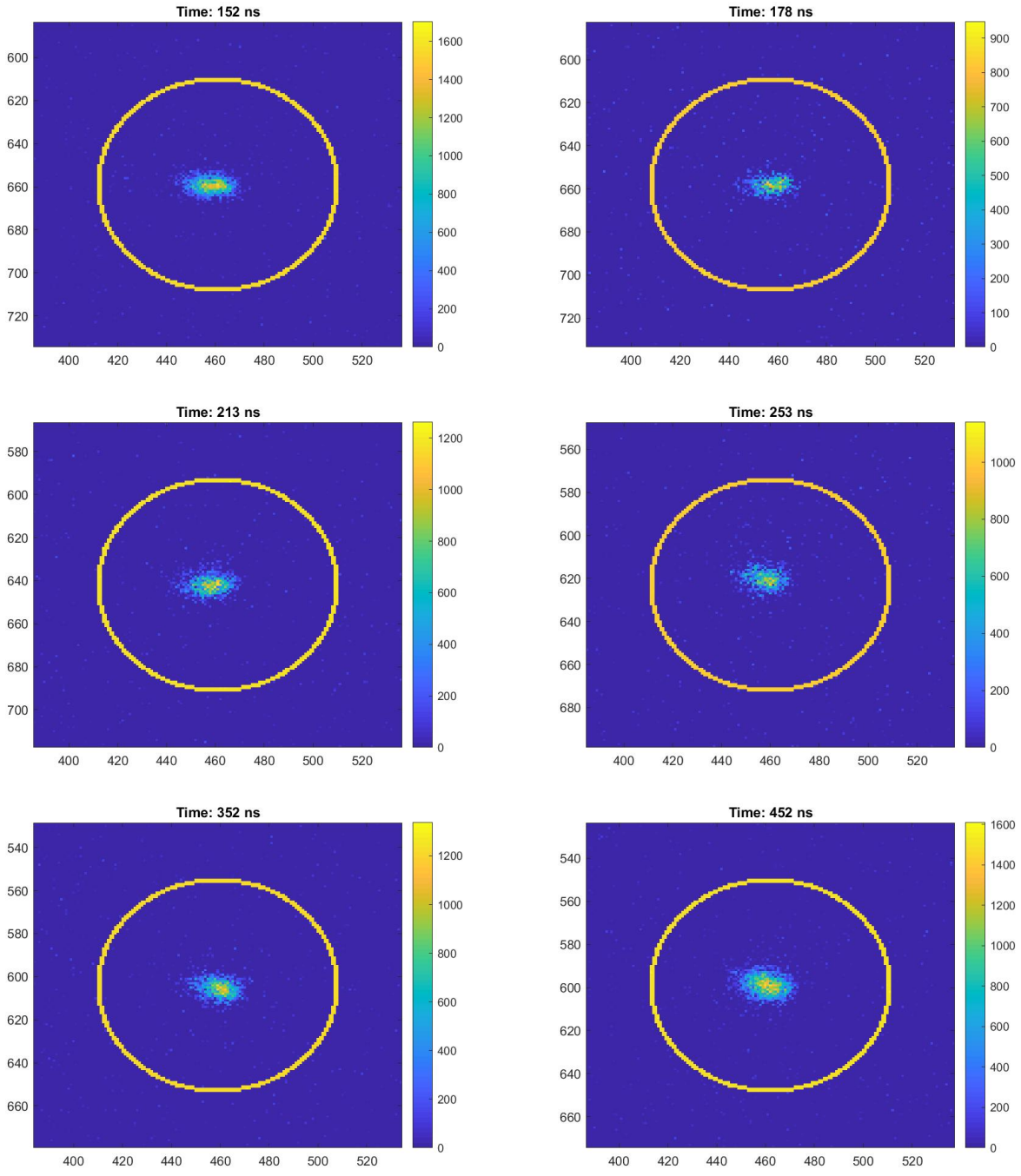

Figure A.1: ICCD Images, Pressure: 1 atm, Time: 152 ns - 452 ns

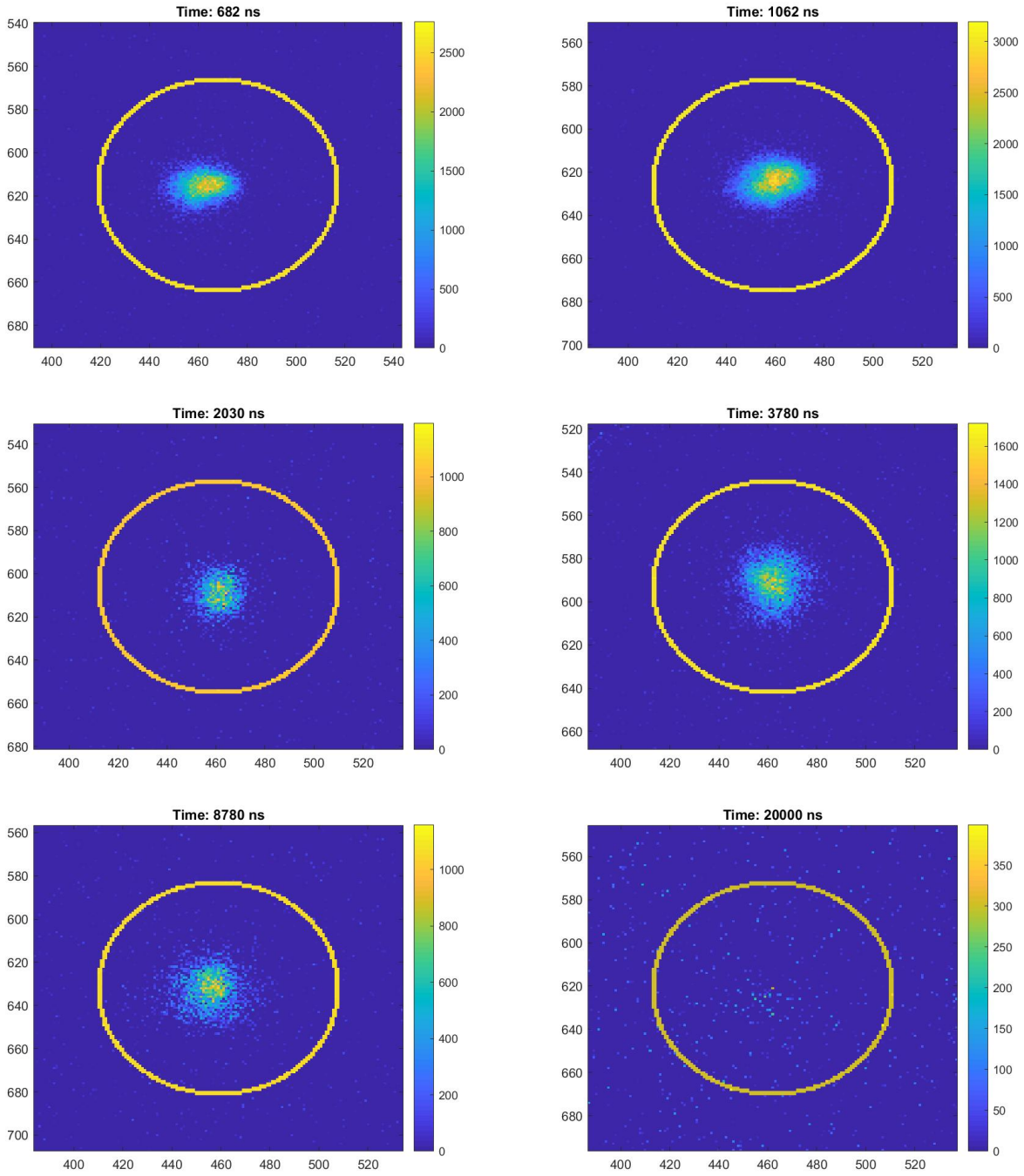

Figure A.2: ICCD Images, Pressure: 1 atm, Time: 682 ns - 20000 ns

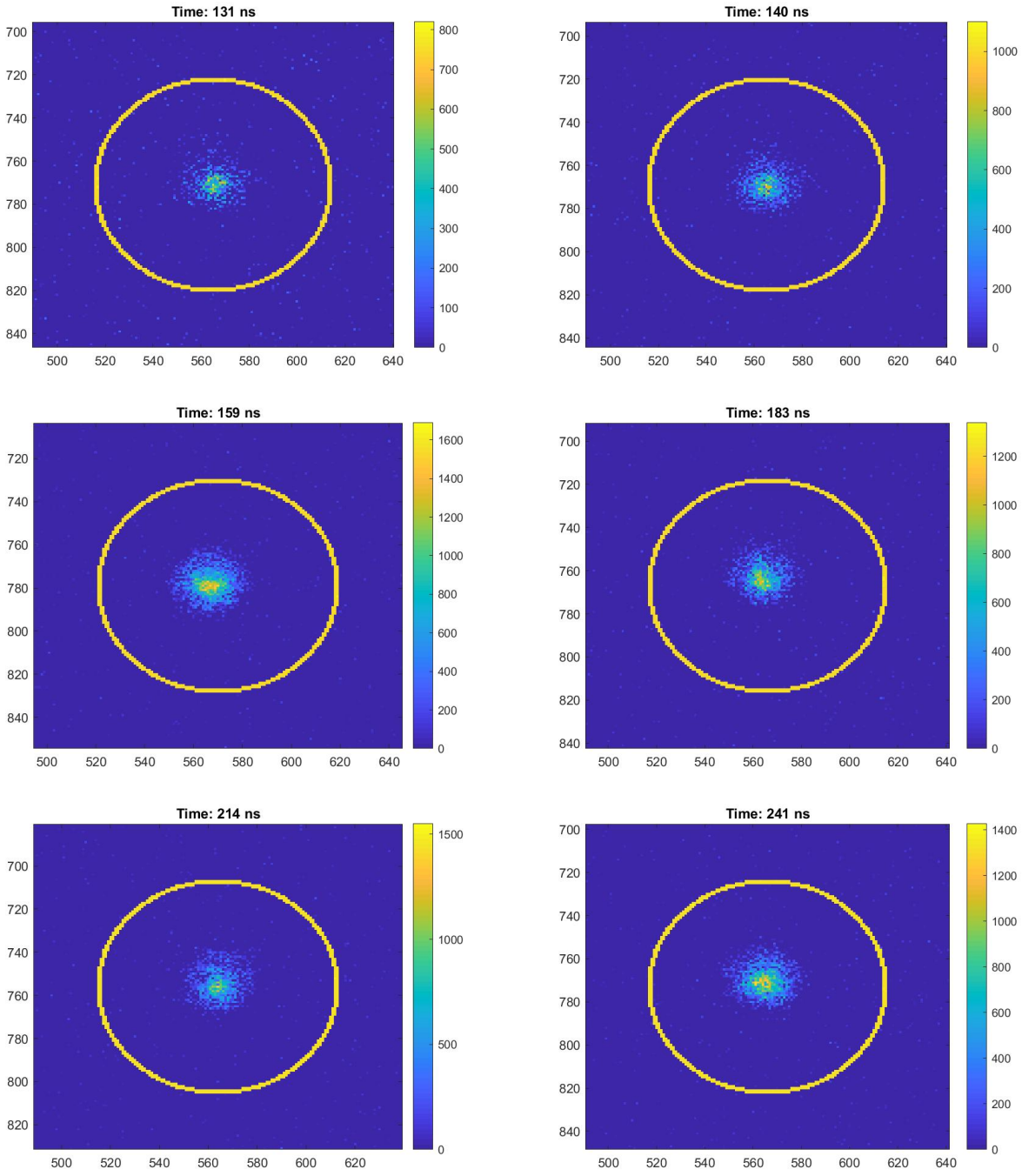

Figure A.3: ICCD Images, Pressure: 136 atm, Time: 131 ns - 241 ns

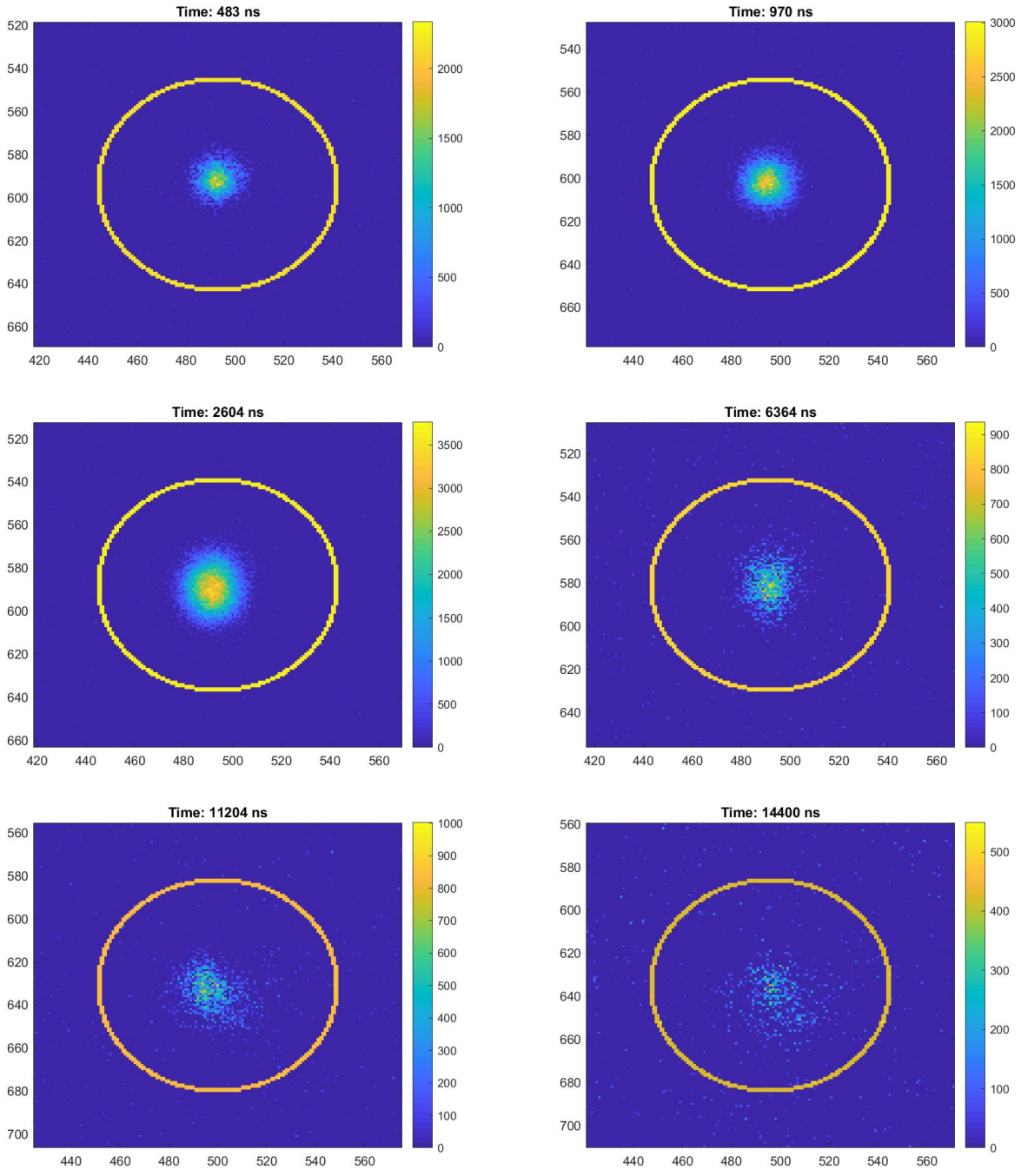

Figure A.4: ICCD Images, Pressure: 136 atm, Time: 483 ns - 14400 ns